

Copyright
by
Behzad Eftekhari
2016

The Dissertation Committee for Behzad Eftekhari
certifies that this is the approved version of the following dissertation:

**A Lattice Model For Gas Production From
Hydrofractured Shale**

Committee:

Tadeusz W. Patzek, Supervisor

Michael P. Marder, Co-Supervisor

Jon E. Olson

Kamy Sepehrnoori

David N. Espinoza

**A Lattice Model For Gas Production From
Hydrofractured Shale**

by

Behzad Eftekhari, B.S.M.E.; M.S.E.

DISSERTATION

Presented to the Faculty of the Graduate School of
The University of Texas at Austin
in Partial Fulfillment
of the Requirements
for the Degree of

DOCTOR OF PHILOSOPHY

THE UNIVERSITY OF TEXAS AT AUSTIN

December 2016

To my parents,
Hashem and Zahra,
and my brother,
Mehrdad

Acknowledgments

Over the past 5 years, I have had the pleasure of working with Dr Tad Patzek and Dr Michael Marder as my advisers and I would like to start this note by expressing my appreciation for their insightful guidance. I feel privileged to have had the opportunity to learn from them. I would like to thank Dr Patzek for his continued support throughout my study. Tad's curiosity, practicality and excellence was the source of much inspiration to me. Of Michael, I would like to say that his wisdom and kindness have been vital to my academic growth; I am forever grateful.

The members of my dissertation committee were all cordial and helpful to me: to Dr Kamy Sepehrnoori, for advising me on my defense and numerous other matters, and to Dr Jon Olson and Dr David Espinoza, for taking the time to discuss technical details with me and making suggestions to extend the work, thank you. I should also thank a non-committee member professor here: Dr Larry Lake was kind enough to meet with me after my defense and share his comments and suggestions with me, for which I am deeply grateful.

Of the good UT PGE staff, I would like to particularly thank Sandy Taylor, Frankie Hart, and Allison Brooks for helping with registration; John Cassibry for all the computer supports, Mary Pettengill for my pleasant volunteer experience at the library, and John Winn for setting up the teleconference

camera for my defense.

My life in Austin has been blessed with friends who have always been supportive and inspiring. Here I shall attempt to thank at least some of them: I would like to thank Aboulghasem Kazemi Nia Korrani and Mohsen Rezaveisi, for having me when I first arrived in Austin and helping me settle. A sincere thank you goes to Saeid Enayatpour, for his tremendous generosity in sharing his experience on \LaTeX and coursework with me. Thank you to my amazing office mates: Yun Wu, Zhong Pan, Bo Ren, Nuntha Naudomsup, Soros Chitsiripanich, Arin Raina, Ryan Leung and the best nearest neighbor I could have hoped for, Brian Lee. Brian's love for art and rational debate made my time at the office infinitely more pleasant. To my physicist friends: Frank Male, Chih-Hung Chen, Matt Guthrie and Wei-Jin Zheng, thank you for the interesting talks and good food. For all the mathematical discussions we had, from which I learned extensively and derived great joy, I thank Amir Khalighi. Thank you to Siavash Zangeneh Kamali, Hossein Ganjizadeh and Morteza Elahi Naraghi, for your support and all the happy memories. Soheil Ghanbarzadeh, Amir Frooqnia, Amir Kianinejad, Ali Goudarzi, Mohammad Lotfollahi and Shaina Kelly, thank you for the stimulating conversations. I finish this note with a sincere thank you to Christen Cardwell, who set up the food at my final defense, helped me prepare my talk and was always incredibly kind and supportive.

The Shell-UT Unconventional Research program is gratefully acknowledged for funding this research project.

A Lattice Model For Gas Production From Hydrofractured Shale

Behzad Eftekhari, Ph.D.

The University of Texas at Austin, 2016

Supervisor: Tadeusz W. Patzek

Co-Supervisor: Michael P. Marder

Natural gas production from US shale and tight oil plays has increased over the past 10 years, currently constitutes more than half of the total US dry natural gas production, and is projected to provide the US with a major energy source in the next several decades. The increase in shale gas production is driven by advances in hydraulic fracturing.

Recent studies have shown that gas production from hydraulically fractured shales has to come from a network of connected hydraulic and natural fractures, and that if one takes the shale permeability to be 10 nD, then the characteristic spacing of the fracture network will be about 1.5 – 3 m. The precise nature of the characteristic spacing, as well as other production and formation properties of the fracture network, are questions which motivated the present dissertation.

This dissertation studies (1) the topology of the fracture network, (2)

the mechanics of how the fracture network evolves in time during injection and (3) how fracture network geometry affects production.

We use percolation theory to study fracture network topology. Fracture are placed on the bonds of a two-dimensional square lattice and follow a power law length distribution. We analytically obtain the scaling of connectivity for power law fracture networks, and numerically compute the percolation threshold as a function of the exponent.

We develop a hydrofracture model which makes it possible to simulate initiation and propagation of hydraulic fractures, as well as the interaction between hydraulic and natural fractures. The model uses the Reynolds lubrication approximation to describe fluid flow through the fractures and relies on analytical estimates to predict the stress response.

We develop a diffusion model to compute gas production from hydraulically fractured shales. The model uses a random walk algorithm and takes the fracture network as the absorbing boundary to the gas transport equation. We show that scaling the cumulative production versus time data from the diffusion model with respect to characteristic scales of production maps the production versus time plots onto a single scaling curve. Using the model, we identify, or define, characteristic spacing for fracture networks.

Table of Contents

Acknowledgments	v
Abstract	vii
List of Figures	xii
Chapter 1. Introduction	1
1.1 Introduction and Significance	1
1.2 Hydraulic Fracture	6
1.2.1 Horizontal Drilling	7
1.2.2 Slickwater Fracturing	8
1.2.3 Multiple Fracture Stages	10
1.2.4 Time Line of Hydraulic Fracturing	11
1.2.5 Motivation	15
1.2.6 Outline	16
Chapter 2. Topology of Hydraulically Induced Fracture Networks	19
2.1 Introduction	19
2.2 Natural–Hydraulic Fracture Interaction	21
2.3 Characterization of the Natural Fracture System in Shales	23
2.4 Percolation Models of Fracture Networks	25
2.5 The Model	28
2.6 Connectivity Scaling	32
2.6.1 Total Number of Fractures in a Lattice of Size L	34
2.6.2 Number of Fractures Longer than the System Size	35
2.6.3 Probability of a Fracture Longer than the System Size	37
2.7 Numerical Computation of the Percolation Threshold	39

2.7.1	The Algorithm to Determine the Apparent Threshold for a Lattice of Size L	39
2.7.2	Extrapolating the Apparent Threshold to Infinite Size	42
2.8	Conclusions	60
Chapter 3. Numerical Modeling of Hydraulic Fractures		62
3.1	Introduction	62
3.2	Outline	63
3.3	Background & Literature Review	64
3.3.1	Fluid Flow through the Hydraulic Fracture	65
3.3.2	Stress Equilibrium	67
3.3.3	Fracture Propagation	68
3.3.3.1	Maximum Circumferential Stress	68
3.3.3.2	Maximum Energy Release Rate	69
3.3.4	Analytical Models	70
3.3.4.1	Penny-Shaped Fracture	71
3.3.4.2	The KGD Model	73
3.3.4.3	The PKN Model	74
3.3.5	Numerical Models	78
3.4	The Model	80
3.4.1	Setup	80
3.4.2	The Lubrication Approximation	85
3.4.3	Fracture Mechanics	88
3.4.3.1	Pressure	88
3.4.3.2	Hydrofracture Initiation	91
3.4.3.3	Hydrofracture Propagation	96
3.4.3.4	Formation of Loops	99
3.5	Validation	100
3.6	Qualitative Observations	105
3.7	Conclusions	111

Chapter 4. Production from Complex Fracture Networks	113
4.1 Outline	114
4.2 Background and Literature Review	115
4.2.1 Derivation of the Transport Problem	119
4.3 The Model	128
4.4 Validation & Results	140
4.5 Conclusions	146
Chapter 5. Conclusions and Future Work	149
5.1 Motivation	150
5.2 The Models	152
5.2.1 Chapter 2: The Percolation Model	153
5.2.2 Chapter 3: The Hydrofracture Model	154
5.2.3 Chapter 4: The Diffusion Model	156
5.3 Future Work	157
5.3.1 Early-Time Production	157
5.3.2 Characteristic Distance as a Function of Fracture Net- work Geometry	159
5.3.3 Scaling of Original Gas in Place with Reservoir Size . .	160
5.3.4 The Stress Shadow Effect	162
5.3.5 Thermodynamic Properties of Natural Gas	162
5.3.6 Finite Fracture Conductivity	163
5.3.7 Extension to Three Dimensions	164
Bibliography	165

List of Figures

1.1	Map of shale plays in the world	3
1.2	Map of the US shale plays in the lower 48 states	4
1.3	Share of shale gas (including natural gas from tight oil plays) in the total US dry natural gas production	5
1.4	US natural gas production by source	6
1.5	Schematic of a typical horizontal well in the Barnett Shale	8
1.6	Volume composition of slickwater	9
1.7	US shale gas and tight oil production	13
1.8	Estimate of annual US shale gas production by play.	14
2.1	Reported values of the fracture length exponent in the literature	31
2.2	Asymptotes of power law length distribution	32
2.3	Connectivity regimes in power law fracture networks	36
2.4	Probability of a fracture at least as long the system size	38
2.5	Cumulative density function of the apparent threshold	43
2.6	Numerical computation of the percolation threshold	51
2.7	Percolation threshold as a function of the fracture length exponent	59
3.1	Fluid setup in the Reynolds lubrication approximation	65
3.2	The penny-shaped (radial) geometry	71
3.3	The KGD geometry	73
3.4	The PKN geometry	75
3.5	Initial configuration of an example hydrofracture simulation	81
3.6	Map view of far-field principal stresses	90
3.7	Initial configuration of seed cracks	92
3.8	Loops in the hydrofracture network	100
3.9	Geometry of the test case used to validate the hydrofracture model	101
3.10	Base pressure history, simulation and theory	102

3.11	Pressure along crack length, simulation and theory	103
3.12	Time evolution of crack volume, simulation and theory	105
3.13	Time evolution of the hydrofracture network	108
4.1	Geometrical setup of the Patzek et al. (2013) model	118
4.2	Dimensionless production rate versus dimensionless time, theory and field data	125
4.3	Dimensionless cumulative production versus square root dimensionless time, theory and field data	127
4.4	Geometrical setup of the diffusion model	132
4.5	A 200×200 example lattice system to demonstrate the procedure to compute M and τ	136
4.6	The procedure to compute the characteristic time to interference τ and the original gas in place M	137
4.7	Least squares fit of theoretical production rate to the distribution of arrival time	138
4.8	Reproduction of the universal scaling curve with the diffusion model	142
4.9	Characteristic spacing of fracture networks	145
4.10	Standard error of the diffusion model	146
5.1	The procedure to compute the characteristic time to interference τ and the original gas in place M , re-visited	158
5.2	Characteristic spacing of fracture networks, re-visited	160
5.3	Scaling of original gas in place	161

Chapter 1

Introduction

1.1 Introduction and Significance

The recent success in producing oil and gas from US mudrocks, commonly known as “shales”, and other low permeability reservoirs is primarily due to advances in hydraulic fracturing. Hydraulic fracturing is a well stimulation technique that enhances hydrocarbon production by creating fractures in the formation. It involves pumping a fracturing fluid into the well at pressures large enough to overcome the mechanical resistance of the reservoir rock and propagate fluid-driven fractures into the pay zone. The fractures increase reservoir exposure and provide hydraulically conductive pathways for the transport of formation hydrocarbons to the well, thereby increasing the effective permeability of the formation and the production rate.

A propping agent (“proppant”) is commonly used to keep the created hydraulic fractures open during the production phase, since they would otherwise shut down under formation stress. Using a high viscosity fracturing fluid improves proppant transport to the hydraulic fractures, and reduces the loss of fracturing fluid to the formation (“leak-off”).

Shales, coal beds (also known as coal seams) and tight sandstones are

collectively referred to as “unconventional” reservoirs in the oil and gas literature. The title “unconventional” refers to how prior to the 1970s, economic production from unconventional reservoirs was generally believed to be impossible: the extremely low permeability of unconventional reservoirs, typically in the nano-Darcy range, prevents practically any hydrocarbon flow through the matrix. In the 1970s, concerns about imminent depletion of domestic natural gas supplies prompted the US Department of Energy to form, in cooperation with private industry operators and the Gas Research Institute, a research venture aimed at assessing the feasibility of production from unconventional natural gas reservoirs and developing/advancing the technologies needed to make production of unconventional natural gas commercially viable (DOE NETL, 2011). Production from deep, extremely low permeability shale plays happened for the first time in the early 1990s, when Mitchell Energy managed to profitably produce gas from the Barnett Shale. Production from unconventional reservoirs started to receive attention only after hydraulic fracturing made profitable production of tight formations possible.

Before we present estimates of technically recoverable shale oil and gas, we first note that at present, because of poor economics, actual hydrocarbon recovery from shales may be 20 – 50% of the technically recoverable reserves, and it is therefore of utmost importance to improve the current efficiency of hydrocarbon drainage.

Shales are estimated to contain 10% and 32% of the world’s technically recoverable crude oil and wet natural gas respectively (EIA 2013). Shale/tight

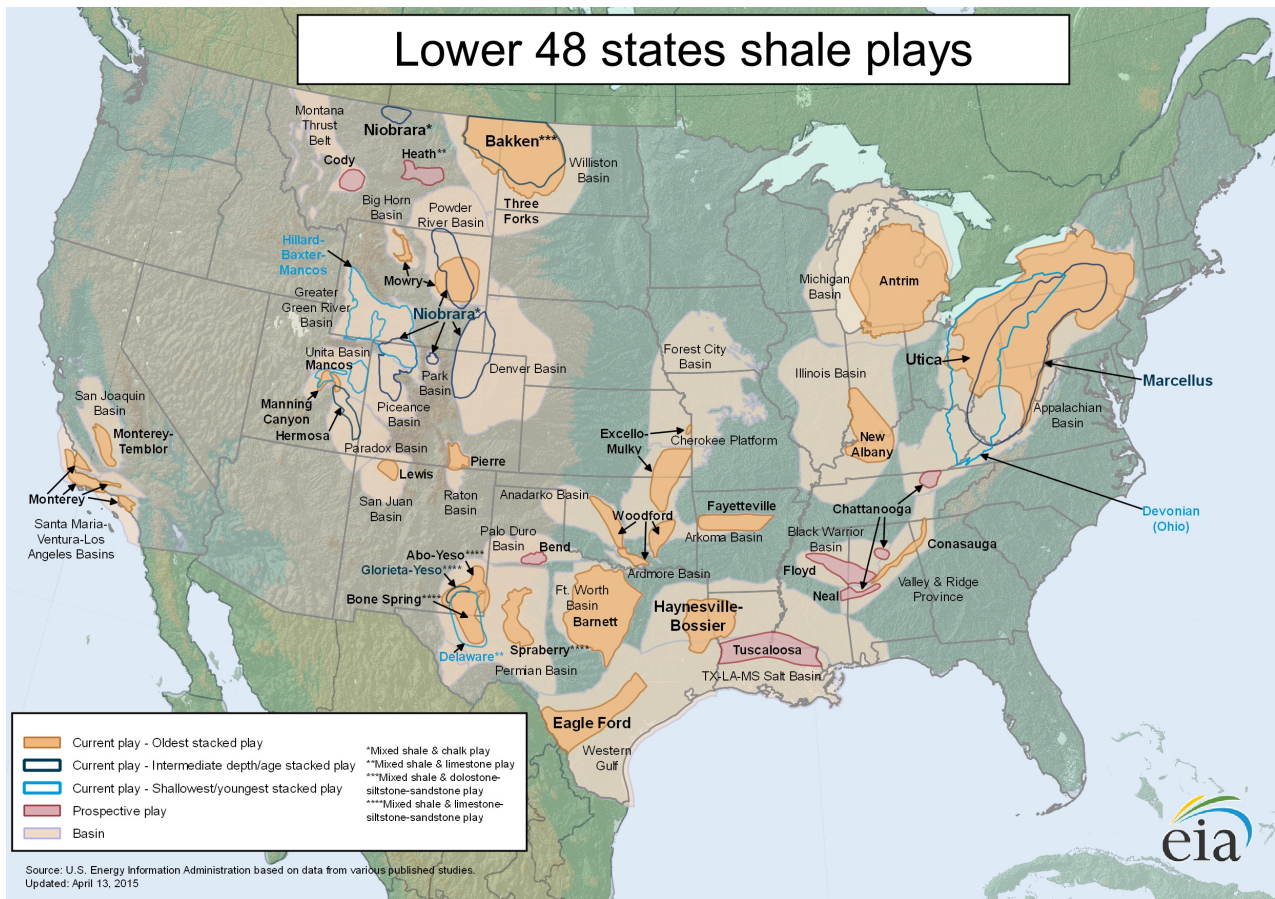


Figure 1.2: Map of the US shale plays in the lower 48 states (EIA, 2015).

Natural gas production from shale and tight oil plays constituted 5% of the total US dry natural gas production in 2004; 10% in 2007; 48% in 2014 and 56% in 2015, Figure 1.3.

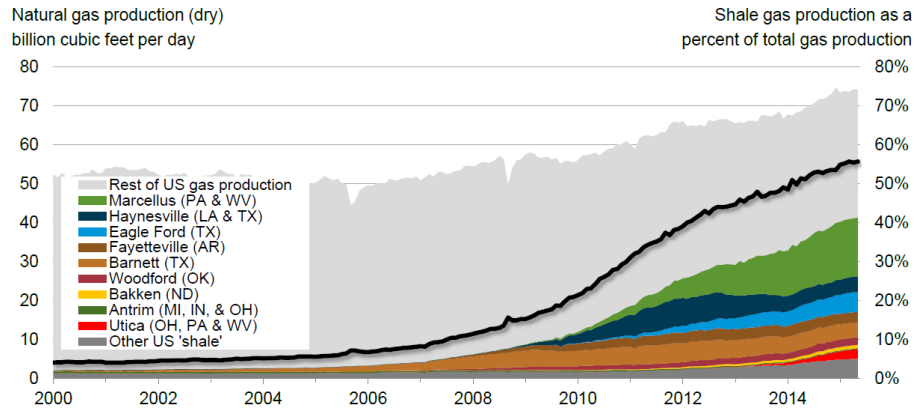


Figure 1.3: Share of shale gas (including natural gas from tight oil plays) in the total US dry natural gas production (EIA, 2015).

The total US dry natural gas production has grown by 35% from 2005 to 2013 and is projected to grow from about 27 Tcf in 2015 to about 42 Tcf in 2040 (EIA Annual Energy Outlook, 2016). Production from shale gas and tight oil plays is the primary contributor to the growth and is projected to grow from about 14 Tcf in 2015 to 29 Tcf in 2040; tight gas production is the second major contributor (EIA Annual Energy Outlook, 2016). Production from all other sources of natural gas (coalbed methane, Alaska and Lower 48 states offshore) is projected to remain relatively steady or decline, Figure 1.4.

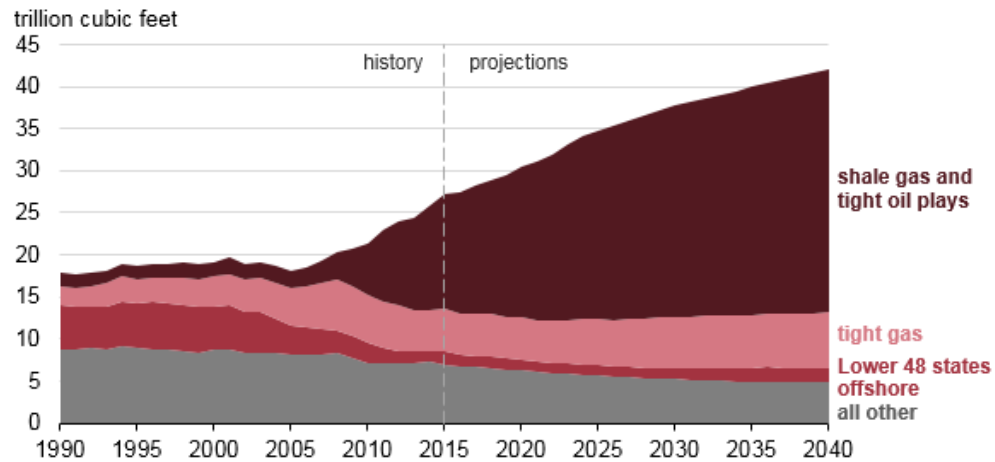


Figure 1.4: US natural gas production by source (EIA, 2016).

The increase in shale gas production is driven by advances in hydraulic fracturing technology. The next section introduces these advances.

1.2 Hydraulic Fracture

The success of present day hydraulic fracturing in shale gas production is primarily due to the following three technologies: horizontal drilling; multiple stimulation intervals, otherwise known as “fracture stages”, completed sequentially along the horizontal section of the well, and injection of large volumes of low friction, water-based fracturing fluids (“slickwater”) (DOE NETL, 2011). Sections 1.2.1 through 1.2.3 introduce these technologies.

1.2.1 Horizontal Drilling

Horizontal drilling is (EIA, 1993) “the process of drilling and completing, for production, a well that begins as a vertical or inclined linear bore which extends from the surface to a subsurface location just above the target oil or gas reservoir called the ‘kickoff point,’ then bears off on an arc to intersect the reservoir at the ‘entry point,’ and, thereafter, continues at a near-horizontal attitude tangent to the arc, to substantially or entirely remain within the reservoir until the desired bottom hole location is reached”. The characteristic advantage of horizontal wells over vertical wells is the significantly improved reservoir exposure: hydrocarbon bearing reservoirs are sedimentary rocks and therefore extend in the horizontal direction significantly more than they do vertically. Although the first horizontal well in the US was completed as early as 1929, application of horizontal drilling to hydrocarbon production started to expand in the early 1980s, by which time the drilling/completion technology had progressed enough to make the technique commercially viable. Figure 1.5 shows a schematic of a typical horizontal well in the Barnett Shale.

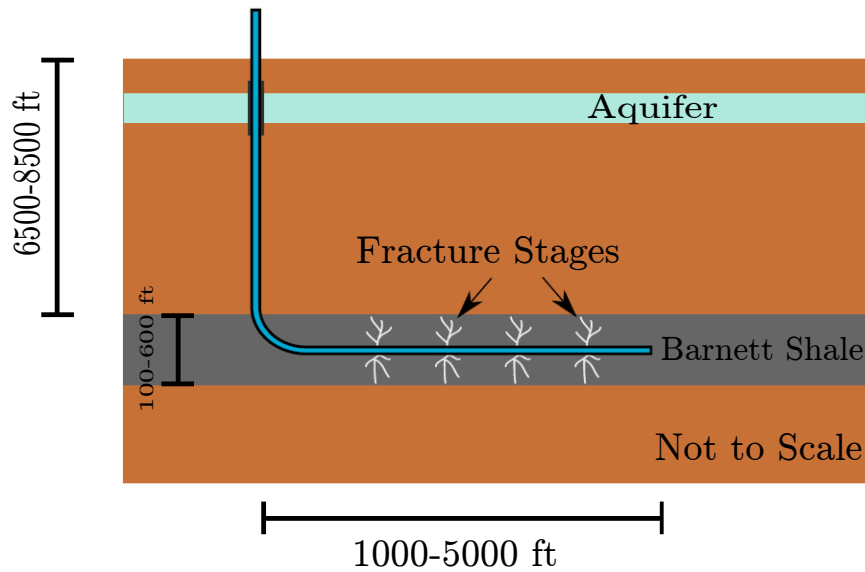


Figure 1.5: Schematic of a typical horizontal well in the Barnett Shale (sketch: modified from Chen, 2014; numbers: DOE NETL, 2009). Horizontal wells in shales can have as many as 25 fracture stages (DOE NETL, 2011); 10-20 stages are typical.

1.2.2 Slickwater Fracturing

In hydraulic fracturing literature, “slickwater” refers to a water-based solution of friction reducing agents and other additives (DOE NETL, 2009). Slickwater is, at present, the most commonly used fracturing fluid. While the type and concentration of the additive depends on the particular treatment, typically 98-99.5% of slickwater consists of water and a propping agent (“proppant”; usually silica sand). Figure 1.6 shows the volume composition of the slickwater used in a horizontal well in the Fayetteville Shale.

Slickwater fracturing of a typical horizontal shale gas well requires 2-4

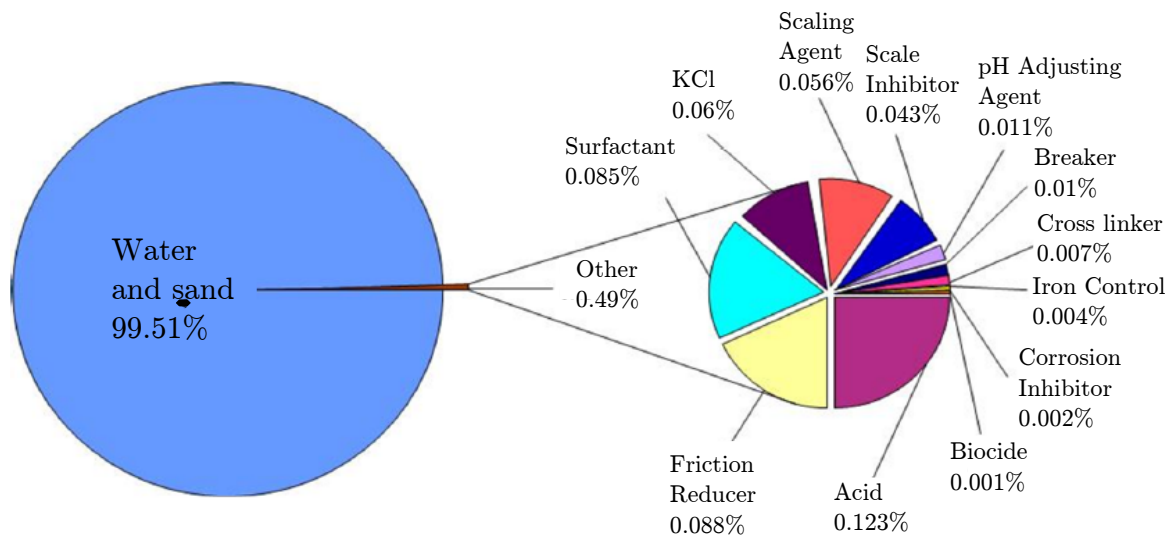


Figure 1.6: Volume composition of the slickwater used in a 9-stage hydraulic fracture treatment in the Fayetteville Shale (modified from DOE NETL, 2009). Slickwater is predominantly water and proppant.

million gallons of water (DOE NETL, 2009). The water is usually supplied from surface waters; underground, produced and municipal waters may also be used as sources. Field experience indicates that once the hydraulic fracture treatment is complete and the pumps are stopped, typically as little as 20–25% of the injected water will be produced back (DOE NETL, 2013). The exact nature of the mechanisms which retain the injected water in the subsurface, as well as how a larger fraction of the injected water can be produced, are as of yet unknown and of significant economic importance to the operators.

1.2.3 Multiple Fracture Stages

A “stage” refers to any sub-interval of the lateral section of a given horizontal well, stimulated through hydraulic fracturing generally while isolated from the rest of the well. Multi-stage fracturing today is done in several ways. Schlumberger’s “plug-and-perf” procedure (Schlumberger, 2016), for instance, consists of the following sequence: first, a perforation gun is moved through the well to the location of the stage and fired to perforate casing in several clusters and form local “seed” cracks in the reservoir rock. The perforation gun is then moved up hole to the location of the next planned stage and a plug is used to hydraulically isolate the stage just created from the rest of the well. The plug stops flow up hole, but allows flow down hole into the stage. Finally, fracturing fluid is injected into the seed cracks at pressures large enough to overcome the mechanical resistance of the formation and propagate fluid-driven fractures into the formation. The process is then repeated to create more stages.

In present day hydraulic fracture treatments, the first stage is placed close to the end of the horizontal well (“toe”) and each additional stage is completed up-hole of the previous stage, such that the last stage is close to the beginning of the lateral section of the horizontal well (“heel”). Stages are stimulated sequentially and from the first to the last: because the stages are arranged in series, simultaneous stimulation of all stages would require fracturing fluid pressures usually well above practical operational limits (DOE NETL, 2009).

About 10-20 stages are typical for horizontal shale gas wells. Reservoir characterization information from well logs (for instance, presence of faults along a specific interval of the lateral, indicated by an image log), informs the operator's decision on the location of the most productive intervals and, consequently, the location of the stages.

1.2.4 Time Line of Hydraulic Fracturing

The first application of hydraulic fracturing dates back to 1947, when the Pan American Petroleum Corporation used the technique to stimulate the Hugoton field in Kansas (Adachi et al., 2007). In a 1949 paper, the Stanolind Oil and Gas Company introduced the technique to the oil and gas literature under the commercial name "Hydrafrac", reporting a significant, sustained increase in the production rate of 11 out of a total of 23 wells stimulated using the technique (J. B. Clark, 1949). The fracturing fluid in Hydrafrac was an oil-based gel, consisting of crude oil/gasoline; a bodying agent, which was, because of availability and price at the time, war surplus Napalm; a "gel breaker" solution to reduce the viscosity of the gel, and sand as a propping agent (J. B. Clark, 1949). At the time, unconventional reservoirs were not yet considered production targets and the technique was applied to conventional reservoirs only.

Application of hydraulic fracturing to US oil and gas wells expanded rapidly after 1949, such that by the end of 1955, more than 100,000 treatments were completed in the US (Hubbert and Willis, 1972). By late 1970s, shale

gas production was limited to relatively shallow shale plays such as the Appalachian Ohio shale and Antrim shale in Michigan. Production from deeper, extremely low permeability shales such as the Barnett or the Marcellus Shale was generally believed to be uneconomical at the time.

Gas production from the Barnett Shale was pioneered by Mitchell Energy. In the 1980s, Mitchell Energy combined horizontal drilling with large volume hydraulic fracture stimulation and persistently improved their hydraulic fracturing field procedure through learning from extensive trial and error, eventually completing the first profitable Barnett Shale gas well in the early 1990s. Success of Mitchell Energy in the Barnett Shale attracted significant attention to the Barnett Shale as well as other major US shale plays, including Haynesville, Woodford, Fayetteville, Eagle Ford and Marcellus Shale, and led to the “shale boom”, or rapid increase, in the US production of shale/tight gas and shale/tight oil, Figure 1.7.

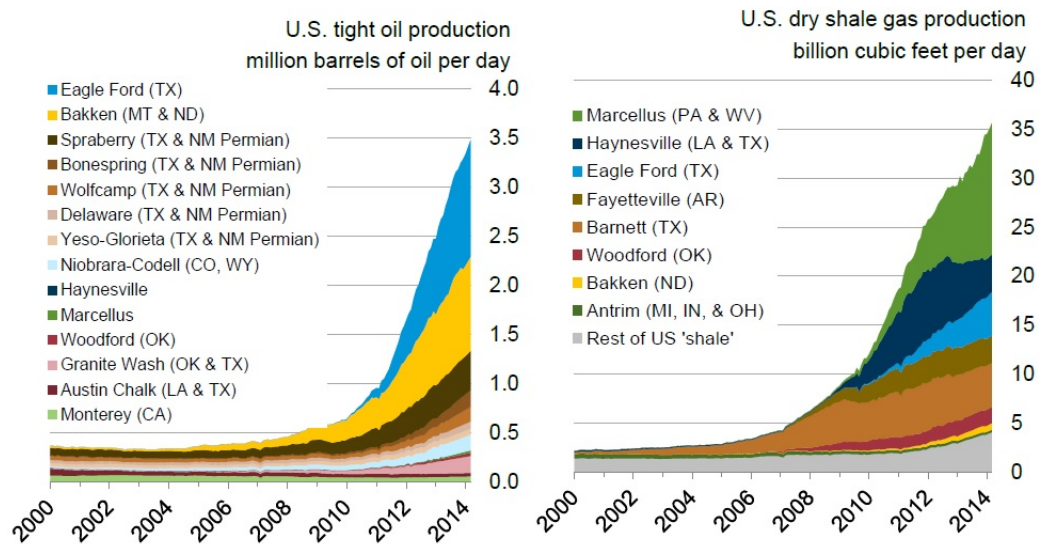


Figure 1.7: US shale gas and tight oil production (EIA 2014).

An estimate of US shale gas production for the current development cycle is presented in Figure 1.8. The predictions were shown to be in good agreement with historical well-by-well field data for 73,000 wells, with 10 – 20% well attrition (T. Patzek, private communication, November 6, 2016). The estimate indicates that the total rate of gas production from US shales has reached a peak in 2016, and therefore improving the efficiency of hydrocarbon recovery from shales is of utmost importance.

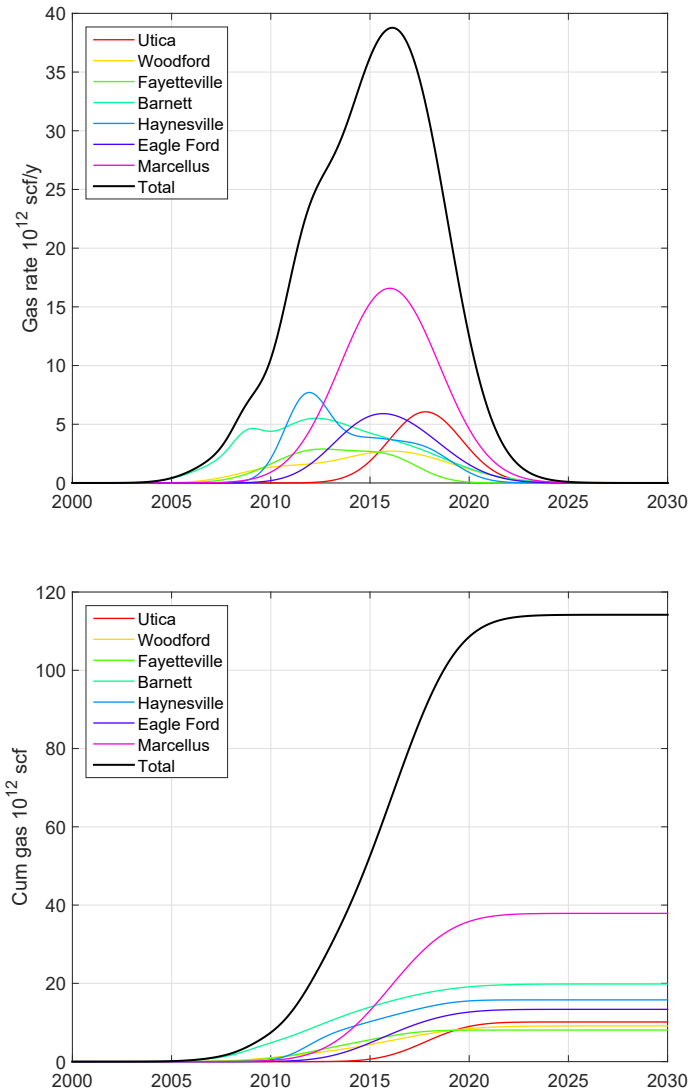


Figure 1.8: Estimate of annual US shale gas production (top) and cumulative production (bottom) by play (T. Patzek, private communication, November 6, 2016). At present (2016), the total production rate has already peaked (black curve, top plot) and the cumulative production will stagnate at about 2022 (black curve, bottom plot). The plots demonstrate the importance of improving the efficiency of hydrocarbon production from shales.

1.2.5 Motivation

There appears to be a gap in our understanding of the nature of hydraulically induced fracture networks. Discharge from the shale matrix alone can not possibly account for field production data, and Patzek et al. (2014) have shown that if hydrofractures are taken to be parallel planes, perpendicular to the wellbore and of generally accepted dimensions, and if gas is taken to flow from the shale to the hydrofractures linearly and in a transient fashion, then to account for Barnett Shale cumulative production history data requires either

1. For a hydrofracture spacing of 75–100 m, effective permeability values of the Barnett Shale/hydrofracture system which are 10 – 100 times larger than lab-measured values of shale matrix permeability, or
2. A spacing of 1.5 – 3 m between the hydrofractures, for a 10 nD shale matrix.

Patzek et al.’s model matches the production history of more than 8000 wells in the Barnett Shale with reasonable accuracy. If one adopts the view expressed in result 1, Patzek et al. suggest that the enhanced permeability is due to a ramified, well-connected system of hydrofractures and natural/induced fractures created by the hydraulic fracture treatment (“fracture network” from here on, for convenience). If one instead adopts the view that shale permeability is about 10 nD (result 2 above), Patzek et al. suggest that the 1.5–3 m

spacing between hydrofracture stages should be interpreted not as the actual distance between stages in the field but as a characteristic spacing of the fracture network, resulting from the topology and transport properties of the network, and that the viability of profitable shale gas wells flows from that portion of the reservoir which has a spacing of 1.5 – 3 m or tighter. We adopt this view in the present dissertation.

The relevance of topology and transport becomes more pronounced when we consider that hydraulic fracturing in the Barnett Shale seems to have produced only 10 – 15% of the (geometric) original gas in place (Patzek et al., 2014): there is ideally potential for as much as a factor of about 2 increase of shale gas production using hydraulic fracturing. Providing insights into how this potential can be exploited is the primary motivation for the present PhD research.

The focus of this PhD is on topology and transport properties of complex hydraulic fracture networks, and the end goal of this research is devising practical strategies to optimize fracture treatments, i.e. creating better-connected, more productive fracture networks that can drain the reservoir more quickly.

1.2.6 Outline

The present dissertation is structured in the following way: first, the nature and topology of hydraulically induced fracture networks is discussed in Chapter 2. A tool used in the present research to model the topology is

percolation theory. Chapter 2 concludes by suggesting that hydraulic fractures primarily propagate along a connected network of relative mechanical weaknesses which either exist as natural fractures or are incipient at the beginning of the treatment and may break in mode I later as the injection continues.

Chapter 3 presents a pseudo-3D numerical model of how the fracture network develops over time during the treatment. The model restricts the fracturing fluid to flow only inside the system of natural fractures/incipient cracks suggested by Chapter 2, and simulates hydraulic fracture propagation, diversion and arrest. The model couples fluid flow through the hydraulic fractures with the elastic response of the rock which hosts the fractures. Fluid flow is modeled directly using the Reynold's lubrication approximation; the elastic response is approximated using analytical expressions which describe a single fracture of a relatively simple geometry, namely PKN or penny-shaped. The model was created to simulate a great number of fractures in a computationally efficient, robust fashion.

The outcome of Chapter 2 and Chapter 3 is a complex network of connected fractures. This network drains gas from the rock and provides hydraulically conductive pathways to the flow of gas from the formation to the wellbore. Gas transport therefore occurs first through the shale to the hydrofracture network, and then through the fractures to the wellbore. Chapter 4 introduces a diffusion model based on random walk that treats gas transport through the shale and the fracture network uniformly and predicts the decline associated with gas production from any complex hydrofracture network. The

hydrofracture network that will be input to the random walk model is the one predicted by Chapter 2 and Chapter 3.

Review of the relevant literature is presented not as a separate chapter but rather as a section at the beginning of each chapter. Finally, Chapter 5 reviews the main conclusions of this dissertation and proposes future courses of research in extension of the present work.

Chapter 2

Topology of Hydraulically Induced Fracture Networks

2.1 Introduction

So far in this dissertation, it has been established that gas is produced from hydrofractured shales through a ramified network of connected fractures: the network drains the gas from the rock and provides hydraulically conductive pathways to the flow of gas from the formation to the wellbore (see 1.2.5).

This chapter studies the topology of the hydraulically induced fracture network. The relevance and significance of fracture network topology can be established by considering how the topology qualitatively controls the ultimate production and the production rate. A more ramified network offers increased reservoir exposure and therefore increased access to the gas in place. In addition, increased ramification reduces the average distance over which the gas diffuses through shale to reach the network. Therefore, topology of the network controls how quickly this network can drain its neighboring reservoir rock.

Once gas has reached the fracture network, the effective hydraulic conductivity of the network controls how quickly the gas flows through the frac-

tures and gets to the well. The effective hydraulic conductivity of the fracture network is controlled by the configuration of the fractures which make up the network, in a manner similar to how effective electrical resistance of networks of resistors is controlled by how the resistors are arranged. Network topology controls the gas travel time both when the gas is diffusing through the shale towards the network and when the gas is flowing inside the fractures towards the well. Consequently, network topology controls the production rate.

This chapter starts by reviewing experimental and theoretical evidence from literature in support of the idea that the topology of hydraulically induced fracture networks is due primarily to the interaction of hydraulic fractures with pre-existing natural fractures/incipient cracks (section §2.2). Characterization of the natural fracture/incipient crack system is discussed next (section §2.3).

We use percolation theory to analyze the connectivity of fracture networks characterized with a power law fracture length distribution. A review of relevant percolation literature is presented in section §2.4. The assumptions, definitions and properties of the model used in this dissertation can be found in section §2.5. The percolation problem solved in this chapter is a variation of the ordinary bond percolation problem on a two-dimensional square lattice, in which the length of the elements (fractures) follows a power law distribution and each element can span multiple lattice bonds at once. Unlike ordinary bond percolation, in which all bonds are identical in size, the fractures which make up the fracture network in the present research exist across multiple scales.

Scaling of fracture network connectivity has been studied theoretically in the present research; see section §2.6. Percolation threshold has been computed numerically; see section §2.7.

2.2 Natural–Hydraulic Fracture Interaction

The idea that geologic discontinuities can significantly affect the overall geometry of hydraulic fractures is not new. In mine back experiments at the US DOE Nevada Test Site, Warpinski and Teufel (1987) observed that “even in the most homogenous of the ash–fall tuff formations, the hydraulic fractures diverge considerably from the usual picture of a planar feature; multiple stranding, fracture meandering, and large–scale surface roughness are common occurrences.” They also observed that multiple strands originated from natural fractures that were opened and filled by fracturing fluid.

Interaction between hydraulic and shale–hosted natural fractures, as well as the subsequent formation of a “complex” fracture network, has been suggested by microseismic monitoring of hydraulic fracture growth in shale. Fisher et al. (2004) report the formation of a multi–planar fracture network in vertical Barnett Shale wells. The network showed major fracture growth in two *orthogonal* directions: that of present–day maximum horizontal stress (S_{Hmax}), and the predominant trend of natural fractures.

Hydraulic fractures have been observed to interact with natural fractures according to one of the following scenarios: arrest, diversion, and crossing. Blanton (1982) systematically varied the angle of approach of the hy-

draulic fracture to pre-existing fractures in blocks of hydrostone under triaxial stress, and observed that a hydraulic fracture will cross a natural fracture only if the angle of approach is high and the stress normal to the natural fracture is much larger than the stress along the natural fracture. Blanton reports that in most of his experiments hydraulic fractures were either diverted or arrested by the pre-existing fractures. Arrest is defined as the termination of hydraulic fracture against the natural fracture. Diversion or deflection corresponds to when the hydraulic fracture hits the natural fracture and continues to propagate along one or both wings of the natural fracture.

Gale and Holder (2008) conducted bending tests on samples of the Barnett Shale and concluded that samples with calcite-filled natural fractures had approximately half the tensile strength of the fracture-free host rock. If one couples this experimental result with the fracture mechanics result which states that fracture energy scales with the square of yield strength, it follows that for the fracturing fluid to break open a typical calcite-filled natural fracture takes about a quarter of the energy needed to fracture the shale matrix. Such natural fractures therefore can act as “planes” of relative mechanical weakness and are prone to re-activation during hydraulic fracture treatments. The set of relative mechanical weaknesses inside the shale is not, however, limited to natural fractures: the heterogeneity in rock strength can manifest itself also in cracks which are incipient at the beginning of the treatment and may later break in mode I as the injection continues. Characterization of both natural fractures and incipient cracks is therefore essential to the optimum design

of hydraulic fracture treatments. The following section presents a review of relevant results from the literature on characterization of the natural fracture system in shales.

2.3 Characterization of the Natural Fracture System in Shales

Shale gas reservoirs show diversity in characteristics of host rock and natural fractures. The most comprehensive studies of natural fractures in US shales to date are presented in Gale and Holder (2010) and Gale et al. (2014). The studies examined cores and outcrops of several US shales, including Barnett Shale, Marcellus Shale, Eagle Ford Shale, Haynseville Shale, Woodford Shale, New Albany Shale, Niobrara formation, Austin Chalk, Monterey formation, and Smithwick formation. Despite the diversity, the studies report several common features among the investigated shale gas reservoirs, including:

1. There are three common types of opening mode fractures in shales: those at a high angle to bedding, which are mostly subvertical; bedding parallel fractures, and compacted fractures. The most important type is the high angle group. Compacted fractures are expected to have a negligible effect on production from shales.
2. The most common type of natural fracture is planar and filled with calcite. This is also the case in the Antrim shale of the Michigan basin

(Ryder 1996).

3. Quartz-filled natural fractures are mechanically strong and could arrest the propagation of hydraulic fractures. Quartz bridges in East Texas tight sands have been shown to prop natural fractures at a depth of 5000 ft to an aperture of 2 mm, maintaining open fractures in the subsurface.
4. Drilling and thin section preparation procedure are known to fracture shales parallel to bedding planes, but there has been no evidence of naturally occurring, bedding-parallel, open microfracture networks in mudrocks.

Characterization of natural fractures is still an active area of research. Cores, outcrops, image logs and their combinations are the primary sources of data on subsurface fractures. As far as characterization of the natural fracture system, the data are too sparse to be conclusive.

Interpretation of the data, for instance to determine the origin of the natural fracture system, is also often non-unique. In its report of natural fracture patterns and their origin in the Antrim Shale, USGS recognizes continental scale compressional stress fields as the most probable origin of the fracture system, and proposes two plausible candidates for the origin of the stress field (Ryder 1996). Gale's (2008) list of possible origins of the fractures in the Barnett Shale includes regional burial plus hydrocarbon generation; regional, tectonic stress; differential compaction; local effects of major faults and

folds; sag features associated with underlying karst, and stress release during uplift.

Marrett et al. (1999) studied data collected from natural faults and extension fractures and found that cumulative frequency versus fracture aperture showed power law scaling across about 3–5 orders of magnitude. Hooker et al. (2014) also observed universal power law scaling for cumulative frequency versus fracture aperture in sandstones, with the exponent being equal to 0.8. Power law size scaling of natural fractures has been observed in studies of natural fractures and fault patterns in different geologic formations around the world (for a review of several such studies, see Sahimi, 1994). Consistent with the idea that rock fractures form self-similar patterns, several of the studies mentioned by Sahimi (1994) independently obtained similar values for the exponent of the power law. In these studies, the power law described frequency versus fracture length and the exponent was reported to be either 1.9 or 1.6–1.7 in 2D and 2.5 in 3D. These power law exponents are consistent with the mass dimensions of percolating clusters at percolation threshold in 2D and 3D (1.9 and 2.5).

2.4 Percolation Models of Fracture Networks

Since its inception by Broadbent and Hammersley (1957), percolation theory has been used extensively to model a wide range of problems in different fields. These problems include fluid flow and transport in porous media/fractured media, conductivity of semi-conductors, mechanical properties

of polymers, etc. Generally, percolation theory describes how random connectivity of a large number of elements leads to properties for the connected system as a whole.

Historically, bond percolation precedes the other variants of percolation theory. In the classical bond percolation problem on a lattice, lattice bonds are selected with probability p , known as the *percolation parameter* or the *concentration* (Stauffer and Aharony, 1992). Selected bonds are considered open; otherwise, they are closed. Because all bonds are identical, p is the ratio of the number of open bonds to the total number of lattice bonds. Nearest neighbor bonds are considered connected, and a group of connected open bonds is known as a *cluster*. Size of each cluster is the number of bonds in the cluster (Stauffer and Aharony, 1992).

If p is gradually increased from 0, initially small clusters form, then each cluster becomes larger and some clusters may connect and form larger clusters. *Percolation* is said to have happened when for the first time a cluster gets large enough to connect the opposite sides of the lattice. This cluster is known as the *spanning cluster*. The value of p at percolation for an infinitely large system is known as the *percolation threshold* and is typically denoted p_c (“ p critical”). In an infinite system, there is no connected path between the opposite sides of the lattice for $p < p_c$ and there is always a connected path for $p \geq p_c$. In ordinary lattice percolation, percolation threshold depends on the type of lattice and the type of percolation problem (site or bond) (Stauffer and Aharony, 1992).

Application of percolation theory to study the connectivity of fracture systems dates back to 1983 (Robinson, 1983). The technical problem which motivated the percolation studies at the time was to ensure that radioactive waste stored in low permeability rock will not leak from its storage site through fractures.

From the early 1980s to 1994, connectivity and transport properties of various two and three-dimensional fracture systems were determined numerically and a theoretical understanding of the governing parameters was established. A detailed review of the relevant literature may be found in Berkowitz and Balberg (1993) and Sahimi (1994).

Bour and Davy (1997) studied the connectivity of a two-dimensional system of fractures characterized by a power law length distribution and uniformly distributed fracture location and orientation. Citing studies of natural fault networks, they used the following length distribution:

$$n(l) \sim l^{-a}, \quad (2.1)$$

in which $n(l)$ is the number of fractures of a length in $[l, l+dl]$. The exponent a was found to control the structure of the spanning cluster, such that for $a > 3$, the cluster was exclusively made of fractures shorter than the system size (“short” fractures); for $1 < a < 3$, a mix of short fractures and fractures longer than the system size formed the spanning cluster, and for $a < 1$, the cluster was made of the longest fracture in the system. The percolation threshold reported by Bour and Davy (1997) was found to be almost independent of the

exponent and the system size.

Despite differences in definition and setup, our percolation model yields the same connectivity regimes as those first obtained by Bour and Davy (1997). We will discuss the differences of the two models in more detail in the next section.

2.5 The Model

Based on section §2.2 and section §2.3, while it is true that certain cements like quartz require more energy to break than does the shale matrix, such cements are rare compared to calcite, the fracture energy of which is equal to about a quarter of that of shale. All cement-filled natural fractures and incipient cracks in the present model are assumed to have a fracture energy much lower than the shale. For the purpose of the model, natural fractures and incipient cracks are essentially identical: hydraulic fracture propagation along all natural fractures/incipient cracks in the model is assumed to be energetically more favorable than propagation through the shale which surrounds the natural fractures/incipient cracks (we note that energy release rate in general depends upon the loading, and energy release rate minus fracture energy might be greatest along directions other than those of the natural fractures; we refer to these directions as incipient cracks). Consequently, if a hydraulic fracture intersects and opens any natural fracture/incipient crack that belongs to a cluster of connected natural fractures/incipient cracks, any further propagation of the hydraulic fracture will be along the fractures/cracks of the

cluster, and the fracturing fluid will remain restricted to the cluster. In this model, the fracture network ultimately responsible for production is that subset of the natural fracture/incipient crack system which has been opened by the fracturing fluid.

In this work, we model the natural fractures/incipient crack system as a stochastic population of lines on a two-dimensional square lattice. Lattice spacing a and lattice size L characterize the lattice.

In Bour and Davy (1997), fracture orientation is assumed to be uniform in all directions. Fractures in our model are placed on a square lattice and are therefore either horizontal or vertical: one direction may be interpreted as the dominant trend of natural fractures/incipient cracks; the other, a cross-cutting direction.

In Bour and Davy (1997), fractures are uniformly distributed on the plane and are not bound to any lattice. In the present research, fractures are randomly placed on a square lattice. To place a given horizontal fracture on the lattice, we first point with equal probability to a point on the two-dimensional domain bounded by the lattice, then round the y -coordinate of the point to the nearest multiple of the lattice spacing to obtain a randomly chosen point on the lattice grid lines. A random point along the fracture is then placed on the point on the grid line. Vertical fractures are placed on the lattice in a similar fashion.

Lines that cross the lattice boundaries are cropped and only the seg-

ment inside the lattice is kept. Lines that overlap are merged together and counted as one. Two fractures are said to be “connected” if they intersect, and any connected set of natural fractures/incipient cracks will be referred to as a “cluster” from here on.

We take the fracture length distribution to be a cut-off power law, bound between a minimum fracture length l_{min} and a maximum length l_{max} , and characterized by an exponent e . If a fracture is randomly drawn from the fracture population, the probability that the fracture is of length l or less is taken to be

$$F(l) = \frac{l^{-e} - l_{min}^{-e}}{l_{max}^{-e} - l_{min}^{-e}}, \quad (2.2)$$

where $F(l)$ is the cumulative density function of the length distribution.

The length of each fracture is rounded to the nearest multiple of the lattice spacing, so each line in the model will start and end at a lattice node. Each fracture can span multiple lattice bonds. Simulations in this work have shown that rounding the fracture length, cropping the fractures which cross lattice boundaries and merging the ones that overlap changes the length distribution only slightly.

The reported values of the exponent for geological systems are between 0.8 and 2.2 with a mode at $e = 1.2$, Figure 2.1.

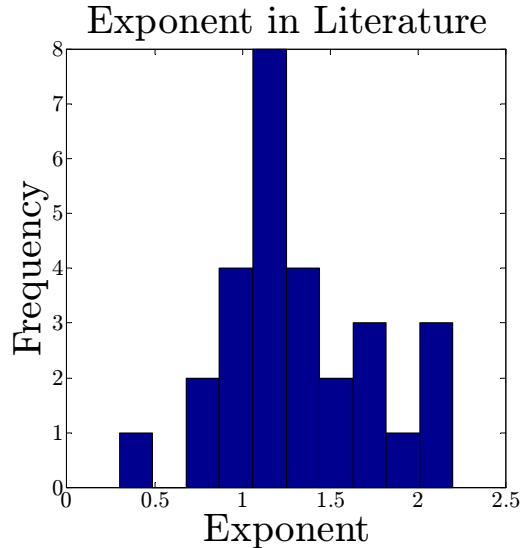


Figure 2.1: Reported values of the exponent from 28 papers, each studying > 200 fractures. (Reproduction of figure 12-b from Bonnet et al., 2001)

The asymptote of the length distribution in the limit of small exponents is the logarithm function:

$$\lim_{e \rightarrow 0} F(l) = \lim_{e \rightarrow 0} \frac{l^{-e} - l_{min}^{-e}}{l_{max}^{-e} - l_{min}^{-e}} = \frac{-\ln(l) + \ln(l_{min})}{-\ln(l_{max}) + \ln(l_{min})}; \quad (2.3)$$

in the limit of large exponents, length of every fracture becomes equal to $l_{min} = a$, i.e., the problem is reduced to the classical bond percolation problem:

$$\lim_{e \rightarrow \infty} F(l) = \lim_{e \rightarrow \infty} \frac{l^{-e} - l_{min}^{-e}}{l_{max}^{-e} - l_{min}^{-e}} = \lim_{e \rightarrow \infty} \frac{(l/l_{min})^{-e} - 1}{(l_{max}/l_{min})^{-e} - 1} \rightarrow 1. \quad (2.4)$$

The asymptotes can be seen in Figure 2.2.

Increasing the exponent from 0 to large values makes the occurrence of long fractures less likely. For small e , fractures longer than the system size (“long” fractures) are probable and the spanning cluster may be made of only

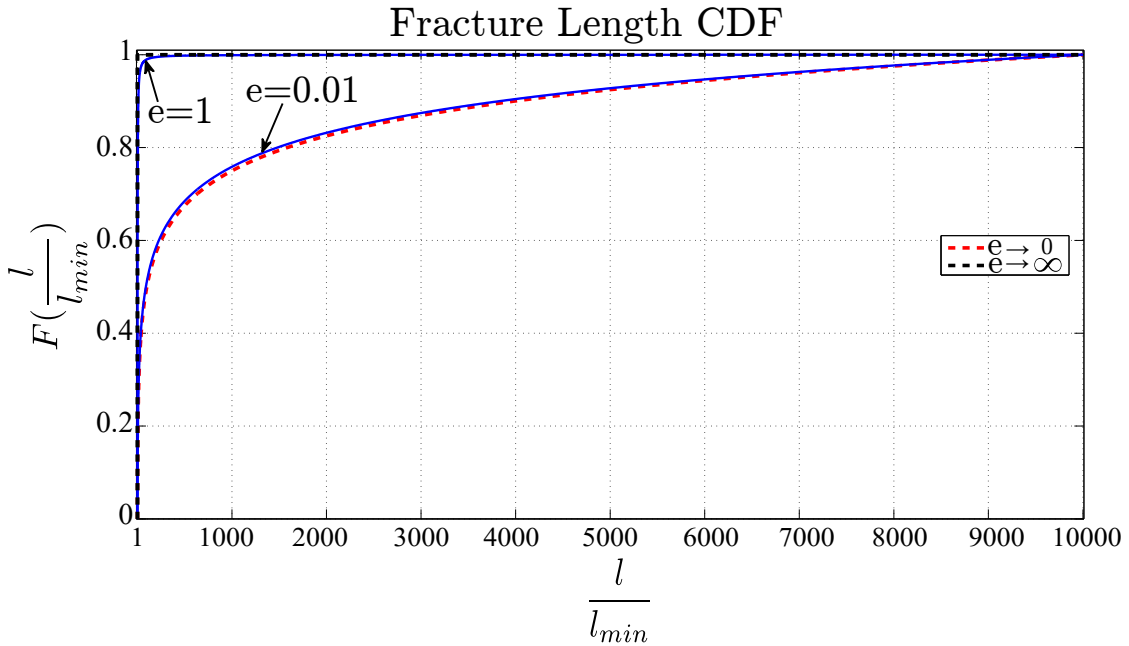


Figure 2.2: The two asymptotes of the power law length distribution are the unit step function at $e \rightarrow \infty$, and the log distribution at $e \rightarrow 0$.

one such fracture, while for large e long fractures are improbable and therefore the spanning cluster is expected to be made of connected short fractures only. We are interested in finding the percolation threshold as a function of the fracture length exponent e .

2.6 Connectivity Scaling

This section presents a theoretical analysis of how lattice size and the exponent e control the connectivity of the model described in section §2.5. In particular, we first derive an expression for the total number of fractures in a lattice of size L , $N(L)$, as a function of e and a network density term (sec-

tion 2.6.1). We then use $N(L)$ to derive a scaling relationship which describes the number of fractures longer than the lattice as a function of lattice size and the exponent e (section 2.6.2). We predict that depending on e , connectivity of the model will have one of two possible characters: for $e > 2$, connectivity emerges from clustering of fractures shorter than the system size into a spanning cluster; for $1 < e < 2$, connectivity is made possible not by clustering of short fractures but rather by a few fractures or even a single fracture of a size comparable to or longer than the system size, which can directly connect the opposite sides of the lattice. In this regime, connectivity no longer has the character of percolation.

The connectivity regimes predicted in this dissertation are derived for a *lattice* model. They turn out, however, to be identical to the connectivity regimes obtained by Bour and Davy (1997) for *off-lattice* fracture systems with random fracture orientation and location. We should note here that the results of this chapter were obtained independently, and we found the main result in the Bour and Davy (1997) paper after the present work was done. In any case, the two models are different in that our model is set up on a lattice, uses a different definition for the percolation parameter, and predicts the percolation threshold to depend upon the exponent e . We will present a detailed comparison of the percolation thresholds from the two models at the end of section 2.7.2.

The probability for the occurrence of fractures longer than the lattice size has been analytically determined in this work. The derivation is presented

in section 2.6.3.

2.6.1 Total Number of Fractures in a Lattice of Size L

The fracture length probability density function, $f(l)$, is given by

$$f(l) = \frac{dF}{dl} = \frac{-el^{-e-1}}{l_{max}^{-e} - l_{min}^{-e}}, \quad (2.5)$$

where F is the fracture length cumulative density function and has been previously defined by equation (2.2).

We take $l_{max} \gg L$, let $l_{max} \rightarrow \infty$ and set $l_{min} = \text{lattice spacing} = a = 1$. All fractures lie completely inside a lattice of size l_{max} . If we randomly point to an $L \times L$ subdomain of the $l_{max} \times l_{max}$ lattice, in the subdomain and *on average*, the total number of fractures is $N(L)$; the total number of occupied bonds is $M(L)$. If the total number of fractures in the $l_{max} \times l_{max}$ lattice is $N(l_{max})$, then

$$\begin{aligned} M(L) &= \frac{L^2}{l_{max}^2} \int_{l_{min}}^{l_{max}} N(l_{max}) f(l) l \, dl \\ &= \int_{l_{min}}^{l_{max}} N(L) f(l) l \, dl. \end{aligned} \quad (2.6)$$

$$\begin{aligned} \int_{l_{min}}^{l_{max}} N(L) f(l) l \, dl &= N(L) \int_{l_{min}}^{l_{max}} \frac{-el^{-e}}{l_{max}^{-e} - l_{min}^{-e}} \, dl \\ &= N(L) \frac{1}{l_{max}^{-e} - l_{min}^{-e}} \frac{-e}{1-e} \left(l_{max}^{1-e} - l_{min}^{1-e} \right). \end{aligned} \quad (2.7)$$

Defining the density parameter p as

$$p = \frac{M(L)}{L^2}, \quad (2.8)$$

we have

$$\begin{aligned} M(L) &= pL^2 = N(L) \frac{1}{l_{max}^{-e} - l_{min}^{-e}} \frac{-e}{1-e} (l_{max}^{1-e} - l_{min}^{1-e}), \\ \Rightarrow N(L) &= \frac{e-1}{e} \frac{l_{max}^{-e} - l_{min}^{-e}}{l_{max}^{1-e} - l_{min}^{1-e}} pL^2. \end{aligned} \quad (2.9)$$

2.6.2 Number of Fractures Longer than the System Size

The number of fractures longer than the system size L , $N_{>}$, is given by

$$N_{>} = N(L) [F(l_{max}) - F(L)] = N(L) \frac{l_{max}^{-e} - L^{-e}}{l_{max}^{-e} - l_{min}^{-e}}. \quad (2.10)$$

Substituting for $N(L)$ from equation (2.9), we get

$$N(L) \frac{l_{max}^{-e} - L^{-e}}{l_{max}^{-e} - l_{min}^{-e}} = \frac{e-1}{e} \frac{l_{max}^{-e} - l_{min}^{-e}}{l_{max}^{1-e} - l_{min}^{1-e}} pL^2 \frac{l_{max}^{-e} - L^{-e}}{l_{max}^{-e} - l_{min}^{-e}}, \quad (2.11)$$

$$\Rightarrow N_{>} = \frac{e-1}{e} \frac{l_{max}^{-e} - L^{-e}}{l_{max}^{1-e} - l_{min}^{1-e}} pL^2. \quad (2.12)$$

For $e > 1$,

$$\lim_{l_{max} \rightarrow \infty} N_{>} = \frac{e-1}{e} \frac{L^{-e}}{l_{min}^{1-e}} pL^2 \propto L^{2-e}. \quad (2.13)$$

If $e > 2$, the spanning cluster will be made exclusively of fractures shorter than the lattice size and gas transport to the well will take place through a cluster of numerous short fractures; if $1 < e < 2$, there is a non zero

probability for the occurrence of fractures longer than the lattice size, and transport pathways will be made of, for the most part, a few long fractures. Figure 2.3 shows the topology of the gas transport pathways for $e = 1.5$, 2 and 100.

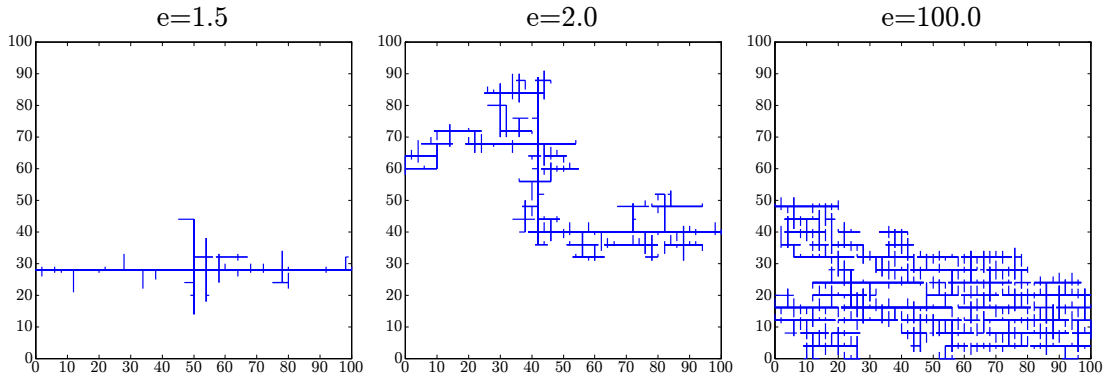


Figure 2.3: For $1 < e < 2$, connectivity between the opposite sides of the lattice is made possible by a few fractures or even a single fracture longer than the lattice size. At $e = 2$, the spanning cluster is made of a mix of long and short fractures. For large e , spanning cluster is made of numerous short fractures.

Based on the histogram of the values of e for various formations, Figure 2.1, which suggests that 1.2 is the most frequently observed value, this dissertation suggests that prior to hydrofracturing and at the percolation threshold, the connected portion of the natural fracture/induced crack network in shales resembles the cluster in the left plot in Figure 2.3.

It should be noted that the presence of a fracture longer than the lattice size in the lattice does not necessarily mean the entire fracture length will exist inside the lattice, but rather that a random point along the fracture has to

exist inside the lattice. The probability of fractures longer than the lattice size is the subject of the next section.

2.6.3 Probability of a Fracture Longer than the System Size

This section answers the following question: if we populate an $L \times L$ square lattice with $n = N(L)$ fractures the lengths of which are randomly drawn from the power law distribution given by equation (2.2), what is the probability $p_{>}$ that at least one of the fractures will be longer than the system size L ?

The probability $p_{>}$ is the sum of the probabilities associated with drawing exactly 1, 2, ..., or n fractures longer than L . Suppose we randomly draw one fracture length from the power law distribution. Let p_0 denote the probability that the length will be shorter than L ; p_1 , the probability that the length is at least L . Then

$$p_{>} = \binom{n}{1} p_1 p_0^{n-1} + \binom{n}{2} p_1^2 p_0^{n-2} + \dots + \binom{n}{n-1} p_1^{n-1} p_0 + p_1^n, \quad (2.14)$$

$$p_{>} = \sum_{k=1}^n \binom{n}{k} p_1^k p_0^{n-k}, \quad (2.15)$$

where

$$p_0 = F(L) = \frac{L^{-e} - l_{min}^{-e}}{l_{max}^{-e} - l_{min}^{-e}}, \quad (2.16)$$

$$p_1 = 1 - F(L) = \frac{l_{max}^{-e} - L^{-e}}{l_{max}^{-e} - l_{min}^{-e}}, \quad (2.17)$$

Using the binomial theorem,

$$(1 + x)^n = \sum_{k=0}^n \binom{n}{k} x^k, \quad (2.18)$$

we simplify equation (2.15) to obtain

$$p_{>} = 1 - p_0^n = 1 - F(L)^{N(L)}, \quad (2.19)$$

where $F(L)$ is given by equation (2.2),

$$F(L) = \frac{L^{-e} - l_{min}^{-e}}{l_{max}^{-e} - l_{min}^{-e}},$$

and $N(L)$ is given by equation (2.9),

$$N(L) = \frac{e - 1}{e} \frac{l_{max}^{-e} - L^{-e}}{l_{max}^{1-e} - l_{min}^{1-e}} pL^2.$$

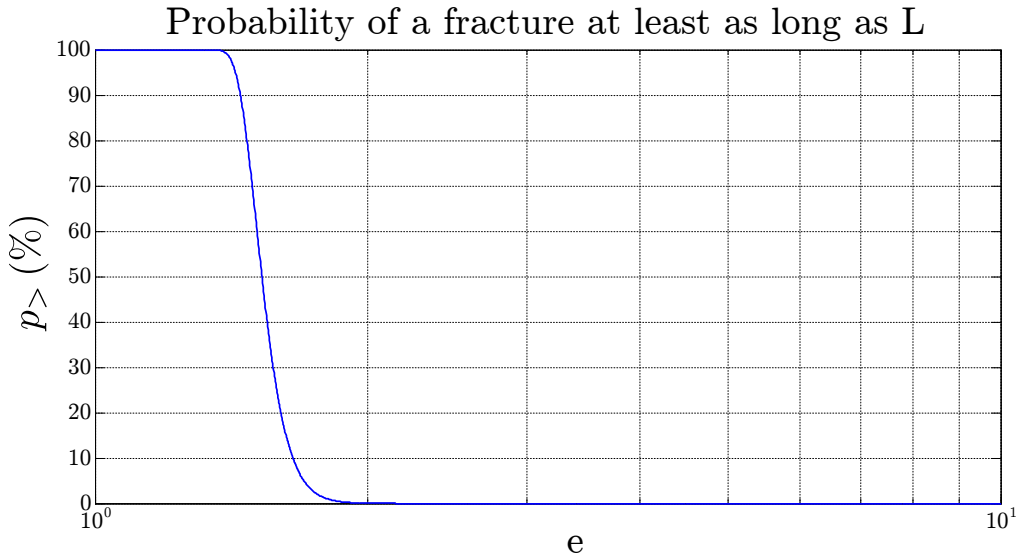


Figure 2.4: $p_{>}$ plotted for $l_{max} = 10^{14}$, $L = 10^7$, $l_{min} = a = 1$, $p = 10^{-3}$.

2.7 Numerical Computation of the Percolation Threshold

Percolation threshold p_c is the concentration p at which an infinite cluster appears for the time in an *infinite* lattice (Stauffer and Aharony, 1992). In the case of finite lattices, however, the spanning cluster may appear for the first time at a value of p that is lower or greater than p_c . Numerical computation of the percolation threshold involves computing an “effective” threshold at multiple lattice sizes and extrapolating to infinite size (Stauffer and Aharony, 1992).

For the classical bond percolation problem, Stauffer and Aharony (1992) have presented an efficient algorithm to compute the concentration p at which a lattice of size L percolates for the first time (“apparent” threshold from now on). Unlike the classical bond percolation problem where all bonds are identical, length of fractures in the present research are variable. We modify the algorithm to extend its application to the case of lattices populated with fractures of different size.

2.7.1 The Algorithm to Determine the Apparent Threshold for a Lattice of Size L

Because the configuration of the lattice is symmetric about the threshold, the concentration at which the lattice percolates for the first time can be viewed as either of the following:

1. If one gradually removes fractures from a lattice above the threshold

until the lattice transitions from percolation to no percolation, the concentration at which the transition happens is the apparent threshold.

2. If one gradually adds fractures to a lattice below the threshold until the lattice transitions from no percolation to percolation, the concentration at which the transition happens is the apparent threshold.

Although the two views are mathematically identical, there is significant computational advantage in adopting the first view, because adding fractures to an already populated lattice requires merging the fractures that overlap with pre-existing fractures and takes considerably longer than only removing fractures from the lattice.

The algorithm due to Stauffer and Aharony (1992) first checks $p = \frac{1}{2}$ for percolation. If the lattice percolates, p is decreased by $\frac{1}{4}$; if not, p is increased by $\frac{1}{4}$, then the percolation status is checked. If the lattice percolates, p is decreased by $\frac{1}{8}$; if not, p is increased by $\frac{1}{8}$, then the percolation status is checked. This process is repeated until the apparent threshold is determined with sufficient accuracy.

Whether a given populated lattice percolates or not is determined in this work by a cluster counting algorithm based on the algorithm introduced by Hoshen and Kopelman (1976) and the extension due to Al-Futaisi and Patzek (2003). The algorithm can label all clusters after one sweep through the lattice.

Similar to the algorithm due to Stauffer and Aharony (1992), the main idea of the algorithm used in the present research is to identify an interval $[p_{lb}, p_{ub}]$ which includes the apparent threshold, and then shrink the interval until the apparent threshold is known with sufficient accuracy. The upper bound, p_{ub} , corresponds to a concentration at which the lattice has already percolated; the lower bound, p_{lb} , corresponds to a concentration at which the lattice does not percolate.

Unlike the algorithm due to Stauffer and Aharony, the algorithm used in this work computes the apparent threshold by *only removing* fractures from a lattice which has already percolated. For a given lattice size L and exponent e , we first determine through trial and error a concentration at which the lattice has already percolated and record the value in p_{ub} . This concentration is usually close to $p = 0.5$, but it can be larger or smaller. The apparent threshold is now known to belong to $[p_{lb} = 0, p_{ub}]$. We now remove enough fractures from the lattice at p_{ub} to obtain a concentration close to $p_{mean} = \frac{p_{lb} + p_{ub}}{2}$. If at p_{mean} the lattice percolates, then apparent threshold has to be in $[p_{lb}, p_{mean}]$ and p_{ub} will be updated to p_{mean} ; if not, the threshold is in $[p_{mean}, p_{ub}]$ and p_{lb} will be updated to p_{mean} . This process is repeated until p_{ub} and p_{lb} are closer than an allowable tolerance, Δp_{tol} .

The change in concentration p when a randomly chosen fracture is removed from the populated lattice, Δp , depends on the length of the fracture.

If the total number of bonds in the lattice is N_b , then

$$\Delta p_{min} = \frac{a}{N_b}, \quad (2.20)$$

where a , the lattice spacing, is the minimum fracture length. Δp_{min} is the precision of the algorithm presented here.

The allowable tolerance is the change in concentration associated with removing the longest fracture which can fit in the lattice:

$$\Delta p_{tol} = \Delta p_{max} = \frac{L}{N_b}. \quad (2.21)$$

The algorithm converges to the apparent threshold in fewer than 10 steps.

2.7.2 Extrapolating the Apparent Threshold to Infinite Size

We consider the following exponents: $e = 1, 1.4, 1.6, 1.8, 2.2, 2.6, 3, 5, 10, 100$. For each value of e , we compute the apparent threshold for each of the following lattice sizes, scaled with the lattice spacing, $a = 1$: $L = 25, 50, 100, 125, 150, 175, 200$.

We use the algorithm described in section 2.7.1 and determine the apparent threshold 100 times for each value of e and L , in general getting a different value for the apparent threshold every time. The apparent threshold at L and e is taken to be the average of the 100 runs and is denoted p_{av} .

For each value of the exponent, Figure 2.5 shows the cumulative density functions (CDFs) of the apparent thresholds computed for each of the lattice sizes.

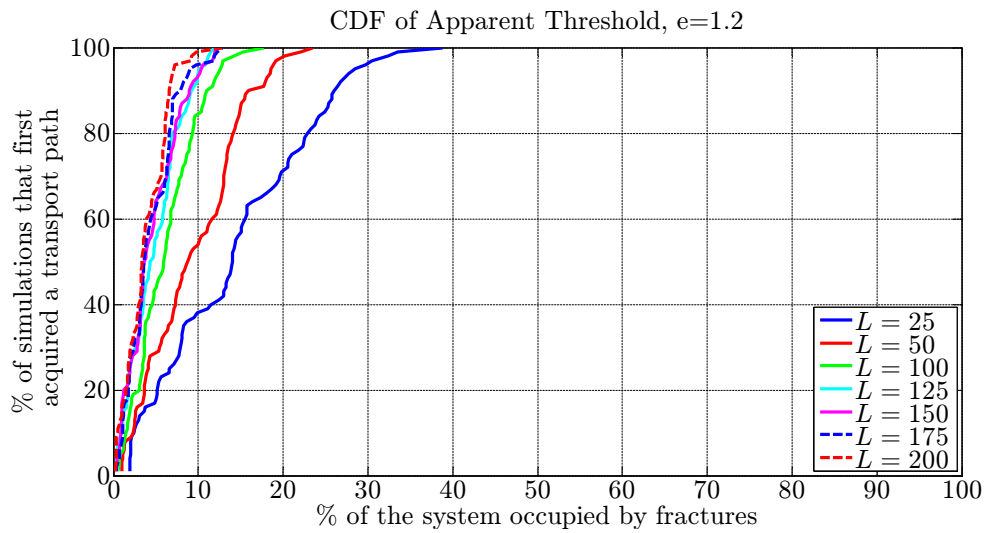
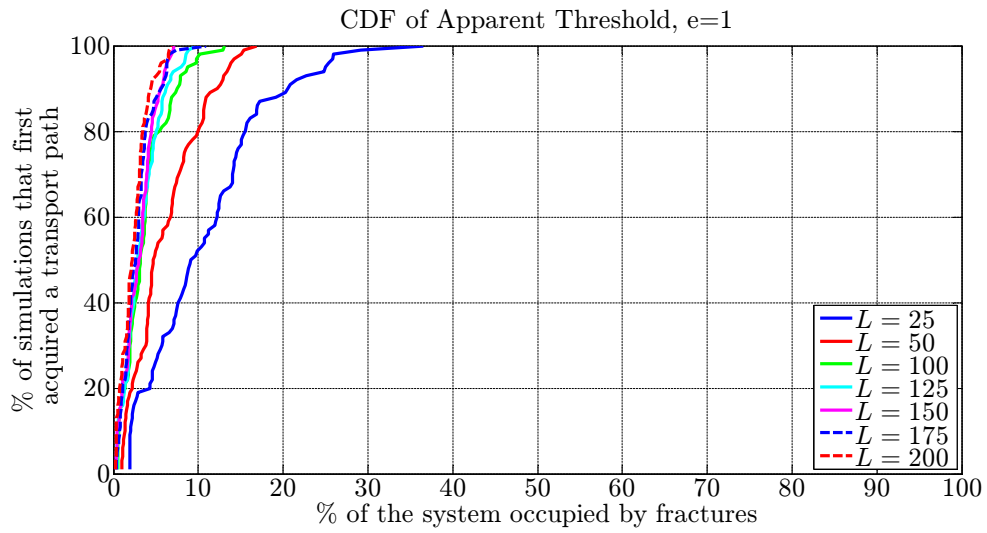


Figure 2.5: Cumulative density function of the apparent threshold, obtained for lattices of different size L and at the power law exponents $e = 1$ and $e = 1.2$.

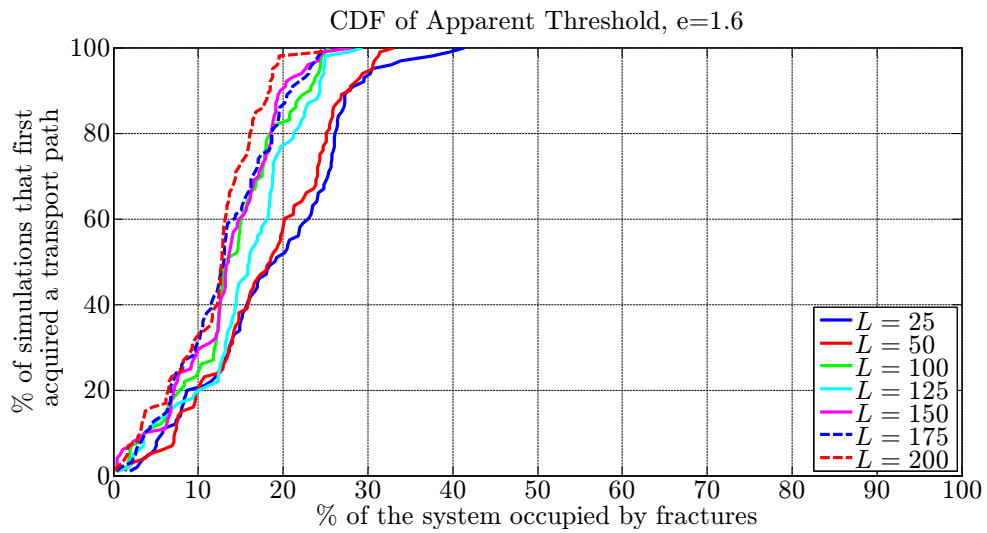
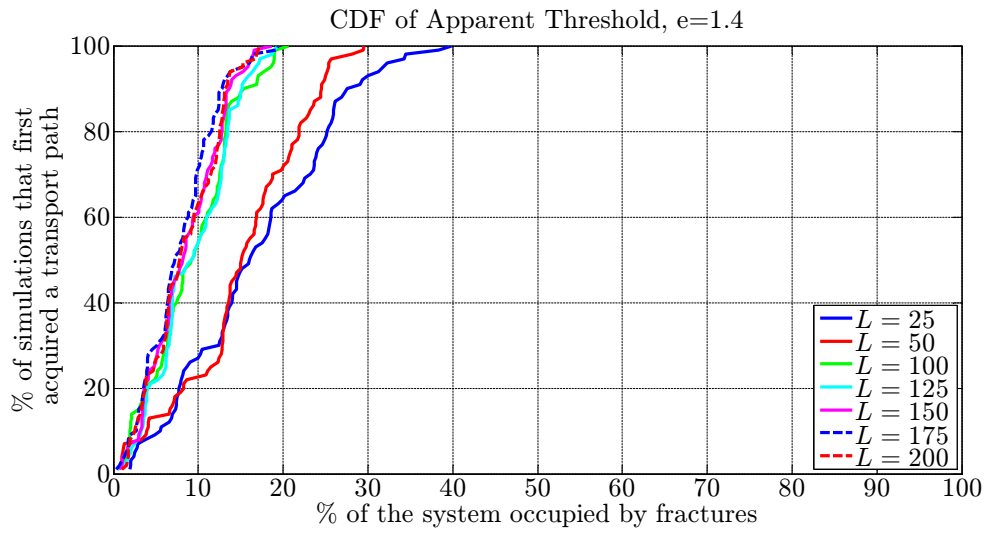


Figure 2.5 (cont.): Cumulative density function of the apparent threshold, obtained for lattices of different size L and at the power law exponents $e = 1.4$ and $e = 1.6$.

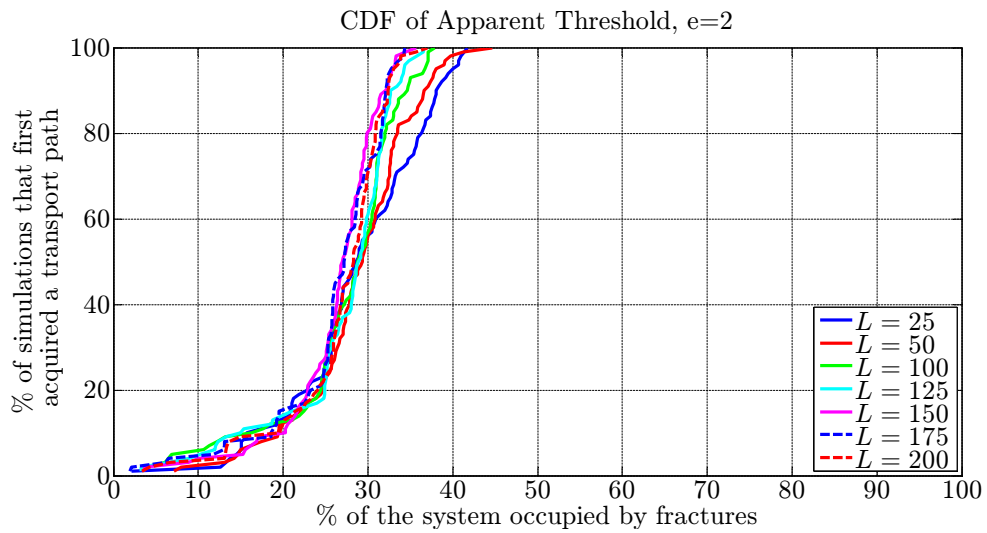
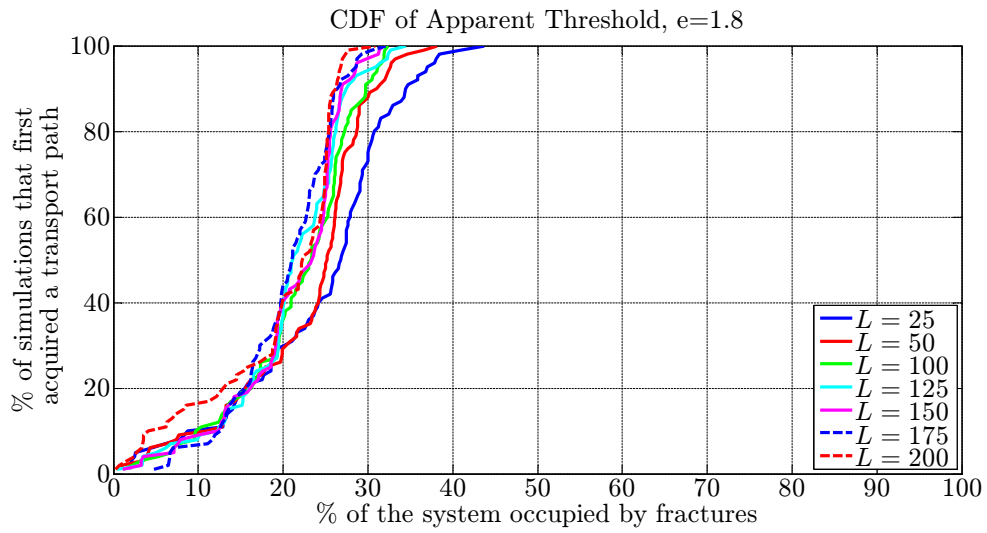


Figure 2.5 (cont.): Cumulative density function of the apparent threshold, obtained for lattices of different size L and at the power law exponents $e = 1.8$ and $e = 2$.

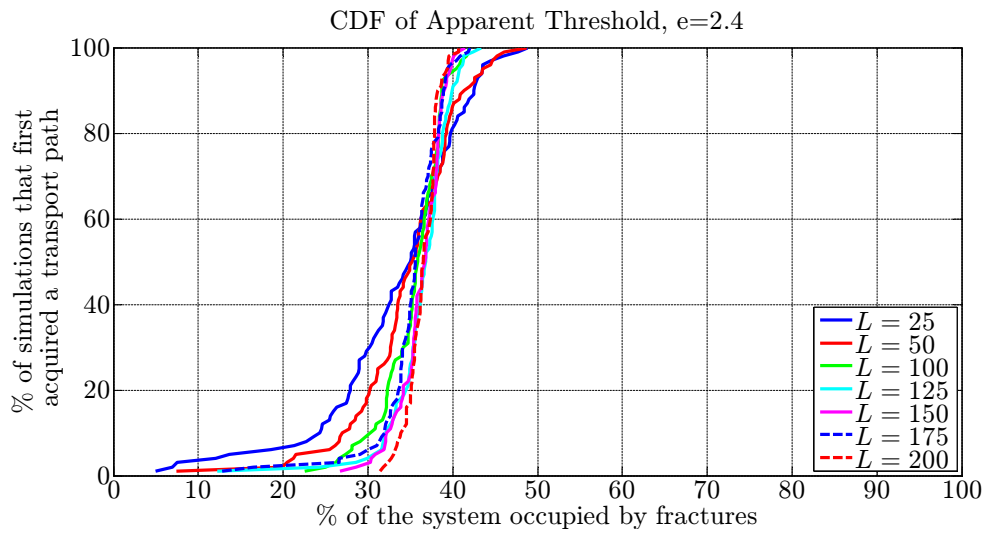
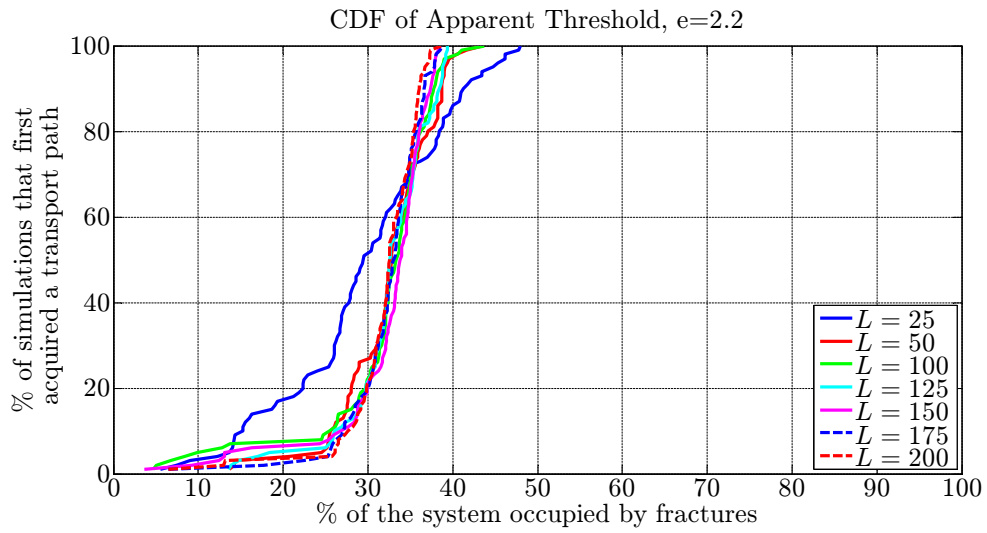


Figure 2.5 (cont.): Cumulative density function of the apparent threshold, obtained for lattices of different size L and at the power law exponents $e = 2.2$ and $e = 2.4$.

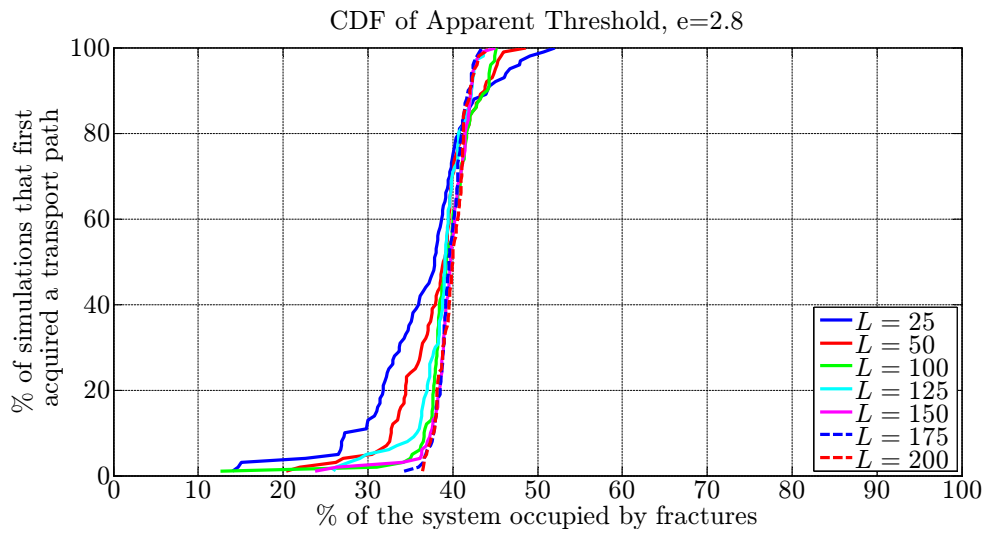
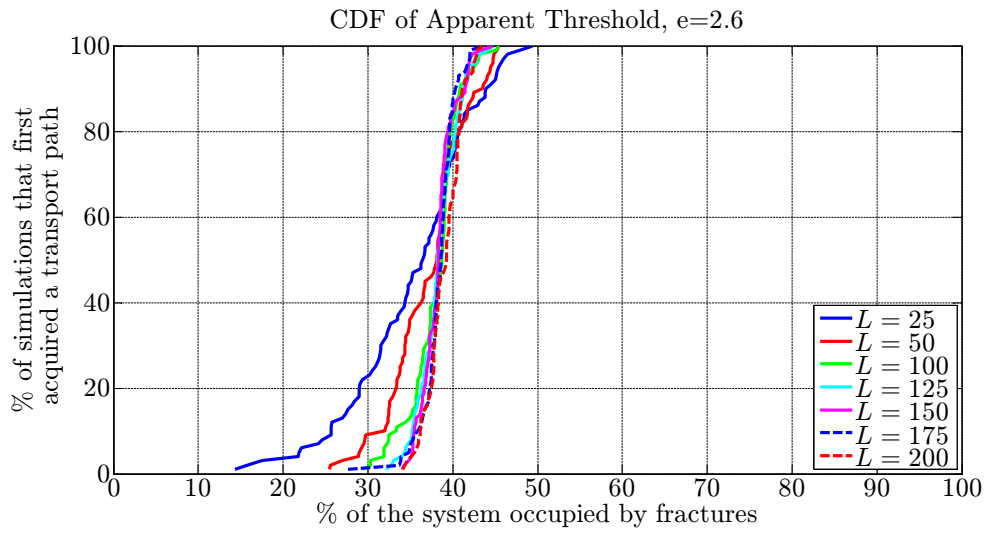


Figure 2.5 (cont.): Cumulative density function of the apparent threshold, obtained for lattices of different size L and at the power law exponents $e = 2.6$ and $e = 2.8$.

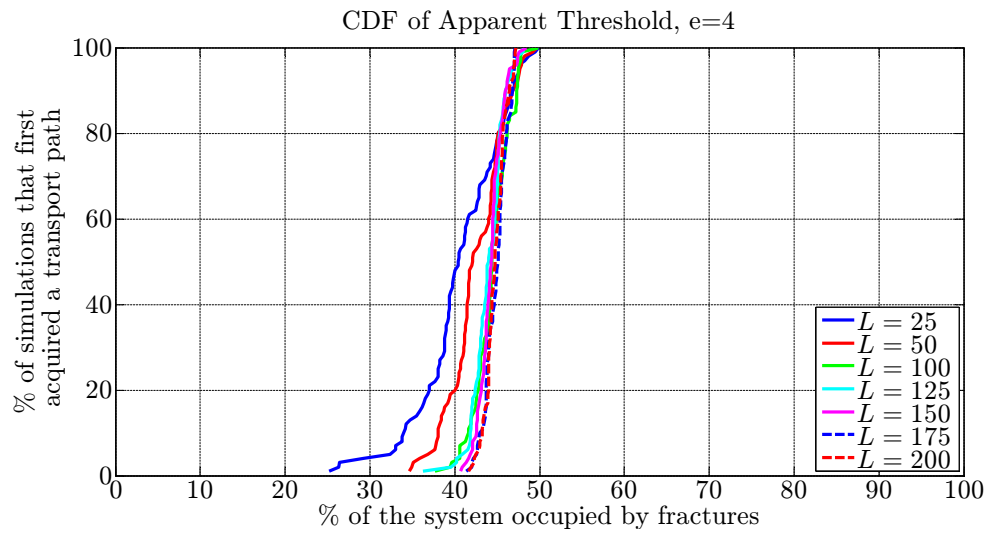
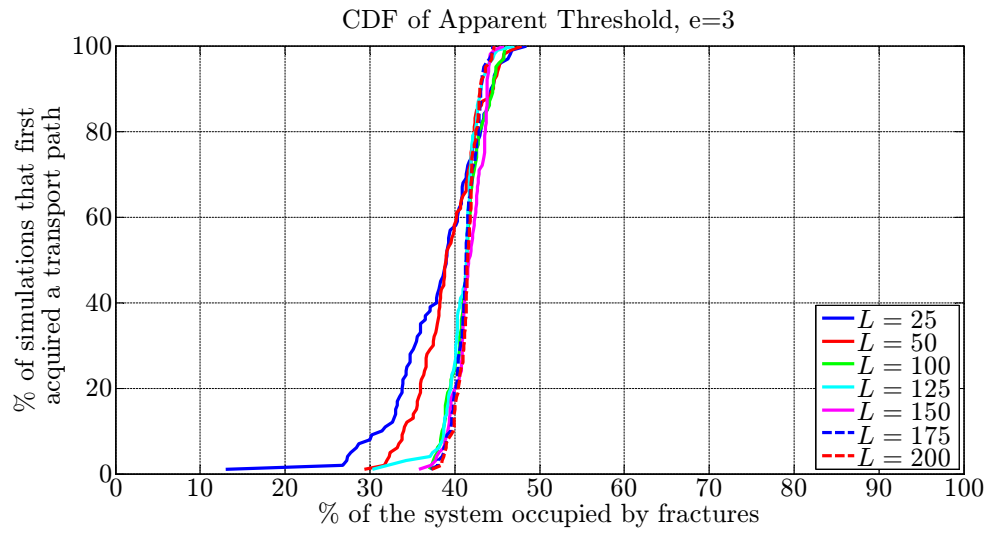


Figure 2.5 (cont.): Cumulative density function of the apparent threshold, obtained for lattices of different size L and at the power law exponents $e = 3$ and $e = 4$.

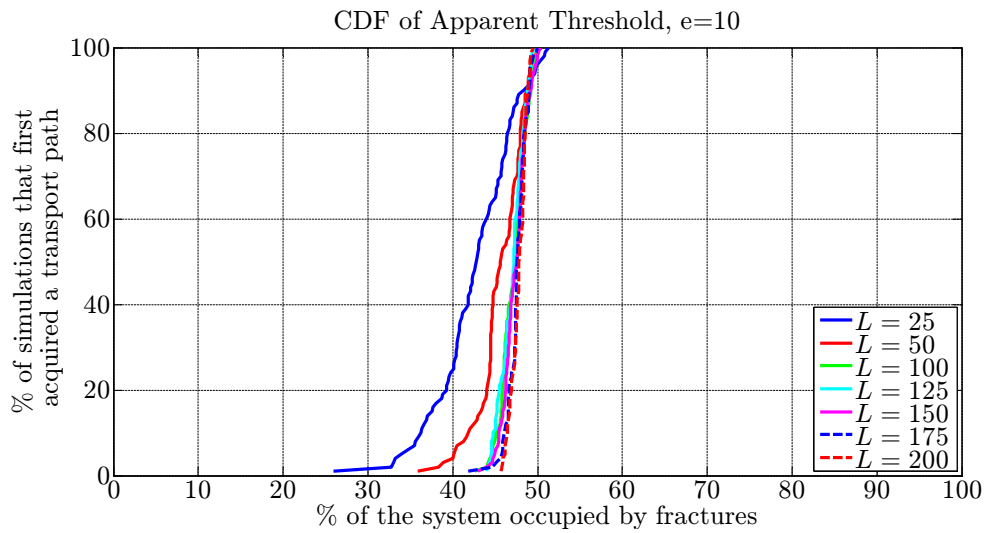
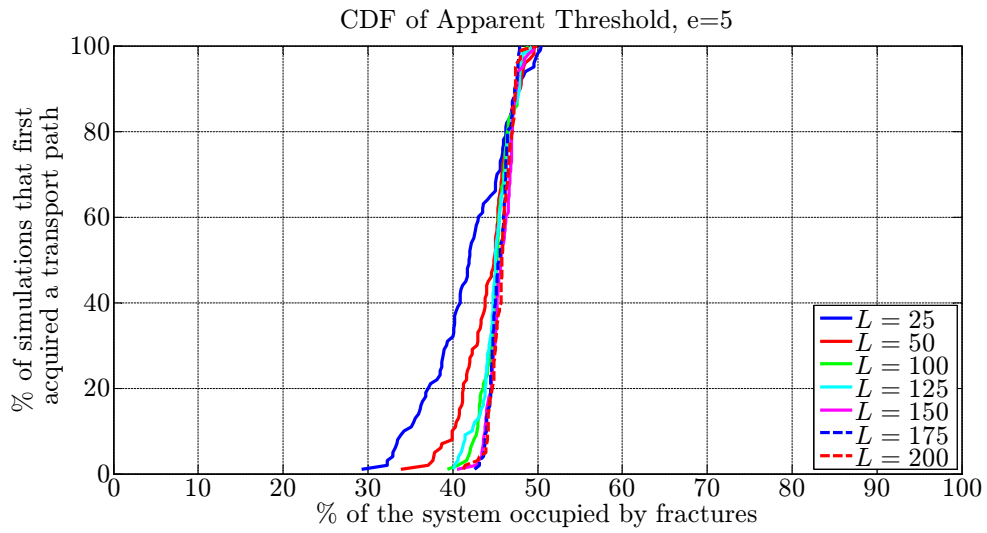


Figure 2.5 (cont.): Cumulative density function of the apparent threshold, obtained for lattices of different size L and at the power law exponents $e = 5$ and $e = 10$.

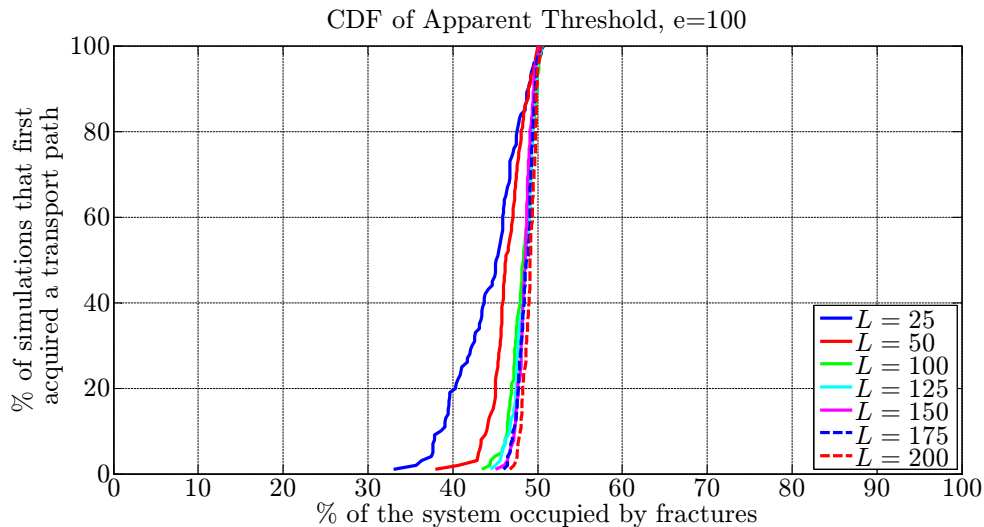


Figure 2.5 (cont.): Cumulative density function of the apparent threshold, obtained for lattices of different size L and at the power law exponent $e = 100$. At each e , the width of the transition zone from 0 to 100% gets smaller with increasing L ; in the limit of $L \rightarrow \infty$, the cumulative density function becomes a step function at the percolation threshold. Increasing e narrows the fracture length distribution; in the limit of $e \rightarrow \infty$, the length of all fractures becomes equal to l_{min} and the problem is reduced to bond percolation, for which the percolation threshold is 50%. Therefore, increasing e and L moves the cumulative density plots towards a step function at 50%.

At a given e , the transition from not getting a transport path in any of the simulations (0 on the vertical axis) to always getting one (100% on the vertical axis) gets sharper with increasing system size, in agreement with percolation theory. Another observation is that increasing the exponent causes a gradual movement of all the plots towards 50% on the horizontal axis, which is the classical bond percolation threshold. This observation is consistent with the analysis at the end of section §2.5: in the limit of $e \rightarrow \infty$, length of all fractures becomes equal to the minimum fracture length and the problem is

reduced to the classical bond percolation problem.

Scaling of p_{av} for each value of e is shown in Figure 2.6, where p_{av} is plotted against $\frac{1}{L}$. The error bars show the standard error associated with averaging the 100 runs at each system size. The intercept of the plot is the percolation threshold p_c .

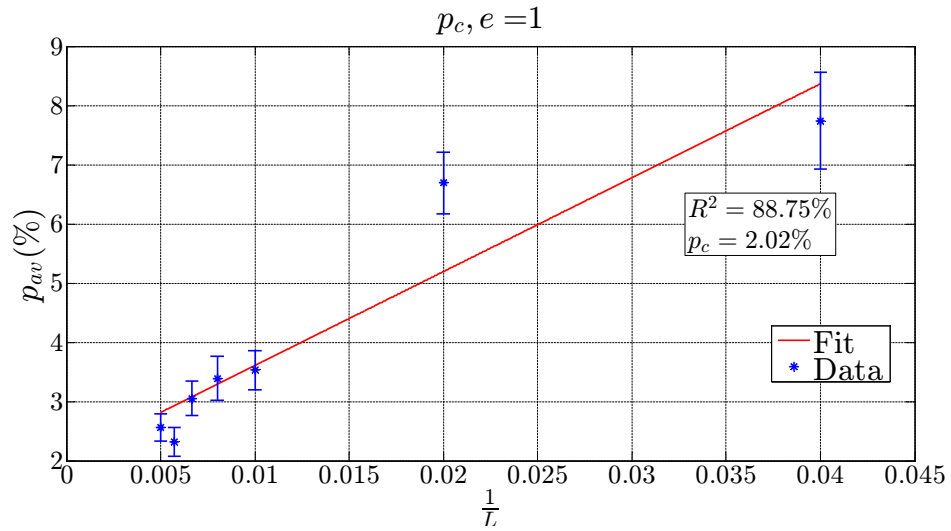


Figure 2.6: The numerical procedure to compute the percolation threshold p_c at the power law exponent $e = 1$. The numerically obtained apparent thresholds (p_{av}) for different sizes are extrapolated to infinite size ($\frac{1}{L} \rightarrow 0$); p_c is the intercept. The blue bar on each data point indicates the standard error.

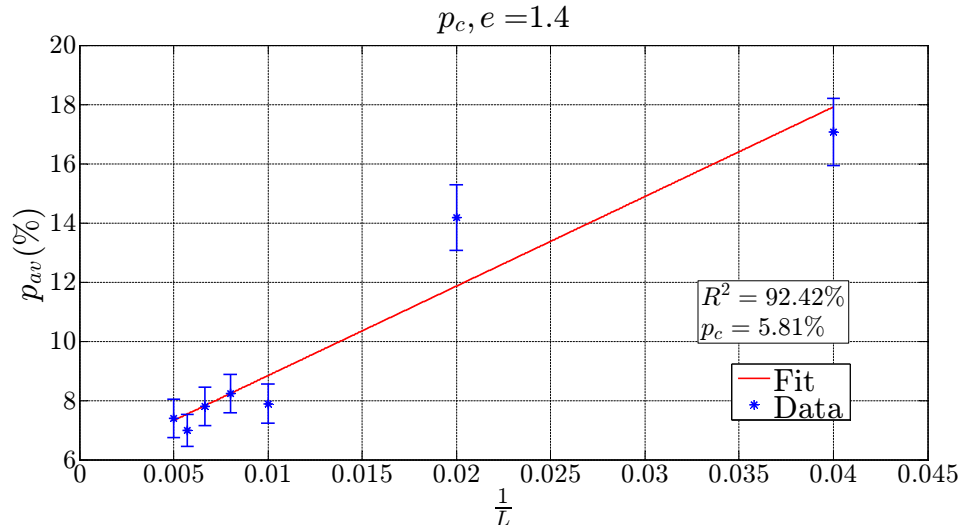
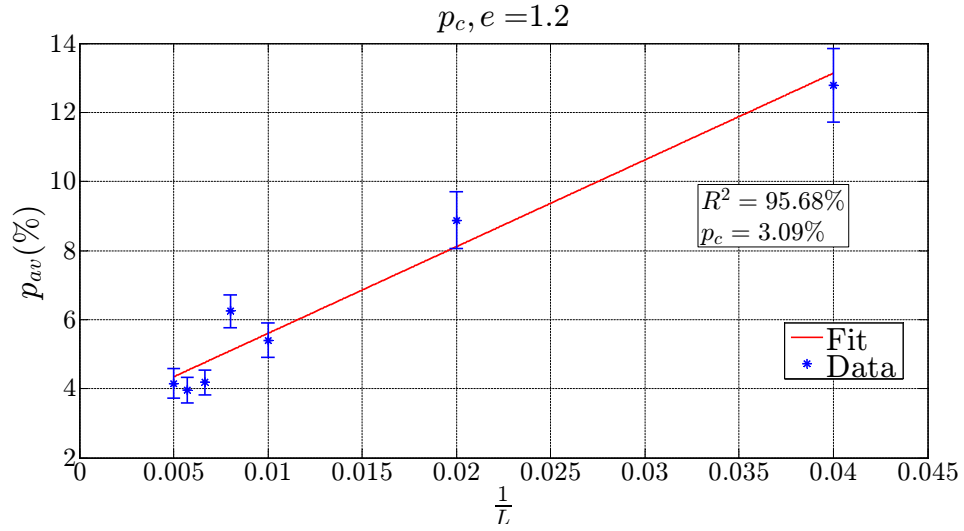


Figure 2.6 (cont.): The numerical procedure to compute the percolation threshold p_c at the power law exponents $e = 1.2$ and $e = 1.4$. The numerically obtained apparent thresholds (p_{av}) for different sizes are extrapolated to infinite size ($\frac{1}{L} \rightarrow 0$); p_c is the intercept. The blue bar on each data point indicates the standard error.

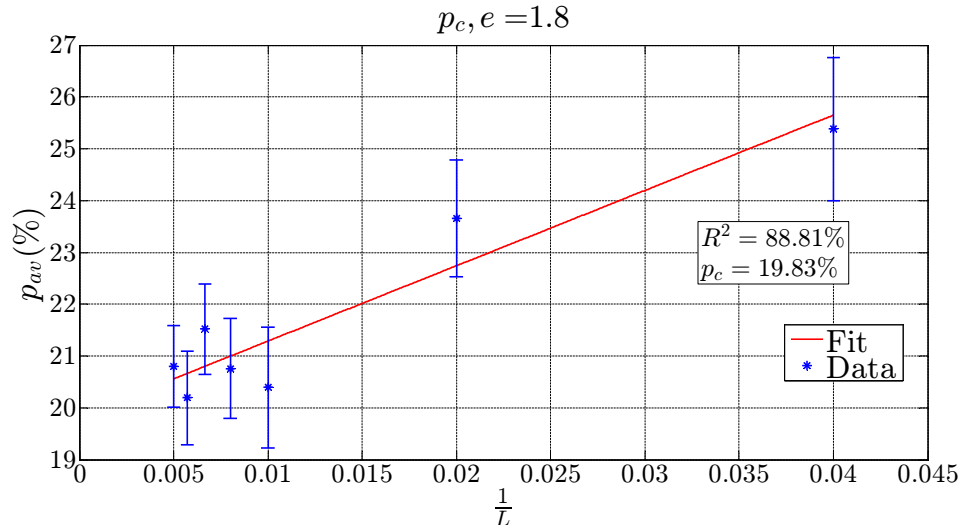
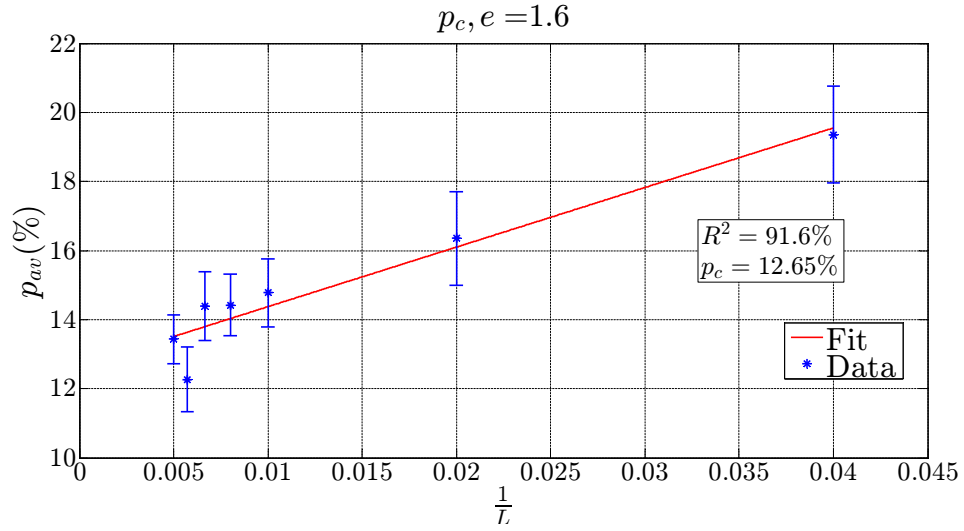


Figure 2.6 (cont.): The numerical procedure to compute the percolation threshold p_c at the power law exponents $e = 1.6$ and $e = 1.8$. The numerically obtained apparent thresholds (p_{av}) for different sizes are extrapolated to infinite size ($\frac{1}{L} \rightarrow 0$); p_c is the intercept. The blue bar on each data point indicates the standard error.

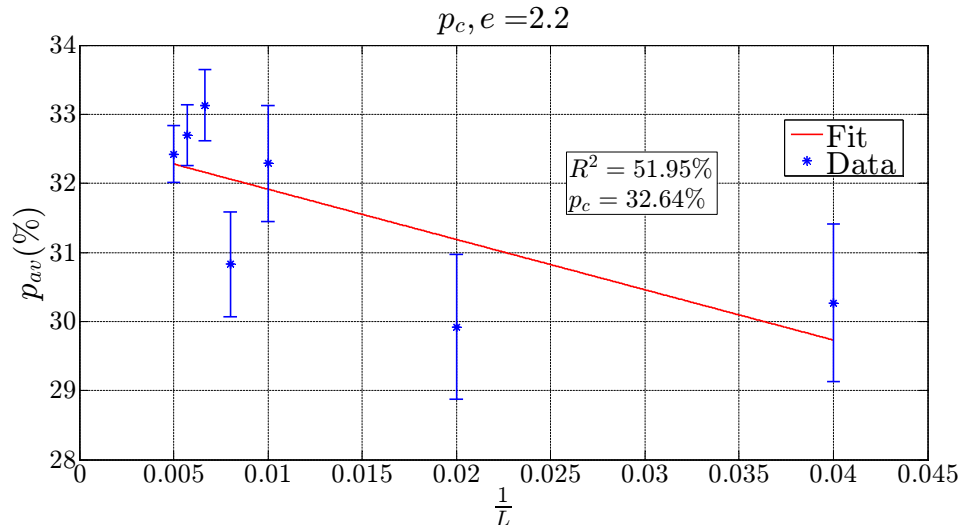
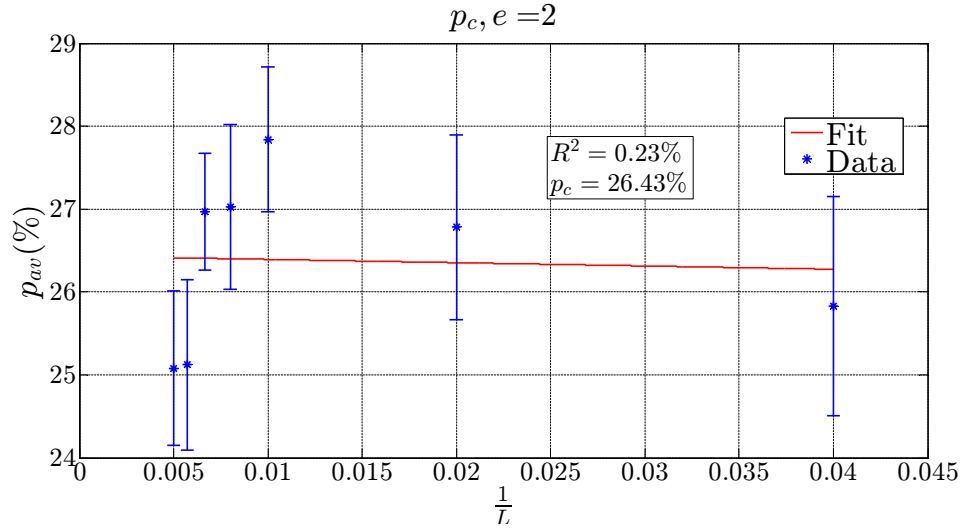


Figure 2.6 (cont.): The numerical procedure to compute the percolation threshold p_c at the power law exponents $e = 2$ and $e = 2.2$. The numerically obtained apparent thresholds (p_{av}) for different sizes are extrapolated to infinite size ($\frac{1}{L} \rightarrow 0$); p_c is the intercept. The blue bar on each data point indicates the standard error.

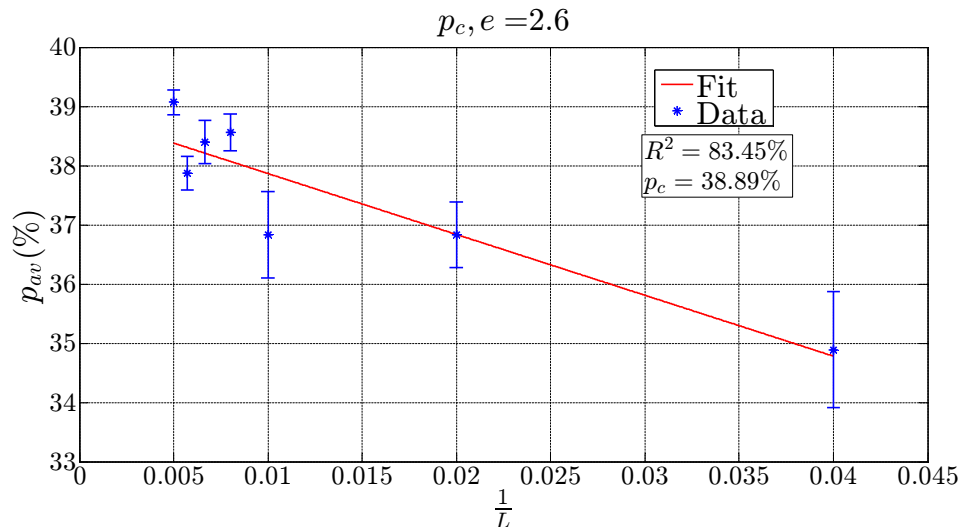
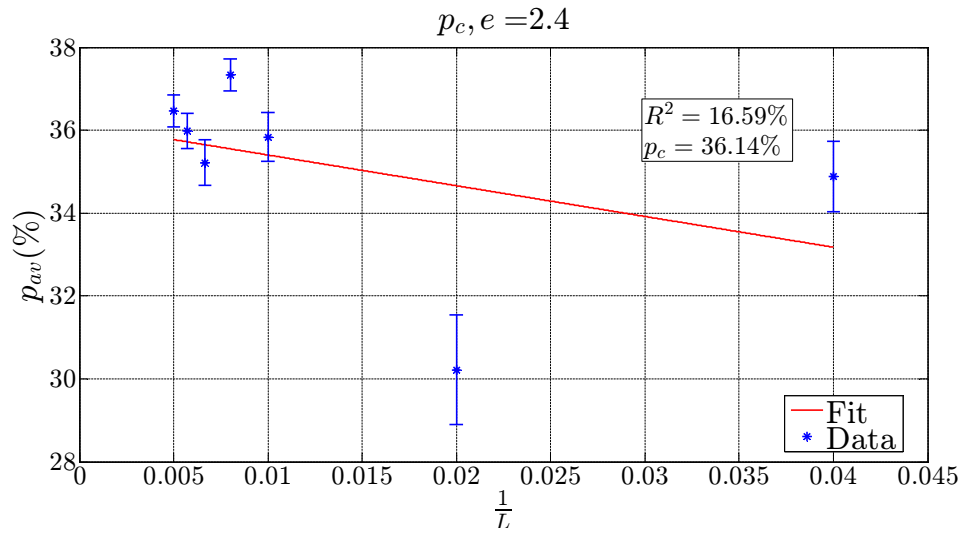


Figure 2.6 (cont.): The numerical procedure to compute the percolation threshold p_c at the power law exponents $e = 2.4$ and $e = 2.6$. The numerically obtained apparent thresholds (p_{av}) for different sizes are extrapolated to infinite size ($\frac{1}{L} \rightarrow 0$); p_c is the intercept. The blue bar on each data point indicates the standard error.

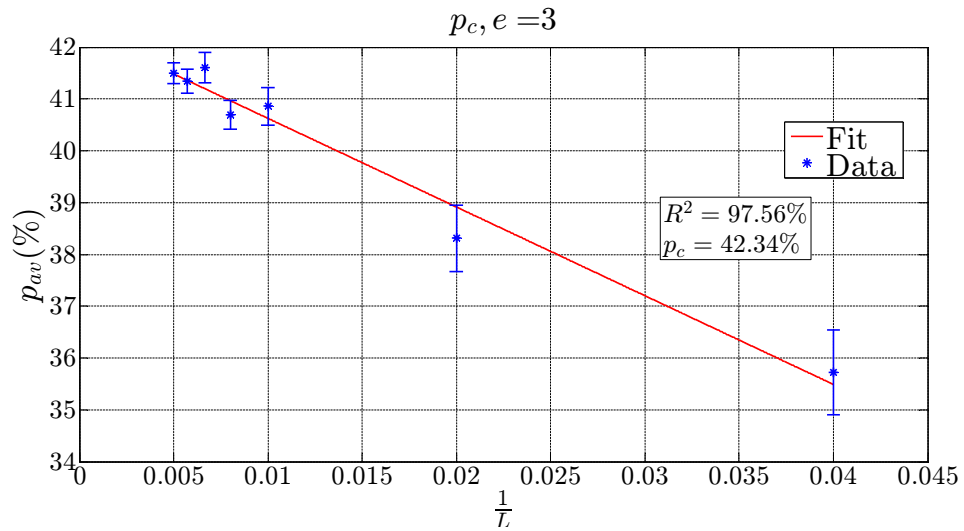
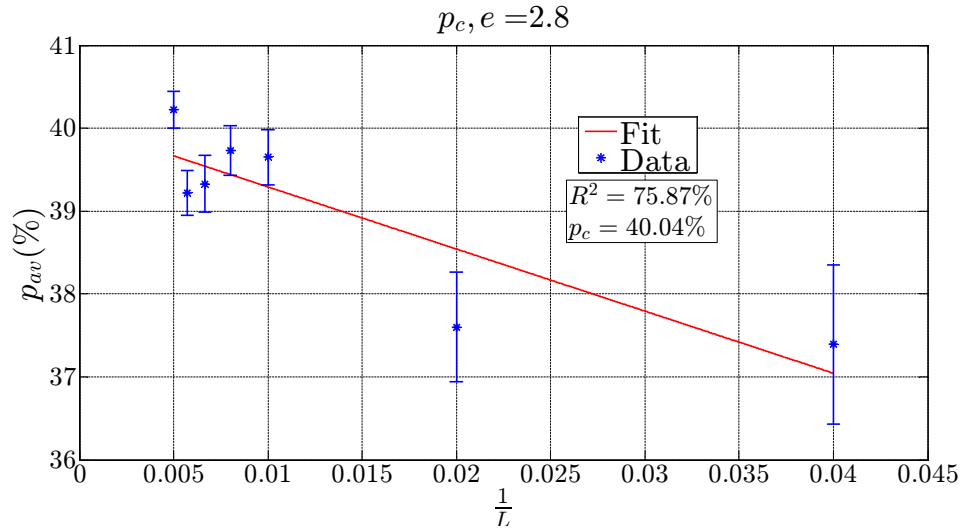


Figure 2.6 (cont.): The numerical procedure to compute the percolation threshold p_c at the power law exponents $e = 2.8$ and $e = 3$. The numerically obtained apparent thresholds (p_{av}) for different sizes are extrapolated to infinite size ($\frac{1}{L} \rightarrow 0$); p_c is the intercept. The blue bar on each data point indicates the standard error.

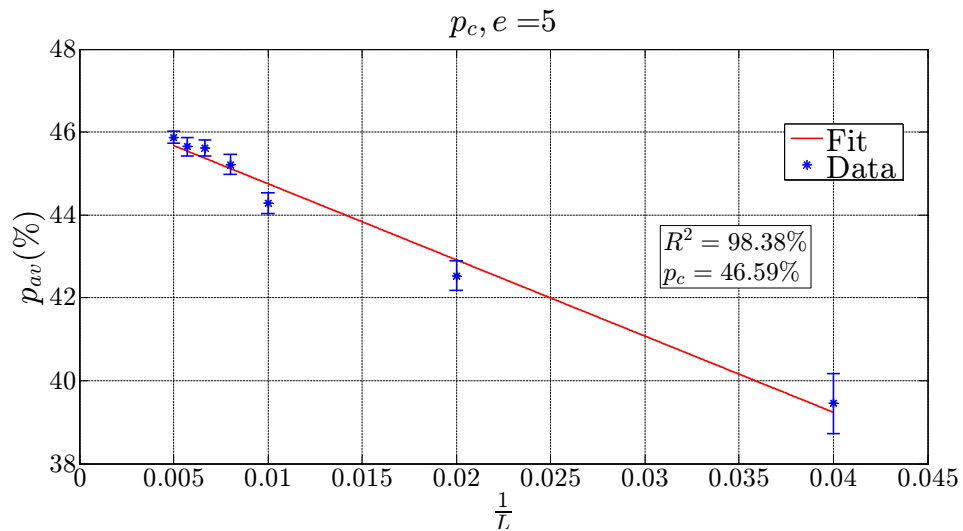
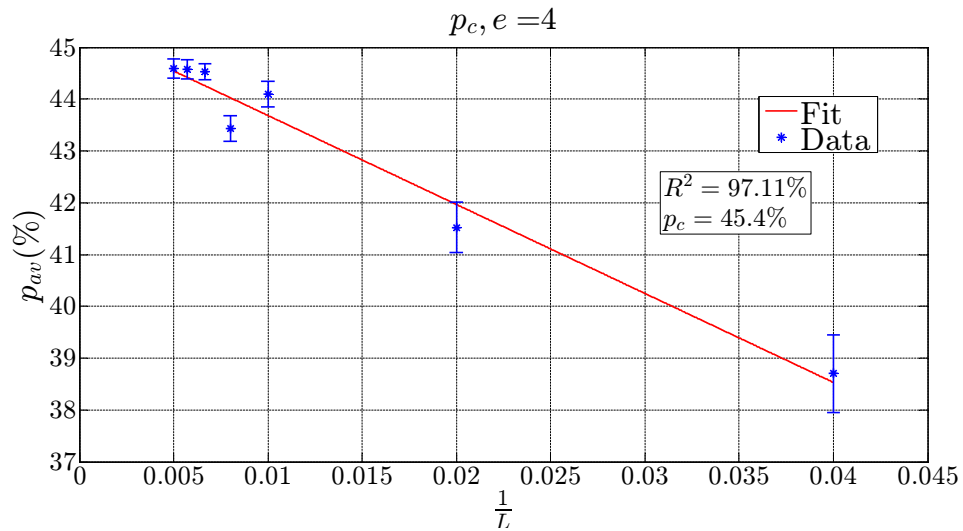


Figure 2.6 (cont.): The numerical procedure to compute the percolation threshold p_c at the power law exponents $e = 4$ and $e = 5$. The numerically obtained apparent thresholds (p_{av}) for different sizes are extrapolated to infinite size ($\frac{1}{L} \rightarrow 0$); p_c is the intercept. The blue bar on each data point indicates the standard error.

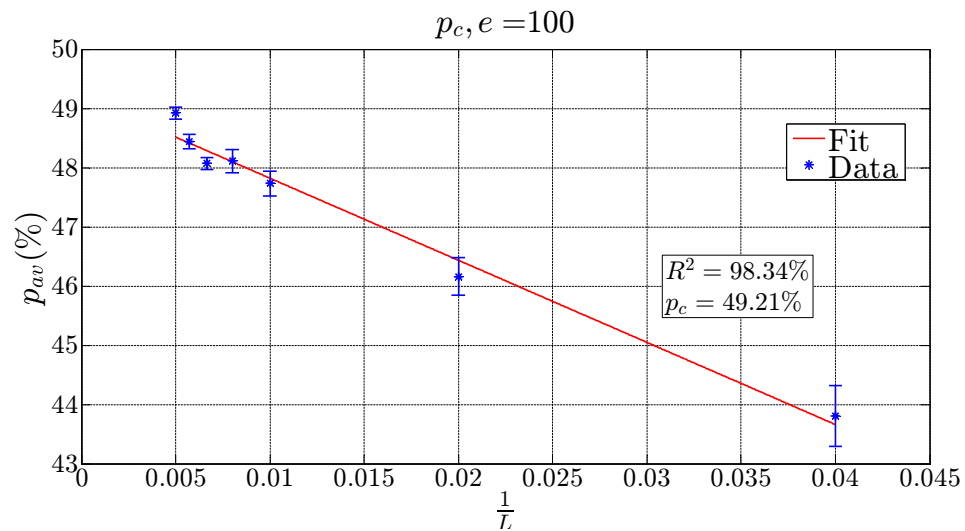
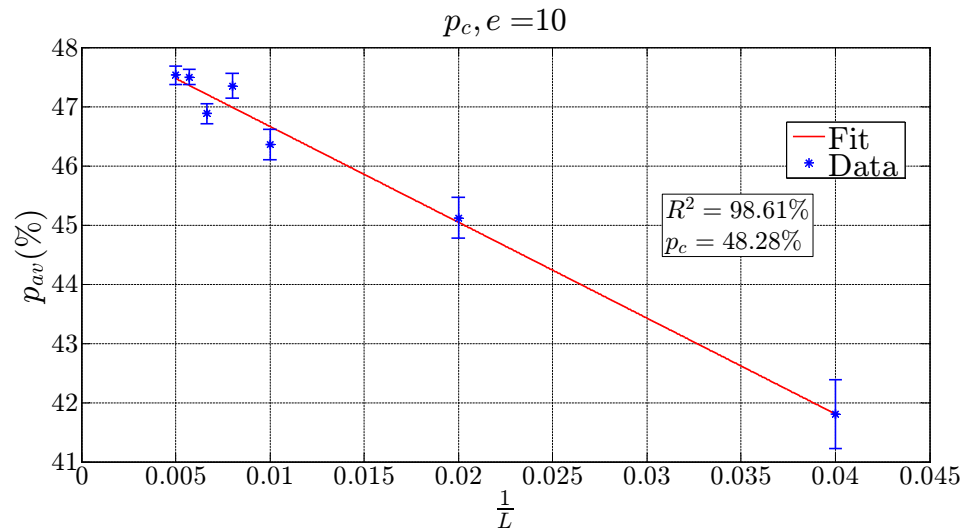


Figure 2.6 (cont.): The numerical procedure to compute the percolation threshold p_c at the power law exponents $e = 10$ and $e = 100$. The numerically obtained apparent thresholds (p_{av}) for different sizes are extrapolated to infinite size ($\frac{1}{L} \rightarrow 0$); p_c is the intercept. The blue bar on each data point indicates the standard error.

Percolation threshold as a function of exponent can be viewed in Figure 2.7. The sharp change in the threshold at around $e = 2$ agrees with the scaling relationship given by equation (2.13).

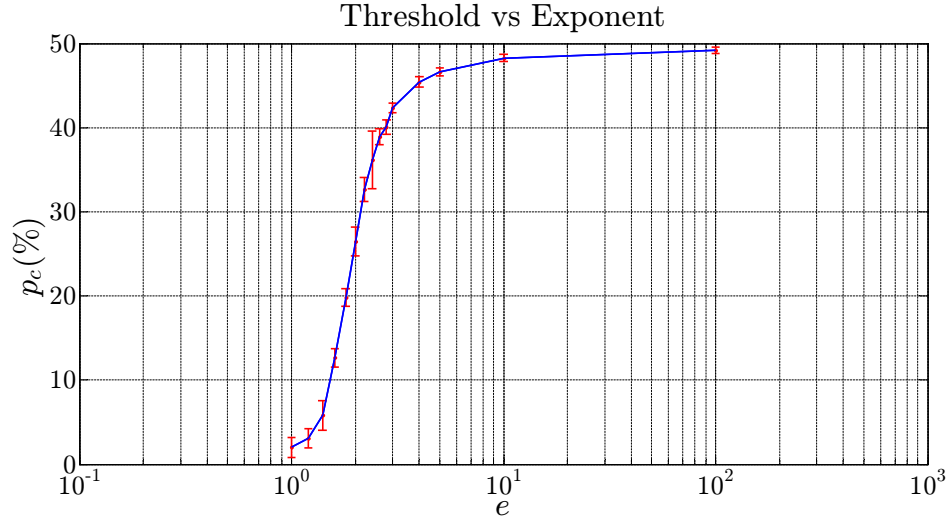


Figure 2.7: Percolation threshold p_c as a function of the exponent e .

In the present research, percolation threshold is expressed as a critical bond concentration, identical to the original definition of p_c in the classical bond percolation problem. Using this definition, our model predicts the percolation threshold to depend upon the exponent e in the manner shown in Figure 2.7. Bour and Davy (1997) use a different definition of the percolation parameter p , namely

$$p = \frac{\sum_i^N l_i^2}{L^2}, \quad (2.22)$$

where L is the domain size, N is the number of fractures in the domain and l_i is the length of the i -th fracture. Consequently, the percolation threshold

due to Bour and Davy (1997) turns out to be independent of the exponent or system size, and always equal to around 5.6.

2.8 Conclusions

The natural fracture/incipient crack system of shales has been modeled in this chapter as a random population of lines on a two-dimensional square lattice (section §2.5). Based on geological observations, fracture length has been taken to follow a power law distribution characterized by an exponent e . A scaling relationship describing the number of fractures longer than the lattice size as a function of e and the lattice size has been derived in section 2.6.2. The relationship shows that depending on e , connectivity happens due to either clustering of fractures shorter than lattice size ($e > 2$), or presence of a few fractures or even a single fracture of a size comparable to or longer than the lattice size, which can directly connect the opposite sides of the lattice ($1 < e < 2$). The probability of at least one fracture longer than the lattice size has been derived in section 2.6.3.

Percolation threshold as a function of e has been computed numerically and the result agrees with the theoretical scaling predicted in this work: for $1 < e < 2$, the threshold is close to 0; for $e > 2$, the threshold rapidly increases and asymptotically converges to 50% as $e \rightarrow \infty$.

This chapter presented a model of the topology of the natural fracture/incipient crack system of shales. Production from hydraulically fractured shales comes from that subset of the natural fracture/incipient crack system

which gets opened by the fracturing fluid. A geomechanical model of hydraulic fracture is required to determine the interaction between hydraulic fractures and the natural fracture/incipient crack system. Such a model is the subject of the next chapter.

Chapter 3

Numerical Modeling of Hydraulic Fractures

3.1 Introduction

So far in this dissertation, we have established that gas production from hydraulically fractured shales has to come from a network of connected natural fractures/incipient cracks and/or hydraulic fractures (Chapter 1), and we have described the topology of the connected portion (“spanning cluster”) of the natural fracture/incipient crack system in shales (Chapter 2).

The work presented in the previous chapters suggests that the fracture network responsible for shale gas production is made of those natural fractures/incipient cracks which belong to the spanning cluster and are opened by the fracturing fluid during the treatment (section §2.5). We suggested that hydraulic fractures will be contained inside the spanning cluster, which means that the spanning cluster contains every possible path the hydraulic fractures may take.

With the topology of the spanning cluster known, we now move on to the mechanics of hydraulic fracture and present in this chapter a numerical model of how network geometry is created during a hydraulic fracture treatment. The model can simulate initiation and propagation of hydraulic

fractures and makes it possible to establish which natural fractures/incipient cracks of the spanning cluster will be opened by the fracturing fluid.

For a given hydraulic fracture treatment in a given shale, the ultimate outcome of the model is the fracture network responsible for gas production. The model also captures the time evolution of the network from the start of injection to the end of treatment. We are particularly interested in identifying the characteristics of the network and ultimately describing how they affect production. The model in this chapter provides the network; production computations will be presented later and in Chapter 4.

The model employs the Reynolds lubrication approximation to simulate fluid flow through fractures. Flow is then coupled with an *estimate* of the elastic response, provided by the analytical expressions which describe fractures of the Perkins-Kern-Nordgren setup. The choice to approximate the elastic response and not implement a highly detailed numerical scheme (for instance some version of the finite element method or the boundary element method) has been made in favor of computational efficiency: the capability to simulate the interaction of hydraulic fractures with a large number of natural fractures/incipient cracks in an efficient fashion has been the primary design objective here.

3.2 Outline

We start this chapter with a review of the relevant literature. Formal statement of the fluid-driven fracture problem, the standard approach to

hydrofracture modeling, and classic models from the literature are reviewed. We then present the setup of our hydrofracture model, followed by validation against theory. We conclude the chapter by discussing the qualitative phenomena observed during simulations.

3.3 Background & Literature Review

Before discussing the equations which govern hydraulic fractures, we introduce fluid-driven fractures with a qualitative description. In fluid-driven fractures, fluid pressure acts normal to the fracture walls from inside the fracture, compresses the fracture medium and causes deformation. (In this dissertation, the fracture medium is the shale reservoir.) The magnitude of the resulting deformation depends on the mechanical properties of the medium, and in turn determines the fluid pressure inside the fracture. Any description of fluid-driven fractures, numerical or analytical, has to couple the elastic response of the fracture medium with the fluid flow through the fracture.

While coupling the fluid flow with the elastic response enables a hydrofracture model to describe the *current* state of a hydraulic fracture, simulating fracture propagation requires the addition of a fracture mechanics propagation criterion to the model. A few such criteria are commonly used in present day hydrofracture models, and will be reviewed in detail later.

Most of the hydraulic fracturing research today relies on a variety of numerical schemes to solve the fluid flow and stress equilibrium equations, as the available analytical solutions have been derived only for simple geometrical

setups. In the following sections, we present the equations governing fluid flow (section 3.3.1) and stress equilibrium (section 3.3.2) and review relevant studies from the literature. Popular fracture propagation criteria are then reviewed in 3.3.3. The model constructed in this study will then be introduced in section §3.4.

3.3.1 Fluid Flow through the Hydraulic Fracture

It is customary in the hydrofracture literature to use the Reynolds lubrication approximation (Reynolds, 1886) to describe fluid flow through the hydraulic fracture. Figure 3.1 shows the fluid setup in the lubrication approximation.

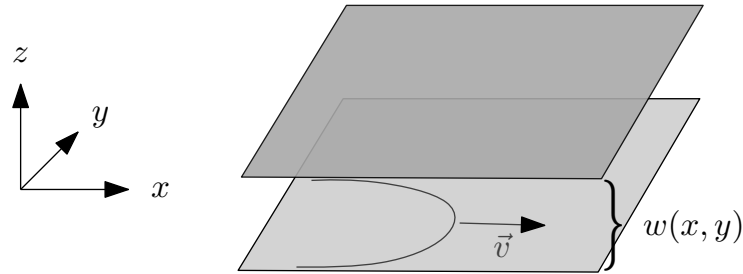


Figure 3.1: Fluid setup in the Reynolds lubrication approximation (from Marder et al., 2015). The figure shows a short segment along fracture length. It is customary in numerical models to discretize fracture length into a number of relatively short, discrete segments. According to the lubrication approximation, the walls in each segment can be taken as parallel planes which are one fracture width $w(x, y)$ apart. Fluid velocity profile is taken to be parabolic and fluid flow is assumed to be laminar and incompressible. Fluid pressure in each fracture segment is taken to be uniform.

If a pressure gradient $\vec{\nabla}P(x, y)$ is applied across the segment, fluid

velocity v is given by (Marder et al., 2015)

$$\vec{v} \approx \vec{u}f(z) + \hat{z}v_z = \vec{u}\frac{z}{w}\left(1 - \frac{z}{w}\right) + \hat{z}v_z, \quad (3.1)$$

where

$$\vec{u}(x, y) = -\frac{w^2}{2\mu}\vec{\nabla}P. \quad (3.2)$$

Because the fluid is assumed to be incompressible,

$$\frac{\partial w}{\partial t} = v_z. \quad (3.3)$$

Solving for v_z then gives the standard lubrication approximation (presented as it appears in Marder et al., 2015):

$$\frac{\partial w}{\partial t} = \vec{\nabla} \cdot \frac{w^3}{12\mu}\vec{\nabla}P. \quad (3.4)$$

Present day numerical hydrofracture models solve equation (3.4) using a numerical scheme.

This dissertation employs the lubrication approximation to model fluid flow through hydraulic fractures. The fracture geometry used in the present research is, however, different from the setup of Figure 3.1 and the associated lubrication equation turns out to be slightly different from equation (3.4). Details of the fracture geometry used in the present research, as well as the derivation of the corresponding lubrication equation, will be presented in section §3.4.

The lubrication approximation does not contain any information about the relationship between fracture width $w(x, y)$ and fluid pressure $P(x, y)$:

if the pressure gradient $\vec{\nabla}P$ is known, the lubrication approximation then provides the means to predict how the fracture width will change in time. The functional dependence of fracture width $w(x, y)$ on fluid pressure $P(x, y)$ is established by stress equilibrium in the fracture medium, and is the subject of the following section.

3.3.2 Stress Equilibrium

Consider a body Ω bounded by a curve Γ , and let a subset Γ_u of the boundary be subject to a prescribed constant displacement u_0 ; another subset, Γ_t , to constant prescribed traction, t_0 . The resulting stress distribution inside the body is the solution to an initial boundary value problem known as the static equilibrium problem, the strong form of which is described by the following equations:

$$\sigma_{ij,j} + b_{ij} = 0, \text{ in } \Omega, \quad (3.5)$$

$$u = u_0, \text{ on } \Gamma_u, \quad (3.6)$$

$$\sigma \cdot n = t_0, \text{ on } \Gamma_t, \quad (3.7)$$

where σ is the Cauchy stress tensor, b is the body force per unit volume and n is the outward unit normal vector. In the case of fluid-driven fracture, the fracture walls are traction free, and the component of traction normal to the fracture walls is the fluid pressure.

Most hydrofracture models assume shale to be linear elastic, in which

case the constitutive equation relating the stress and strain is the Hooke's law,

$$\sigma_{ij} = C_{ijkl}\epsilon_{kl}, \quad (3.8)$$

where C is the elasticity tensor. It is also customary in the hydrofracture modeling literature to take shale to be isotropic.

3.3.3 Fracture Propagation

A variety of fracture propagation models exist in the hydrofracture literature. Every numerical model of fracture propagation is constructed of three essential components: a crack propagation criterion; prediction of the propagation direction, and computation of the propagation velocity (to determine how far the fracture should extend in the next time-step).

The objective in this section is to introduce fracture propagation models by presenting a review of two such models from the literature. Each model consists of a propagation criterion and a method to determine the propagation direction. The maximum circumferential stress and the maximum energy release rate are the models which appear in this review. The propagation model employed in this dissertation will be discussed separately and in more detail in section 3.4.3.3.

3.3.3.1 Maximum Circumferential Stress

A popular fracture propagation criterion in the hydrofracture literature is the maximum circumferential stress criterion (Olson, 1990, 2007; Wu and Olson, 2015). First proposed by Erdogan and Sih (1963), this criterion is

based on the assumption that the fracture will grow from its tip in a direction perpendicular to the maximum circumferential stress: propagation is assumed to be always in opening mode, i.e, along the direction in which the circumferential stress is zero. This assumption leads to the following prediction for the direction of propagation, θ :

$$\tan \frac{\theta}{2} = \frac{1}{4} \frac{K_I}{K_{II}} \pm \frac{1}{4} \sqrt{\left(\frac{K_I}{K_{II}}\right)^2 + 8}. \quad (3.9)$$

The propagation direction θ is measured from the crack alignment, and K_I and K_{II} are respectively mode I (opening) and II (shearing) stress intensity factors. According to this criterion, the crack propagates only when

$$K_I = K_{IC}, \quad (3.10)$$

where K_{IC} is a material constant known as the *fracture toughness*. Hydrofracture models which employ this criterion employ a numerical scheme such as the displacement discontinuity method to determine K_I and K_{II} (Olson, 1990, 2007).

3.3.3.2 Maximum Energy Release Rate

The maximum energy release rate criterion (Nuismer, 1975) is another fracture propagation criterion used in hydrofracture models (Dahi-Taleghani and Olson, 2011). According to this criterion, a given fracture will propagate critically only if the strain energy release rate G , defined by Irwin (1957) as

$$G = \frac{K_I + K_{II}}{E} \frac{1}{1 - \nu^2}, \quad (3.11)$$

exceeds a material property known as the *critical strain energy release rate*, G_c . As G combines the mode I and II stress intensity factors, the maximum energy release rate criterion can model mixed mode I and II propagation.

Propagation direction in the criterion is determined in the following way: consider a hypothetical kink at the tip of a given fracture, at an angle θ to the current fracture alignment. If the fracture abruptly changed its path and propagated in the direction of the kink, then the stress intensity factors K_I and K_{II} and consequently the strain energy release rate G would be different from their current value, and will be in general a function of the kink angle θ . The propagation direction in the criterion is taken to be the direction in which the strain energy release rate is maximum.

For quasi-static cracks, the criteria presented here are nearly identical, but this is not the case for dynamic cracks. We note that fracture mechanics has not yet settled which of these criteria is correct, or preferable.

3.3.4 Analytical Models

The literature on fluid-driven fracture started in the 1950s. Early papers on the subject employed geometrical setups that were simple enough to lend themselves to analytical progress: all early papers describe a single fracture in an infinite medium. Nevertheless, besides the remarkable amount of insights gained from such simple models, prior to the development of numerical hydrofracture models in the 1960-1970s, hydraulic fracture design and analysis relied significantly on the analytical results of early papers, for instance

to estimate the injected volume needed to widen the fracture enough to allow the proppant to enter the fracture (Adachi et al., 2007).

This section presents a review of relevant analytical models from the literature. In historical order, the penny-shaped fracture and the KGD model are reviewed first. The model presented afterward is the PKN model with the addition of new results due to Marder et al. (2015). This final model is the theoretical framework for the numerical hydrofracture model of this dissertation and is accordingly discussed in more detail.

3.3.4.1 Penny-Shaped Fracture

Historically, the penny-shaped fracture precedes all other geometrical setups. Also known as the radial fracture, the penny-shaped fracture occupies a circle in the plane $z = \text{const}$, Figure 3.2.

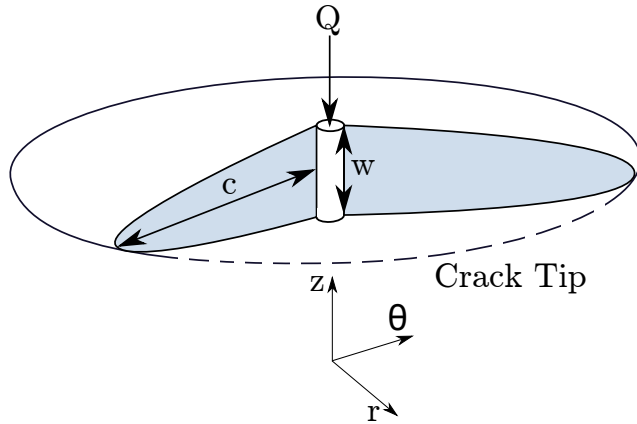


Figure 3.2: The penny-shaped (radial) geometry. Fluid is injected into the wellbore at the center.

The penny-shaped fracture was first studied by Sneddon in 1946. Building on the works of Griffith (1921) and Westergaard (1939), Sneddon (1946) analytically obtained, among other results, the stress distribution around a penny-shaped fracture in an infinite linear elastic medium. The particular result we review here is one which later proved essential in the development of the classical analytical models of hydrofracture, namely the KGD model and the PKN model.

The result is the following: for a penny-shaped fracture in an infinite medium, Sneddon has shown that if the walls of the fracture are subjected to constant internal pressure P and far-field stress σ_{\perp} , then the fracture will be elliptical and the displacement w in the center of the crack ($r = 0$) will be given by

$$w = \frac{4c(1 - \nu^2)}{\pi Y}(P - \sigma_{\perp}) = \beta P_{\text{net}}, \quad (3.12)$$

where c is the fracture radius, ν is Poisson's ratio, Y is Young's modulus, P is assumed to be constant over $r \leq c$ and the net pressure P_{net} is defined as $P - \sigma_{\perp}$.

In the PKN or KGD model, the coefficient β is defined using the short dimension of the crack. The models are discussed in more detail in the following subsections.

3.3.4.2 The KGD Model

The Khristianovic-Geertsma-DeKlerk (KGD) model is due to Khristianovic and Zheltov (1955) and Geertsma and de Klerk (1969). As shown in Figure 3.3, the KGD model assumes fracture height H to be uniform along the fracture length L ; fracture width w is taken to be uniform along H . Fluid is injected through the rectangular cross section of the KGD crack (the $y - z$ plane) and propagation happens in the x direction. In the KGD model, only the fracture length L and width w are allowed to change during injection; fracture height H is taken to be constant in time.

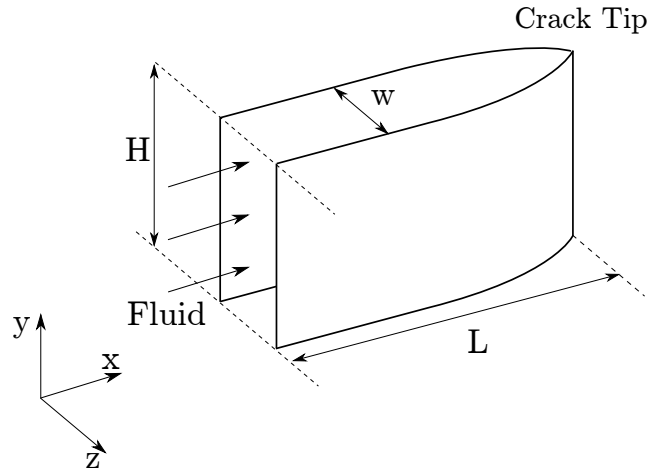


Figure 3.3: Geometry of the KGD fracture. Water flows into the rectangular cross section of the fracture, causing growth in the x direction. Fracture height H is uniform along the crack length L ; the fracture is uniform in the y direction.

At any given time t and location x along the crack length, crack width

and net fluid pressure are related through Sneddon's result, equation (3.12):

$$w(x, t) = \beta P_{\text{net}}(x, t),$$

where for the KGD geometry

$$\beta = \frac{2L(t)(1 - \nu^2)}{Y}. \quad (3.13)$$

The KGD results we now review here are the scaling laws for net fluid pressure and crack length. For the reader's convenience, the results are presented in the simplified form in which they appear in Chen (2014).

For a constant injection rate Q , when the length of the KGD crack reaches $L(t)$, net pressure profile along the crack length is given by

$$P_{\text{net}}(x, t) = \left\{ \frac{48Q\mu[L(t) - x]}{H\beta^3} \right\}^{\frac{1}{4}}. \quad (3.14)$$

Time evolution of crack length is given by

$$L(t) = C_1 \left(\frac{Q}{H} \right)^{\frac{1}{2}} t^{\frac{2}{3}}, \quad (3.15)$$

where

$$C_1 = \left(\frac{5}{8} \right)^{\frac{2}{3}} \left[\frac{Y}{6(1 - \nu^2)\mu} \right]^{\frac{1}{6}}.$$

3.3.4.3 The PKN Model

Perhaps the most famous of the early hydrofracture studies is the article due to Perkins and Kern (1961). In this work, hydraulic fracture is taken to

be of elliptical cross section and uniform height, Figure 3.4. The fracture is imagined to extend as a result of fluid flowing into the cross section.

Perkins and Kern derived analytical estimates of the width of hydraulic fractures in rock formations in the following cases: horizontal/vertical fractures, Newtonian/non-Newtonian fracturing fluid, and laminar or turbulent regimes for an elliptical cross section. In recent numerical studies, the assumption of an elliptical cross section or uniform height can be relaxed in favor of more realistic fracture geometries and the fluid flow through the fracture is typically taken to be laminar.

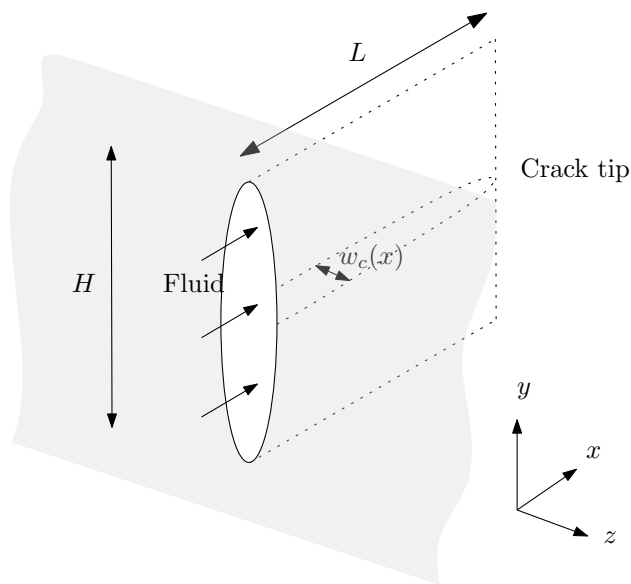


Figure 3.4: The geometry of the Perkins and Kern fracture (figure from Marder et al., 2015).

Nordgren (1972) later extended the work of Perkins and Kern to include the possibility of fluid loss to the formation or *leak-off*, so the model is presently

known as the Perkins–Kern–Nordgren or the PKN model. We have adopted in this chapter Marder et al.’s (2015) simplified presentation of the original Perkins and Kern expressions. The PKN results reviewed here are used later in this dissertation to validate our numerical model.

To employ the lubrication approximation of equation (3.4) in the context of the PKN geometry, Marder et al. (2015) employ four assumptions:

1. At any given location x along the crack length, fluid pressure is assumed to have reached equilibrium over the elliptical cross section, i.e., $P = P(x)$;
2. The lubrication approximation of equation (3.4) is applied to the minor axis of the elliptical cross section of the crack: $w = w_c$ (see Figure 3.4);
3. The cross section is assumed to remain elliptical as the crack grows, and
4. The injection rate of water Q into the fracture is assumed to be constant.

For the PKN crack, Sneddon’s result (equation (3.12)) takes on the following form:

$$w_c(x) = \beta(P - \sigma_{\perp}) = \beta P_{\text{net}},$$

where σ_{\perp} is the far-field stress perpendicular to the crack and

$$\beta = \frac{2H(1 - \nu^2)}{Y}, \tag{3.16}$$

where $H \ll L$ is the short dimension of the crack.

Inserting equation (3.16) into equation (3.4) and integrating for pressure yields the scaling law for net pressure along the crack length:

$$P_{\text{net}}(x, t) = 4 \left\{ \frac{Q\mu [L(t) - x]}{\pi H \beta^3} \right\}^{\frac{1}{4}}. \quad (3.17)$$

Crack length $L(t)$ is given by

$$L(t) = \left[\frac{5^4 Q^4 Y}{8^3 \pi^3 \mu (1 - \nu^2) H^4 Q} \right]^{\frac{1}{5}} t^{\frac{4}{5}}. \quad (3.18)$$

Net pressure at the base of crack is given by

$$P_{\text{net}}(x = 0) = \left(\frac{\mu Q^2 Y^4}{H^6} \right)^{\frac{1}{5}} t^{\frac{1}{5}}. \quad (3.19)$$

As first described by Griffith (1921), a given crack inside a medium starts to propagate in an unstable fashion only if the energy supplied to the crack tip exceeds the energy required to create new surface area in the medium. In the case of hydraulic fracture, adopting the Griffith's energy balance approach results in the following propagation criterion: a given hydraulic fracture will propagate if the mechanical work done by the fracturing fluid on the fracture walls exceeds the sum of the energy required to create new surfaces in the medium and overcome the viscous frictional loss associated with the fluid flow through the fracture and to the tip.

Marder et al. (2015) analytically determined the terms in the energy balance approach and obtained the condition under which a given dynamic PKN crack will continue to propagate:

$$\frac{\beta}{3} P_{\text{net}}^2(x = 0) > \Gamma, \quad (3.20)$$

where Γ is the specific fracture energy of the rock in $\frac{\text{J}}{\text{m}^2}$.

3.3.5 Numerical Models

The analytical models reviewed in the previous section provide insight into hydraulic fracture modeling and are appropriate for a single fracture of a simple geometry. Simulation of more realistic or complex geometrical setups, however, requires the use of numerical models. The importance of numerical hydrofracture models which can simulate many fractures becomes more pronounced when one considers that the interaction between two or more hydraulic fractures can have a significant effect on production, an effect which is typically absent from simple analytical models.

At present, solution of the stress equilibrium equation is typically attempted using either a version of the finite element method (Dahi-Taleghani and Olson, 2011; Haddad and Sepehrnoori, 2014 and 2016) or the displacement discontinuity method (Wu & Olson, 2015; Olson, 2004). The finite element approach was pioneered by Clifton (1978); the displacement discontinuity method is due to Crouch (1976).

In 2015, Wu and Olson proposed the *simplified three-dimensional displacement discontinuity method* and reported a 1000 fold increase in computational efficiency compared to the standard displacement discontinuity method. The method was used to construct a three-dimensional model of hydrofracture propagation in naturally fractured reservoirs.

Chen (2014) and Marder et al. (2015) constructed a pseudo–three–dimensional lattice model of hydraulic fracture. In this model, the rock is viewed as a three–dimensional array of cubic mass blocks connected with Hookean springs, and fracture corresponds to the breaking of the spring between two adjacent mass blocks. Lubrication approximation was used to model the fluid flow through the fractures.

The fracture propagation criterion in this model is based on the extension of the springs: a given spring breaks when the extension of the spring exceeds a critical value δ , the *extension at failure*, derived analytically so as to reproduce the Young’s modulus and the specific fracture energy of the rock. For a lattice made up of blocks of side a , the extension at failure was shown to be

$$\delta = \sqrt{\frac{2\Gamma a}{Y}}, \quad (3.21)$$

where Γ is the specific fracture energy and Y is the Young’s modulus of the rock.

The model was shown to reproduce the PKN equations for a single crack. Fluid motion, elastic deformation and crack propagation all came out of the lattice model based on the underlying physics.

Despite the tremendous progress of the hydrofracture modeling literature, computational efficiency still remains a major issue. This problem becomes more pronounced if one chooses to consider the interaction between hydraulic fractures and pre–existing natural fractures in the reservoir.

The numerical hydrofracture model developed in this dissertation is presented in the next section. We note here that the ability to efficiently explore geometric and temporal complexities of fracture networks comes at the cost of accuracy at the level of fracture mechanics. Given that the primary design objective of our model is to simulate the interaction of hydraulic fractures with a large number of natural fractures in a computationally efficient manner, we are forced to treat the mechanics of fracture in less detail than typical numerical hydrofracture models. Details of fracture mechanics in the model will be presented in section 3.4.3.

3.4 The Model

We showed in Chapter 2 that the natural fracture/incipient crack system in shales can form a connected network, which we referred to as the spanning cluster, and suggested that gas production from hydraulically fractured shales comes from that subset of the spanning cluster which is opened during the treatment by the fracturing fluid inside the hydraulic fractures.

This section presents our numerical hydrofracture model. Before we present the numerical framework, we first introduce the setup of the model and a qualitative description of the scenarios the model can simulate.

3.4.1 Setup

The initial configuration of the model consists of the spanning cluster and a perforation crack which intersects the spanning cluster, and corresponds

to the beginning of the injection. Figure 3.5 shows the initial configuration.

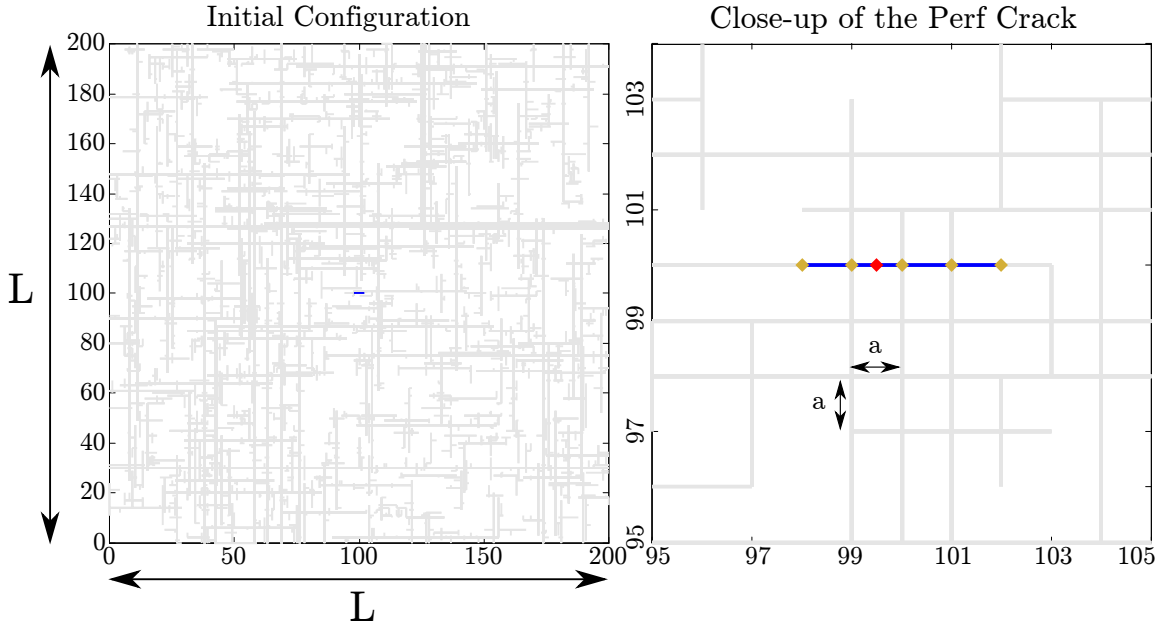


Figure 3.5: Map view of the initial configuration of an example hydrofracture simulation (left) and close-up of the perforation crack (right). The gray lines represent the spanning cluster, determined from the percolation model of Chapter 2. The blue line corresponds to the perforation crack. Water is injected inside the perforation crack at the segment marked by the red diamond. Depending on the injection rate and duration, eventually at some point after the beginning of injection new fractures may start from the intersections of the perforation crack with the spanning cluster (the gold diamonds). In our model, water is allowed to propagate only along the spanning cluster cracks and not through the shale, so the gray lines specify the potential paths of hydraulic fractures in advance of the simulation.

The setup of the model is identical to that of the model in Chapter 2: fractures are restricted to the bonds of a square lattice of spacing a and size L , and each $a \times a$ square tile inside the lattice represents a block of mass. Each fracture consists of a number of *channel segments* of length a .

The perforation crack includes an injection segment, which allows the model to add water to the system from the outside. Besides the injector, water has no other way of getting in or out of the fracture assembly; the extremely low permeability of shales makes it reasonable to assume that water leak-off to the formation is negligible.

Since PKN geometry is assumed for the fractures, the width profile in the $y - z$ plane is elliptical (Figure 3.4). Our hydrofracture model employs fluid flow and stress response expressions which account for the variation in fracture width in the z direction (direction of fracture height), and as such the model is pseudo-three-dimensional.

Once injection has started, as time goes by fluid pressure inside the perforation crack builds up. Depending on the injection rate and duration, the pressure may eventually rise enough to start a new fracture, which will either propagate along one of the natural fractures which intersect the perforation crack, or break new rock in what we refer to as *incipient cracks*: streaks of relative mechanical weakness which were not open prior to the treatment, but which opened up later during the injection and as a result of the change in the state of stress. The union of natural fractures and incipient cracks characterizes all possible propagation pathways for the hydraulic fractures. In the hydrofracture model, the set of natural fractures and incipient cracks is taken to be the spanning cluster of the percolation model of Chapter 2 and as such fracture propagation paths are specified in advance of the simulation.

Once a new crack has initiated, the crack might propagate until it has

reached the end of the natural fracture/incipient crack along which it has been propagating, at which point the model stops the crack. Another possibility is that the crack may reach an intersection with a natural fracture/incipient crack of the spanning cluster, at which point water may turn into the intersection and/or continue propagation.

The fluid path inside the spanning cluster and at the end of the injection is the fracture network responsible for shale gas production. Our objective here is to model the path. Going back to the motivations for this dissertation, the primary purpose of our hydrofracture model has to be to allow a robust investigation of how the fracture network geometry affects production. In particular, we are interested in identifying the characteristic length scales involved in production from the network, as well as the scaling of gas production, both of which were first suggested by Patzek et al. (2013, 2014). We note that our hydrofracture model therefore has to be able to simulate the development of a large fracture network, i.e. a large number of hydraulic fractures, natural fracture/incipient cracks and their interactions. From this design philosophy it immediately follows that any computationally expensive hydrofracture model will not fit the purpose of this research.

Here we adopt an approach to hydrofracture modeling which can be described as being at an “intermediate” level of including details, in that we model the fluid flow numerically and rely on analytical estimates, instead of numerical methods, to simulate the stress response. Before introducing the details of the model in the following sections, to help the reader make a

judgment as to the cost/benefit of the approach, we now address the accuracy of the hydrofracture model and present a comparison of the model to more detailed hydrofracture simulations.

As far as accuracy, we show in section §3.5 that the hydrofracture model reproduces established analytical results for a single fracture (the PKN solution) with reasonable accuracy. We suggest that the difference between simulation and theory for a single fracture, presented in Figure 3.10 and Figure 3.11, is indicative of the magnitude of error associated with simulations of fracture networks done with the hydrofracture model.

Two features of more elaborate hydrofracture simulations are absent from our hydrofracture model. First, the interaction between nearby hydraulic fractures, the *stress shadow effect* (Wu and Olson, 2013; Geilikman and Wong, 2013), does not emerge naturally from the underlying assumptions of the hydrofracture model: we assume hydraulic fractures to be isolated. It is, however, possible to extend the model to allow the possibility of the stress shadow effect, and more details are provided in section 3.4.3.1 and section §3.6. Second, propagation in the hydrofracture model is restricted to paths which are specified in advance of simulation. To relax this restriction requires stress computations which can be used in a fracture propagation criterion to decide fracture path. However, addition of such computations to the hydrofracture model will introduce a significant computational load which will strip the model of its ability to simulate the time evolution of a large fracture network in a computationally efficient manner.

We now move on to the details of the hydrofracture model and discuss in the next two sections fluid flow through the fractures (section 3.4.2) and fracture mechanics (section 3.4.3).

3.4.2 The Lubrication Approximation

We use the lubrication approximation in this work to model fluid flow through hydraulic fractures. In particular, the lubrication approximation provides us with the means to update the width of channel segments in time.

As mentioned earlier, the lubrication approximation of equation (3.4) describes fluid flow between two parallel plates. The fractures in our model, however, are PKN fractures: not of a rectangular cross section, as is the case for parallel plates, but of an elliptical cross section, for which the lubrication approximation takes on a form which is slightly different from that of equation (3.4) (Perkins and Kern, 1961):

$$\frac{\partial w}{\partial t} = \vec{\nabla} \cdot \frac{w^3}{16\mu} \vec{\nabla} P, \quad (3.22)$$

in which the factor of 16 has replaced the 12 in equation (3.4).

We now present the derivation of the lubrication equation for PKN fractures. The derivation is presented as it appears in Marder et al. (2015).

Consider a fluid flowing through a channel of an elliptical cross section. Then the total volumetric flow rate through the crack at any point x along the crack length is given by

$$Q = \int u_x(x, y) w(x, y) dy, \quad (3.23)$$

where u_x is the x component of the fluid velocity vector \vec{u} , given by equation (3.2). For an elliptical cross section of minor axis w_c (crack width) and major axis H (crack height), Q comes out to

$$Q = -\frac{\pi \left(\frac{w_c}{2}\right) \left(\frac{H}{2}\right)}{4\mu} \frac{\partial P}{\partial x}. \quad (3.24)$$

We now discretize fractures along the length and into channel segments of length a . Each segment is represented in the model by a bond on the square lattice and can have up to 6 neighbors. The cross section of each segment is elliptical and of major axis H , but the minor axis is smaller for segments which are closer to the tip. Taking w_i to represent the minor axis of segment i , the total volume of fluid V contained in the fracture assembly is

$$V = \sum_i \pi \left(\frac{H}{2}\right) \left(\frac{w_i}{2}\right) a. \quad (3.25)$$

Let index j denote the neighbors of segment i . Discretizing equation (3.24) then gives

$$Q = \pi \left(\frac{w_{>}}{2}\right)^3 \frac{H}{2} \frac{1}{4\mu} \frac{p_j - p_i}{a}, \quad (3.26)$$

where

$$w_{>} = w_i, \quad \text{if } p_i > p_j; \text{ else } w_j. \quad (3.27)$$

The rate of change of width due to the volumetric flow rate Q entering the segment can be found from the rate of change of volume:

$$\pi \left(\frac{H}{2}\right) \frac{1}{2} \frac{dw}{dt} a = Q. \quad (3.28)$$

Setting equal equations 3.26 and 3.28 gives the following relationship between the change in segment width and the net flux of water through:

$$\pi \left(\frac{H}{2} \right) \frac{1}{2} \frac{dw}{dt} a = \pi \left(\frac{w_{>}}{2} \right)^3 \frac{H}{2} \frac{1}{4\mu} \frac{p_j - p_i}{a}, \quad (3.29)$$

$$\frac{dw}{dt} = \frac{1}{a} \sum_j v_{ij} w_{>}, \quad (3.30)$$

where

$$v_{ij} = \frac{w_{>}^2}{16\mu} \frac{p_j - p_i}{a} \quad (3.31)$$

is the volumetric flux of water entering segment i from neighboring segment j . Depending on the relative magnitude of p_i and p_j , v_{ij} can be negative or positive. The antisymmetry of equation (3.31), however, guarantees that if no water enters or leaves the fracture assembly, then the volume of water inside the system will remain constant in time.

In this dissertation, we employ the forward Euler finite difference formulation of equation (3.30):

$$\frac{w_i^{n+1} - w_i^n}{\Delta t} = \frac{1}{a} \frac{w_{>}^3}{16\mu} \sum_j \frac{p_j^n - p_i^n}{a}, \quad (3.32)$$

where the superscripts n and $n + 1$ mark respectively the value at the present time step t_n and the next time step t_{n+1} ; Δt is constant and given by

$$\Delta t = t_{n+1} - t_n, \quad (3.33)$$

and

$$w_{>} = w_i^n, \quad \text{if } p_i^n > p_j^n; \text{ else } w_j^n. \quad (3.34)$$

Equation 3.32 describes the change in segment width due to water transfer between the segment and its neighbors.

As mentioned earlier, water is added to the fracture assembly at a constant injection rate Q . Injection takes place at one of the segments of the perforation crack, one which we refer to as the *injection segment* or the *injector*. It should be noted that equation (3.32) describes non-injector segments only: besides water transfer between the injector and its neighbors, the change in the width of the injector also includes the contribution of the injected water, given by equation (3.28). Superposing equation (3.32) and equation (3.28) then gives the following expression for the change in the width of the injector:

$$\frac{w_i^{n+1} - w_i^n}{\Delta t} = \frac{4Q}{\pi a H} + \frac{1}{a} \frac{w_i^3}{16\mu} \sum_j \frac{p_j^n - p_i^n}{a}. \quad (3.35)$$

3.4.3 Fracture Mechanics

So far we have described the initial configuration of the model and presented the lubrication approximation as a means to update the width of the segments in time. We now proceed to present the fracture mechanics rules of the model. These rules govern initiation and propagation of the hydraulic fractures, as well as their interaction with natural fracture/induced cracks of the spanning cluster.

3.4.3.1 Pressure

Given pressure and width of the segments at time t_n , the lubrication approximation of equation (3.32) makes it possible to predict the widths at

time $t_n + \Delta t$. To use equation (3.32), one needs to also compute pressure. We use Sneddon's expression, modified for the PKN geometry, to compute the pressure at segment i :

$$p_i = \frac{w_i}{\beta} + \sigma_{\perp}, \quad (3.36)$$

where σ_{\perp} is the far-field stress perpendicular to segment i and

$$\beta = \frac{2d(1 - \nu^2)}{Y}, \quad (3.37)$$

in which d is the short dimension of the crack and is given by

$$d = \frac{1}{\frac{1}{H} + \frac{1}{L}}. \quad (3.38)$$

We mentioned earlier that the coefficient β for the PKN geometry is defined using the short dimension of the crack. As a given PKN crack grows, the short dimension of the crack changes from crack length L at $L \ll H$ to crack height H at $L \gg H$. Using equation (3.38) to compute the short dimension d makes it possible to account for the change in crack geometry in a continuous fashion as the crack gets longer: if $L \ll H$, then $d \approx L$, and if $H \ll L$, then $d \approx H$.

The far-field stress σ_{\perp} depends on the orientation of the segment, Figure 3.6.

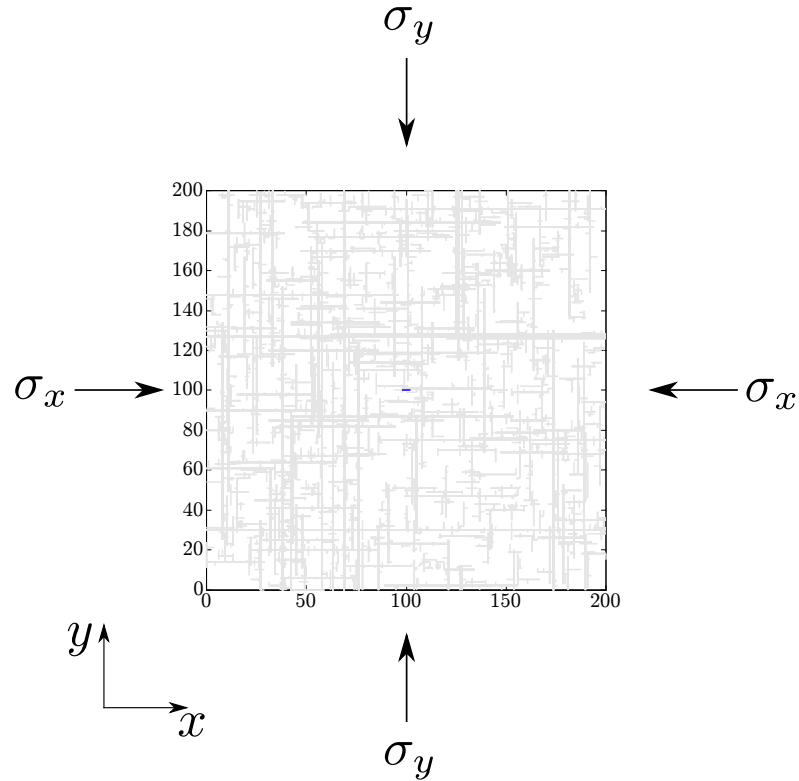


Figure 3.6: Map view of the (horizontal) far-field principal stresses in an example hydrofracture simulation. The far-field stress perpendicular to each segment, σ_{\perp} , depends on the orientation of the segment; $\sigma_{\perp} = \sigma_y$ for segments in the x direction and $\sigma_{\perp} = \sigma_x$ for segments in the y direction.

Using Sneddon’s expression to estimate pressure allows us to skip a direct solution of the stress equilibrium equation, which is one of the major sources of run-time in hydraulic fracture models. We also note that this treatment of the stress response can not model how propagation of one hydraulic fracture affects other nearby hydraulic fractures (also known as the stress shadow effect). A more detailed review of this feature and the stress shadow effect will be given in section §3.6, where the qualitative features of

the model are discussed.

3.4.3.2 Hydrofracture Initiation

The initial configuration of the model (Figure 3.5) was described earlier in this chapter to consist of the spanning cluster, and a perforation crack which intersects the cluster. Once injection has started, pressure inside the perforation crack will gradually increase and eventually start a hydraulic fracture from the perforation crack. It was suggested earlier that the new hydraulic fracture will be restricted to propagate from one of the intersections of the perforation crack with the spanning cluster; the natural fracture/induced crack along which the new hydraulic fracture propagates will be the propagation path.

We now consider one of the intersections of the perforation crack with the spanning cluster. To decide whether a new hydraulic fracture will start from the intersection, the model considers a seed crack in the direction of each wing of the natural fracture/induced crack which intersects the perforation crack, Figure 3.7.

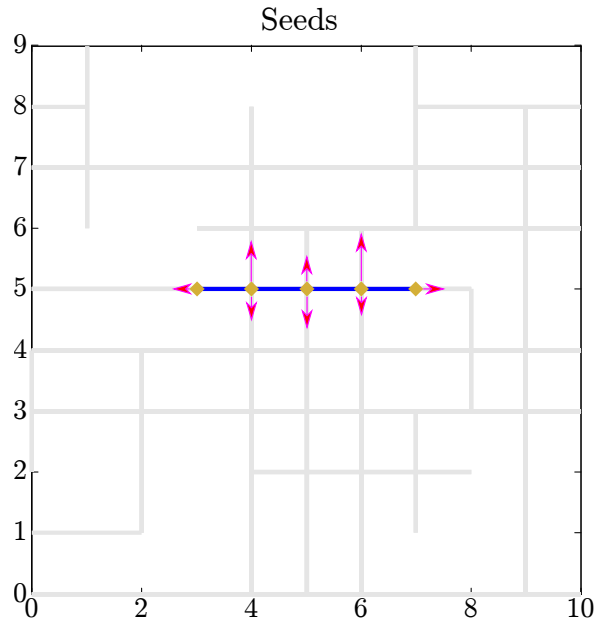


Figure 3.7: The purple arrows show the seed cracks considered at the intersections of the perforation crack with the spanning cluster (the gold diamonds). Seed length is chosen from a Gaussian distribution. Hydrofracture initiation in the model is treated as the extension of a static seed crack located at an intersection.

The seed cracks in the model should be understood as approximations of material flaws: in reality, flaws of irregular shape and random size are present in all materials. The seed cracks in our model are, for simplicity, PKN edge cracks of height H and length $L \ll H$. Seed length in the model is taken to be given by a Gaussian distribution.

Because seed cracks are static, fluid pressure inside is constant. For PKN edge cracks, the critical pressure at which the crack begins to propagate

is given by

$$p_c^{\text{static}} = \sqrt{\frac{Y\Gamma}{2L(1-\nu^2)}} + \sigma_{\perp}, \quad (3.39)$$

where Y and Γ represent respectively the Young's modulus and specific fracture energy of the cement/weak shale which hosts the seed crack, and σ_{\perp} is the far-field stress perpendicular to the crack.

The model employs equation (3.39) to determine the critical extension pressure for static seed cracks. The Poisson's ratio ν is assumed to be the same for all fractures and equal to 0.25. Y and Γ of different natural fractures/induced cracks are assumed in the model to be given by Gaussian distributions. This choice is an attempt at capturing at least part of the heterogeneity in mechanical properties of shales. (It should be noted that a canonical model of reservoir heterogeneity has not been established in the literature yet.)

The model treats hydrofracture extension in a discrete fashion, that is, fractures grow one new segment at a time. This means that the minimum incremental growth, from one time step to the next, is one lattice spacing (1 m in our model). Width of newly formed segments in the model is taken to be given by Marder et al.'s (2015) extension at failure:

$$\delta = \sqrt{\frac{2\Gamma a}{Y}},$$

where a is the lattice spacing. The water which fills the new segment comes from exactly one *parent* segment, located immediately upstream of the new

segment. To ensure conservation of mass, in the time step when the new segment forms, the model reduces the width of the parent segment by δ . Assuming typical shale values (Gale and Holder, 2008; Marder et al., 2015), $Y = 30$ GPa, $\Gamma = 100 \frac{\text{J}}{\text{m}^2}$ and δ comes out to $80 \mu\text{m}$ for a lattice of spacing $a = 1$ m.

If one decides initiation solely based on equation (3.39), then as soon as pressure at a given seed exceeds p_c^{static} , a segment of a length equal to one lattice spacing (1 m in our model) and a width equal to δ will form. Suppose that this is the case, and assume the new segment forms at time t_{n+1} . Let σ_{parent} and σ_{new} represent the far-field stress perpendicular to the parent segment and the new segment, respectively. Then to ensure that pressure in the new segment (downstream) is less than that in the parent segment (upstream), one should make sure that

$$p_{\text{parent}}^{n+1} \geq p_{\text{new}}^{n+1}, \quad (3.40)$$

$$\begin{aligned} \Rightarrow \frac{w_{\text{parent}}^n - \delta}{\beta_{\text{parent}}} + \sigma_{\text{parent}} &\geq \frac{\delta}{\beta_{\text{new}}} + \sigma_{\text{new}}, \\ \Rightarrow p_{\text{parent}}^n &\geq \frac{\delta}{\beta_{\text{new}}} + \frac{\delta}{\beta_{\text{parent}}} + \sigma_{\text{new}} = p_{\delta}, \end{aligned} \quad (3.41)$$

or equivalently, expressed in terms of width,

$$\begin{aligned} w_{\text{parent}}^n - \delta &\geq \frac{\beta_{\text{parent}}}{\beta_{\text{new}}} \delta + \beta_{\text{parent}} (\sigma_{\text{new}} - \sigma_{\text{parent}}), \\ \Rightarrow w_{\text{parent}}^n &\geq \left(\frac{\beta_{\text{parent}}}{\beta_{\text{new}}} + 1 \right) \delta + \beta_{\text{parent}} (\sigma_{\text{new}} - \sigma_{\text{parent}}). \end{aligned} \quad (3.42)$$

Note that equation (3.41) imposes a new condition, besides equation (3.39), on initiation: no new segment should form unless pressure in the (future) parent segment is large enough that when a new segment of length a and

width δ forms, pressure in the new segment, which is always downstream of the parent segment, will necessarily be less than or equal to the pressure inside the parent segment. This condition represents the physics of flow, and also has important implications for the stability of the numerical solution. If pressure downstream gets larger than pressure upstream, fluid starts to oscillate back and forth between the upstream and the downstream, typically resulting in the instability of the numerical scheme.

Taking into account both equation (3.39) and equation (3.41), the initiation criterion in the model is then taken to be the following: a new segment will grow from a seed crack at a given intersection only if pressure p at the seed crack satisfies

$$p \geq \max(p_c^{\text{static}}, p_\delta), \quad (3.43)$$

where p_c^{static} is given by equation (3.39); p_δ , by equation (3.41).

In the time step when a new hydraulic fracture initiates, the model considers exactly one new channel segment at the location of the seed and removes the seed from the system. The new segment is one of the bonds which make up the spanning cluster.

As shown in Figure 3.7, the path of a new hydraulic fracture may intersect multiple other natural fractures/induced cracks of the spanning cluster. As long as fluid pressure is large enough to overcome viscous frictional losses along the length of the hydraulic fracture and overcome surface energy of the cement/weak shale, the fracturing fluid will continue to open up the natural

fracture/induced crack and the hydraulic fracture will continue to propagate along the path until an intersection with another natural fracture/induced crack is reached. At this point the model considers a seed crack in each wing of the intersecting natural fracture/induced crack. When the intersecting fracture ends at the path, the number of seeds is 1; when it crosses the path, 2 seeds are considered. Then equation (3.43) is used to decide whether the fracturing fluid will divert into any of the seeds at the intersecting fracture and start to open it.

The use of seed cracks allows the model to treat both initiation and diversion of hydraulic fractures as the extension of a static crack. It is however incorrect to assume that straight propagation of dynamic cracks may also be modeled in the same way. As the next subsection will elaborate, dynamic fluid-driven fractures are unstable and as such one may not model propagation as a sequence of extension of static seed cracks at the tip.

3.4.3.3 Hydrofracture Propagation

Having discussed hydrofracture initiation and diversion, we now focus on straight propagation of hydraulic fractures. We use in the model Marder et al.'s condition for crack propagation (2015), given by equation (3.20):

$$\frac{\beta}{3} P_{\text{net}}^2 (x = 0) > \Gamma.$$

This expression was obtained by setting the work done on crack faces by the injection of the fluid to be greater than the energy cost of creating extra

surface area. The contribution of viscous dissipation here is taken into account through the pressure profile used in the work calculation. For a given dynamic PKN crack, propagation will continue only if equation (3.20) is satisfied.

Note that net pressure at crack base $P_{\text{net}}(x = 0)$ only grows as time goes by, so one can conclude from equation (3.20) that dynamic fluid-driven cracks will always have enough energy to propagate once they start. In fact, the net energy available for propagation increases as the crack grows longer and as such one might expect the crack to grow infinitely. There are, however, certain physical mechanisms which prevent infinite crack growth both along the lateral extent of the shale layer (horizontal) and across the layer height (vertical), and here we present two such mechanisms.

Initiation of a new crack at the base of a dynamic crack is one mechanism which limits the propagation of the dynamic crack. Marder et al. (2015) showed that the total viscous dissipation associated with flow through a crack of length L scales with $L^{\frac{1}{4}}$. This means that pushing the fluid through the crack and to the crack tip becomes harder as the crack grows longer. It is therefore reasonable to propose that at some point during propagation viscous dissipation through the crack becomes so large that it becomes energetically more favorable to start a new crack. Since pressure is at its largest at the base and drops towards the tip, the new crack is expected to start typically from around the base of the old crack.

The most important mechanism for containment of hydraulic fractures in the height (vertical) direction is the contrast in the in-situ stress between

the shale and the layers immediately above and below (Fisher and Warpinski, 2011). A theoretical analysis of this mechanism was provided by Simonson et al. (1978); a data-based discussion of this mechanism and other fracture height containment mechanisms can be found in Fisher and Warpinski (2011). We note that hydraulic fractures in shales are expected to grow vertically because the vertical stress (overburden) in shale reservoirs is generally the largest principal stress: shale wells are typically deeper than about 2,000 ft, at which point the overburden gets larger than the horizontal stresses and becomes the largest principal stress (Fisher and Warpinski, 2011).

As mentioned earlier, fractures in the model grow one new segment at a time and width of newly formed segments is taken to be given by Marder et al.'s (2015) extension at failure, δ (equation (3.21)). In the time step when a dynamic hydraulic fracture extends, the model considers exactly one new channel segment in front of the crack tip, which is the parent segment in this case. The new segment is taken to be one of the bonds which make up the spanning cluster; in the model, dynamic cracks stop when they reach the end of the natural fracture/induced crack on which they were propagating.

To ensure that pressure in the new segment is always smaller than or equal to the old crack tip (the parent segment), we go back to equation (3.41), which for a dynamic crack gives

$$p_{\text{tip}}^n \geq \frac{\delta}{\beta_{\text{new}}} + \frac{\delta}{\beta_{\text{tip}}} + \sigma_{\text{new}} = p_{\delta}.$$

For straight propagation

$$\beta_{\text{new}} = \beta_{\text{tip}} = \beta, \quad (3.44)$$

and therefore

$$p_{\text{tip}}^n \geq \frac{2\delta}{\beta} + \sigma_{\text{new}}. \quad (3.45)$$

We note that it is the discrete nature of the numerical model which necessitates the use of equation (3.45) beside equation (3.20). Because the model is constructed on a lattice, numerical propagation takes place in increments of one lattice spacing and the width of newly created segments is pre-specified. Propagation in the continuum theory, however, can take place in any positive increment of length and therefore equation (3.20) alone is enough to describe propagation.

The analysis presented in this section ultimately leads to the following propagation criterion: the model allows a given dynamic crack to continue to propagate only if there is enough energy available for propagation, equation (3.20), and pressure downstream remains smaller than pressure upstream, equation (3.45).

3.4.3.4 Formation of Loops

The diversion mechanism described earlier allows the fluid to turn corners as it advances through the spanning cluster. Diversion can lead to formation of loops in the hydraulic fracture network, Figure 3.8.

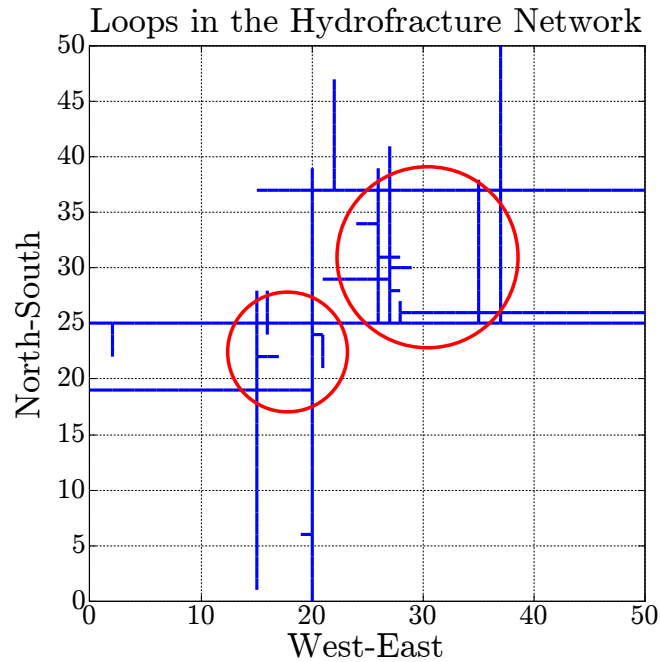


Figure 3.8: In the model, fluid can turn corners at intersections and may form loops. The red circles show two loops in the network, marked by blue lines. Loops can form due to a head-on collision of two dynamic cracks, or because a dynamic crack has reached an intersection which the fluid had visited earlier.

Regardless of how loops form, the model stops the propagation of the dynamic crack(s) which complete the loop, and ensures that new seeds are considered only at those bonds of the spanning cluster which have not been opened yet.

3.5 Validation

We now present a comparison of theory and numerical simulation to validate the model. The PKN theory is used in this dissertation to benchmark

the numerics. Since the theory can describe only a single fracture and not a complex network of fractures, the geometry of the test case considered here is one in which a single crack initiates and propagates, Figure 3.9.

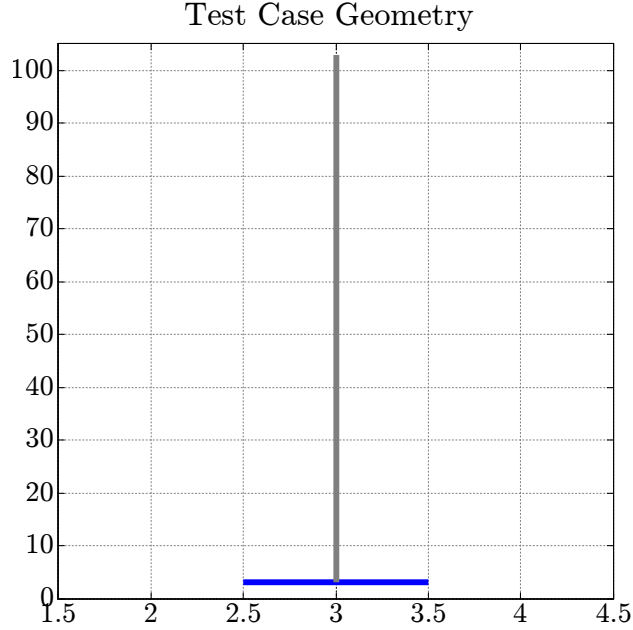


Figure 3.9: Geometry of the test case used to validate the hydrofracture model. Water is injected at the blue segment. Pressure buildup at the injector eventually starts a dynamic crack which will propagate along the natural fracture/induced crack marked by the gray line. The resulting propagation is then compared to the PKN theory.

We compare theory and simulation first for the time evolution of pressure at crack base. As presented in Figure 3.10, the numerics agree well with the analytical expression, which is given by equation (3.19):

$$P(x=0) = \left(\frac{\mu Q^2 Y^4}{H^6} \right)^{\frac{1}{5}} t^{\frac{1}{5}} + \sigma_{\perp}.$$

The far-field stress σ_{\perp} is taken to be 0 here. Time t is measured from initiation, which happens at about 0.5 s here and is marked by the pressure spike. The parameter β in the simulation was taken to be equal to $\frac{2H(1-\nu^2)}{Y}$.

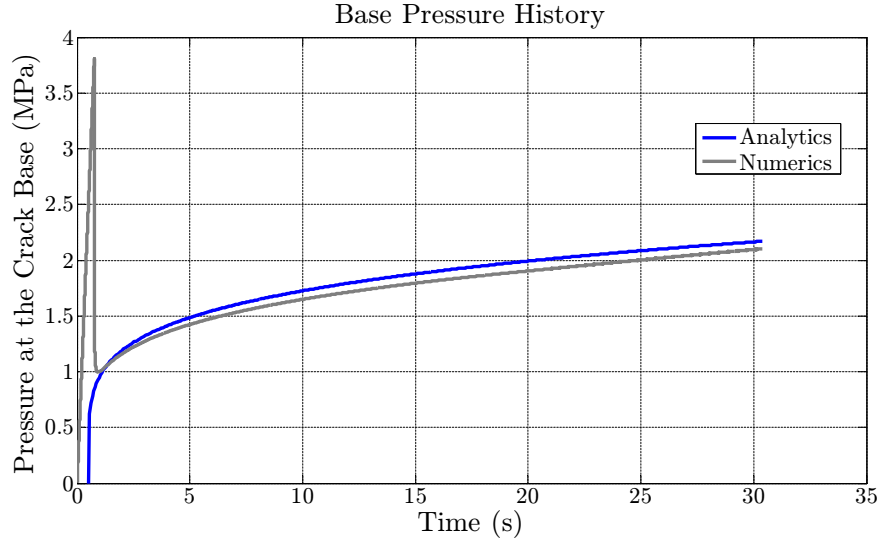


Figure 3.10: Simulation and theory for pressure at crack base. The pressure spike at about 0.5 s corresponds to fracture initiation: pressure in the injection segment initially builds up until the critical extension pressure of the seed crack is exceeded. Once the crack starts to propagate, water flows from the injection segment to newly formed segments and consequently pressure at the injection segment drops. In the simulation plotted here, the crack grew to about 100 m by the end of injection.

Prior to initiation, pressure in the injection segment builds up over time until eventually the local critical extension pressure is reached. At this point a new crack will initiate; that is, a new segment will form. Immediately after initiation, the model takes some water away from the injection segment to fill the new segment, creating a rapid pressure decline at the injection segment.

The pressure buildup and rapid decline therefore mark crack initiation.

Next, we look at the net pressure profile along crack length at the end of injection. As presented in Figure 3.11, the simulation and theory agree reasonably well. The analytical expression plotted in Figure 3.11 is given by equation (3.17),

$$P(x, t) = 4 \left\{ \frac{Q\mu [L(t) - x]}{\pi H \beta^3} \right\}^{\frac{1}{4}} + \sigma_{\perp},$$

where the far-field stress σ_{\perp} is taken to be 0. As was the case for Figure 3.10, the parameter β for Figure 3.11 was taken to be equal to $\frac{2H(1 - \nu^2)}{Y}$.

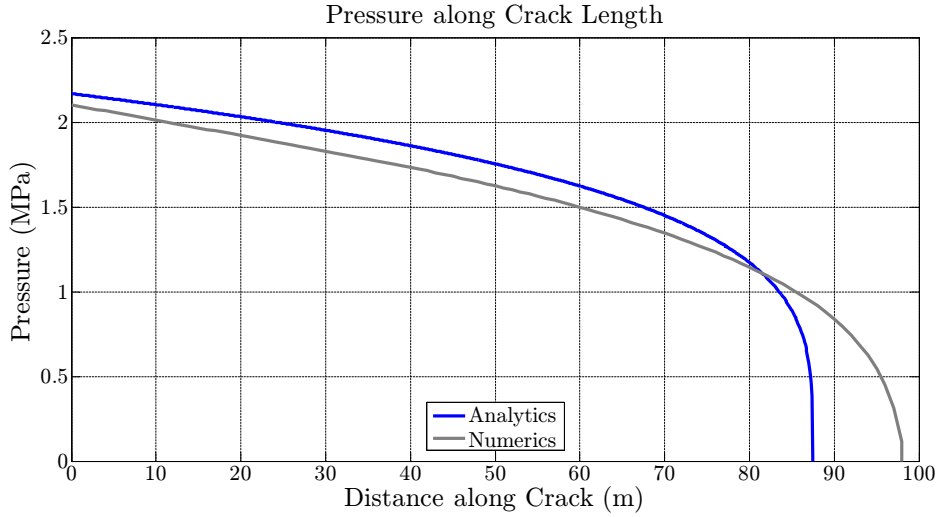


Figure 3.11: Simulation and theory for pressure along crack length. Water was injected into the initial configuration shown in Figure 3.9 for about 30 s. At the end of injection, the analytical crack had reached about 88 m while the numerical crack is about 100 m long. Using a smaller lattice spacing a results in a smaller difference between the two lengths.

The difference between numerical and analytical crack length at the

end of injection can be explained as follows: while analytical propagation is controlled only by the PKN energy criterion, equation (3.20), numerical propagation is controlled not only by the PKN energy criterion but also by the condition which ensures that pressure in the new segment is smaller than or equal to the parent segment, equation (3.45). As discussed earlier, this condition is critical to the stability of the numerical scheme and is required because of the discrete nature of the model: a smaller lattice spacing a reduces the difference between the numerical and analytical crack lengths at the end of injection.

As mentioned earlier, the model takes fluid leak-off to the formation to be negligible. Then conservation of mass requires the total crack volume $V(t)$ to be equal to the total injected water volume at all times. Injection rate is taken to be constant and equal to Q , so we should have

$$V(t) = Qt. \tag{3.46}$$

As presented in Figure 3.12, the numerics match the analytics exactly. Mass is therefore shown to be conserved in the model.

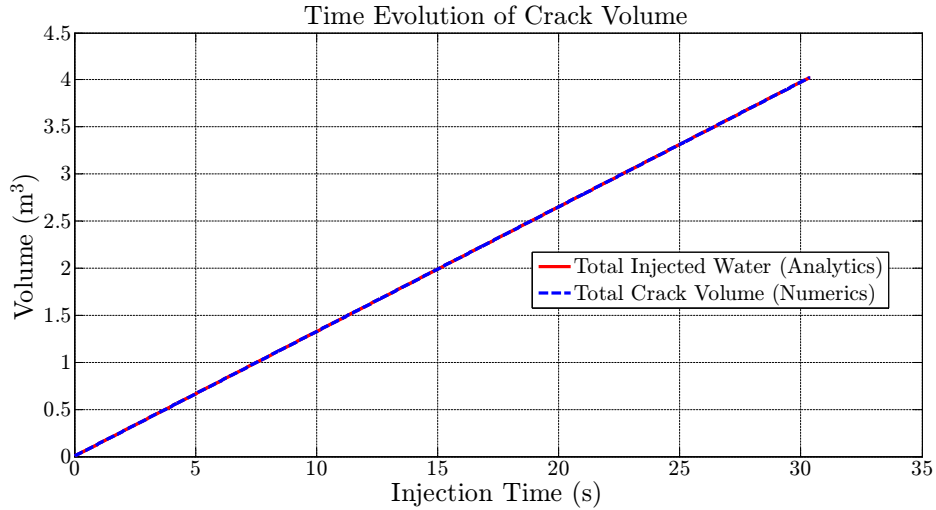


Figure 3.12: Mass is conserved in the model. Since fluid leak-off to the formation is taken to be negligible, the total injected water volume at any time is equal to the total crack volume at that time.

3.6 Qualitative Observations

Having explained the mechanics of the model, we now use the model to investigate how network geometry is created during a treatment. The description presented here is qualitative; we note that the design objective for the model has been to help answer how network geometry affects production, and to answer this question one needs in addition to the model presented in this chapter another model that allows computation of gas production from a given fracture network. The production model developed in this work will be presented in detail in the next chapter.

The first observation is that hydraulic fractures in the model primarily

grow one at a time. We note that this observation is what one should expect from the criterion for crack propagation, equation (3.20), given by

$$\frac{\beta}{3} P_{\text{net}}^2(x=0) > \Gamma.$$

Because seed cracks in the model have different critical static extension pressures (p_c^{static}), in cases where two seed cracks exist at the same location, the seed with the lower critical extension pressure always grows first. Once the seed crack starts to grow, the mechanical energy available for propagation will get increasingly larger than the minimum energy required to create new crack surfaces, as shown by equation (3.20), and the crack will be unstable.

As mentioned earlier, one physical mechanism which ultimately puts a limit on propagation is the competition between the energy needed to start a new crack and the energy dissipated through the fluid: the dynamic crack stops propagating when the dissipation becomes so large that starting a new crack becomes energetically more favorable than continued propagation. It should be noted that hydraulic fractures in the model also stop when they reach the end of the natural fracture/induced crack (the path crack) on which propagation was taking place.

Another observation is that the longer a crack gets, the slower its propagation will be. This observation is consistent with the analysis of Marder et al. (2015) for two cracks propagating from a shared base: if the lengths are L_1 and L_2 and the propagation velocities are \dot{L}_1 and \dot{L}_2 , then

$$\frac{\dot{L}_2}{\dot{L}_1} = \frac{L_1}{L_2}. \quad (3.47)$$

It was observed that branches emerge from a given dynamic crack mostly after the crack had reached the end of its path. The location of the branch is controlled by first the pressure profile along the crack length, which favors branching closer to the base, and second the critical extension pressure of the incipient branches. For a more homogeneous cement, variability in fracture energy and Young's modulus of the incipient branches is low and branches tend to form closer to the base; otherwise, branches can form anywhere on the dynamic crack and even close to the tip.

Snapshots of the time evolution of the hydrofracture network can be viewed in Figure 3.13. The far-field stress in this simulation was assumed to be isotropic, and the parameter β was set equal to $\frac{2H(1-\nu^2)}{Y}$.

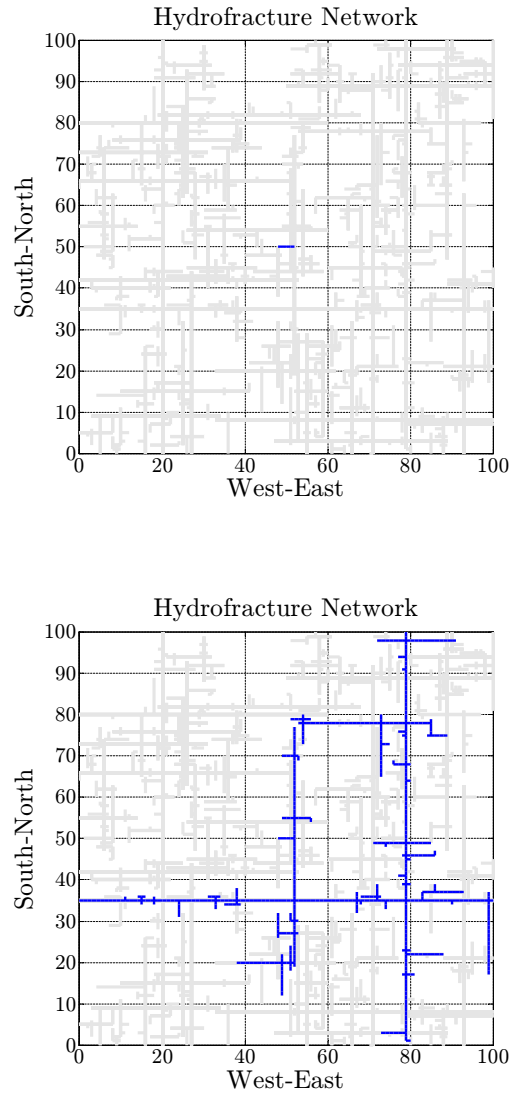


Figure 3.13: Time evolution of the hydrofracture network for relatively heterogeneous cement. Water (blue) is injected at a constant rate at the center, throughout the simulation, and into the natural fracture/induced crack cluster (gray). Top: the initial condition, $L = 4$ m; bottom: the network at about 5 min into injection (physical pumping time in the field), $L = 547$ m. The simulation was carried out with $H = 30$ m, $Q = 50$ bpm, $Y = 50$ GPa, $\nu = 0.25$, and $\mu = 10^{-3}$ Pa s under isotropic far-field stress.

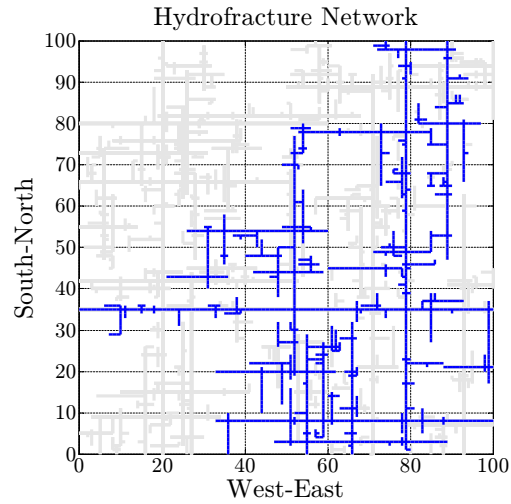
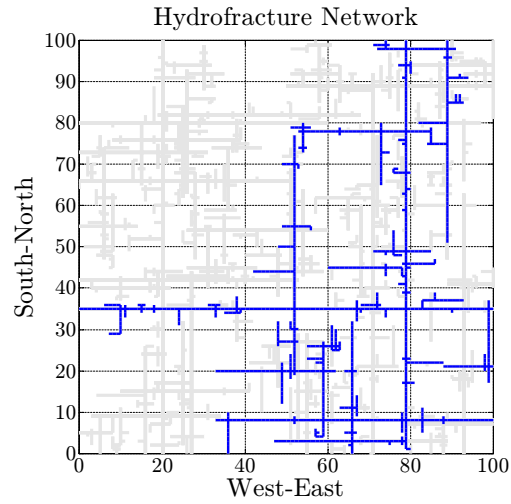


Figure 3.13 (cont.): Time evolution of the hydrofracture network for relatively heterogeneous cement. Water (blue) is injected at a constant rate at the center, throughout the simulation, and into the natural fracture/induced crack cluster (gray). Top: the network at about 10 min into injection (physical pumping time in the field), $L = 952$ m; bottom: the network at about 15 min into the injection, $L = 1316$ m. The simulation was carried out with $H = 30$ m, $Q = 50$ bpm, $Y = 50$ GPa, $\nu = 0.25$, $\mu = 10^{-3}$ Pa s under isotropic far-field stress.

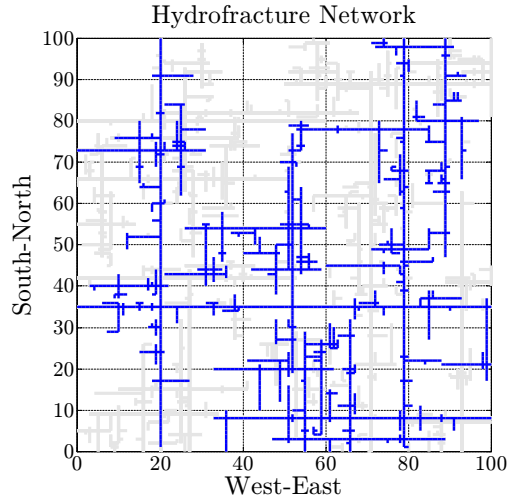


Figure 3.13 (cont.): Time evolution of the hydrofracture network for relatively heterogeneous cement. Water (blue) is injected at a constant rate at the center, throughout the simulation, and into the natural fracture/induced crack cluster (gray). The plot shows the network at about 21 min into the injection (physical pumping time in the field), when $L = 1700$ m. The simulation was carried out with $H = 30$ m, $Q = 50$ bpm, $Y = 50$ GPa, $\nu = 0.25$, $\mu = 10^{-3}$ Pa s under isotropic far-field stress.

To obtain an estimate for the time it takes an operator in the field to reach each snapshot, we first scale each simulation parameter with a corresponding canonical (reference) value. We take the canonical values to be $H_0 = 30$ m, $Y_0 = 50$ GPa, $\nu_0 = 0.25$, $L_0 = 100$ m, $Q_0 = 50$ bpm and $\mu_0 = 10^{-3}$ Pa s. The dimensionless quantities are then given by $\tilde{H} = \frac{H}{H_0}$, $\tilde{Y} = \frac{Y}{Y_0}$, and so on. We then use the expression for the time it takes a dynamic PKN crack to reach a given length L ,

$$t = 35.9 \left(\frac{\tilde{\mu} \tilde{L}^5 \tilde{H}^4}{\tilde{Q}^3 \tilde{Y}} \right)^{\frac{1}{4}} \text{ s}, \quad (3.48)$$

where in the simulations $\tilde{L} = \frac{\text{number of channel segments} \times \text{lattice spacing}}{L_0}$.

In reality, a dynamic hydraulic fracture exerts compressive stress on the surrounding shale, opposing the growth of new fractures nearby. This phenomenon is known as the stress shadow effect.

In this model, propagation of a fracture does not affect other fractures. In other words the stress shadow effect does not come out of the model based on the underlying assumptions and has to be explicitly added to the model. This addition is left for future work. We note that an analytical estimate of the stress shadow effect has been obtained recently by Geilikman and Wong (2013).

3.7 Conclusions

Prior to this chapter, we used the percolation analysis of Chapter 2 to obtain the spanning cluster for a given natural fracture/induced crack network. We suggested that it is energetically more favorable for hydraulic fractures to be restricted to the spanning cluster, and concluded that the spanning cluster contains the potential paths of hydraulic fractures.

We presented in this chapter a numerical framework to simulate initiation and propagation of hydraulic fractures, as well as the interaction of hydraulic fractures with natural fractures/induced cracks. The model allows an investigation of how the geometry of hydrofracture networks is created. Given the desire to include the interaction of hydraulic fractures with a large

number of natural fracture/induced cracks, and having made computational efficiency a priority, we adopted in this chapter an “intermediate” level of including details; we use the Reynolds lubrication approximation to model fluid flow through hydraulic fractures and rely on analytical estimates to model the stress response. The model is constructed on a square lattice and is pseudo-three-dimensional.

The model was validated against the Perkins-Kern-Nordgren theory. The numerics are in reasonable agreement with theory and as originally intended, the model is computationally efficient.

We concluded the chapter with an analysis of the qualitative observations made during simulations. Hydraulic fractures mostly seemed to propagate one at a time and got slower as they grew longer. Branching was observed to happen primarily after hydraulic fractures had reached the end of their natural fracture/induced crack path. A more mechanically homogeneous cement tends to lead to branches which form close to the base of dynamic cracks, while more heterogeneity allows branches to form farther from the base and even close to the tip of a dynamic crack.

The model was designed to ultimately help describe how network geometry affects gas production. The work presented so far in this dissertation predicts the fracture network responsible for gas production, and an additional model is needed to compute gas production from the predicted network. The next chapter presents such a model.

Chapter 4

Production from Complex Fracture Networks

So far in this dissertation, we have established that hydraulic fracturing of shale reservoirs results ultimately in a network of connected fractures, which we refer to as the fracture network, and that the observed field production of shale gas is due to this network. We discussed that the network drains gas from the rock and provides hydraulically conductive pathways to the flow of gas from the formation to the wellbore. Natural gas was described to travel through two distinct transport paths during production: gas is first transported from the organic matter inside the shale through the shale to the hydrofracture network, and then through the network fractures to the wellbore.

The work presented so far allows one to describe the geometry of the fracture network at any time during injection. The question we raise and address in this chapter is how the geometry affects production. In particular, we focus in this chapter on the scaling of gas production from hydraulically fractured shales and identify the characteristic length scale of the fracture network.

We present in this chapter a diffusion model which makes it possible to predict the time evolution of gas production in fractured shales. The model is

based on the random walk algorithm and operates on the network geometry which results from the percolation model of Chapter 2 and/or the hydrofracture model of Chapter 3.

For fracture networks of different size and geometry, the diffusion model reproduces Patzek et al.'s (2013) universal scaling curve. The two models are different in how they treat the effect of fracture network on production: the diffusion model explicitly considers the fracture network and solves the transport problem with the fractures as the boundary, while Patzek et al.'s model treats hydrofractured shale as a homogeneous medium of a permeability equal to the lab measured value for unfractured shale, bounded between parallel planar hydrofracture stages which are spaced very closely (on the order of a meter). In the Patzek et al. model, hydrofractures are constant pressure sinks of infinite hydraulic conductivity. We show that the two models nevertheless lead to exactly the same universal scaling. The consistency between the two works confirms that the setup of the models is indeed the correct mental picture for gas production from hydraulically fractured horizontal shale wells.

4.1 Outline

We start this chapter with the formal statement of the initial boundary value problem which governs gas production from hydrofractured shales. We discuss the underlying assumptions first and then present the derivation. The governing equation here is the gas pseudo–pressure diffusivity equation.

We then present a diffusion model based on random walk on a square

lattice to numerically solve the gas diffusivity equation. We establish how the model may be used to compute the characteristic scales which control gas production. We then run the diffusion model for a number of fracture networks of different size and geometry and scale the numerically obtained cumulative production versus time data with respect to the characteristic scales. We show that the scaled plots reproduce the universal scaling curve first proposed by Patzek et al. (2013), a solution which was shown to match the production history of more than 8,000 horizontal gas wells in the Barnett Shale.

Finally, we use the model to define the characteristic spacing of fracture networks. We find that the characteristic distance of a given fracture network is the average distance from a random point in the area drained by the fracture network to the nearest fracture of the network.

4.2 Background and Literature Review

We present in this section a review of relevant results from the literature on modeling the production decline in unconventional reservoirs. As discussed earlier, the natural gas present in shale reservoirs is adsorbed in nano-scale pores and due to the extremely low permeability of the shale matrix the gas does not naturally flow through the reservoir rock. Hydraulic fracturing creates a multi-scale network of connected fractures which drains the gas from shale and provides hydraulically conductive pathways to the flow of gas to the wellbore. For a detailed discussion of the nature of the fractures which make up the network, as well as the network geometry and scaling of connectiv-

ity, the reader is referred to Chapter 2; the mechanics of hydraulic fracture propagation were discussed in detail in Chapter 3.

In the first 3 months after a well is hydraulically fractured, back-production of the injected water along with the gas, as well as the spontaneous imbibition of the injected water into the shale, make it difficult to predict the gas production. Due to this difficulty, in the present research, as well as in for instance Patzek et al. (2013), production is investigated only after the initial production transients and the associated transient phenomena have passed.

An additional effect present during shale gas production is desorption. Desorption refers to the escape of adsorbed shale gas due to pressure falling during production and is described by the Langmuir isotherm. Patzek et al. (2013) note that in the particular case of the Barnett Shale the contribution of desorption to gas production is negligible, yet warn that this may or may not be the case for other fields.

The analysis by Patzek et al. shows that gas production is dominated by the effective properties of a fracture network and that “the net effect is pressure diffusion at an enhanced rate in a homogeneous medium”. As such, their analysis establishes that one can safely skip the nonlinear behavior of desorption and gas flow in the unfractured shale at the microscopic scale and still arrive at a reasonable prediction for production.

The geometrical setup employed by the Patzek et al. (2013) model can be seen in Figure 4.1. This geometry was suggested earlier by Al-Ahmadi et

al. (2010) as the right starting point for modeling the application of linear flow analysis to shale gas wells.

In the setup, hydrofractures are taken to be parallel planes of height $H \sim 30$ m and tip-to-tip length $2L \sim 200$ m, uniformly spaced at $2d \sim 100$ m. Gas is taken to come entirely from inside the cuboid region bounded between consecutive stages, and is taken to flow linearly into each stage from both sides. Permeability of hydrofractures is taken to be infinite compared to the effective permeability of the surrounding shale.

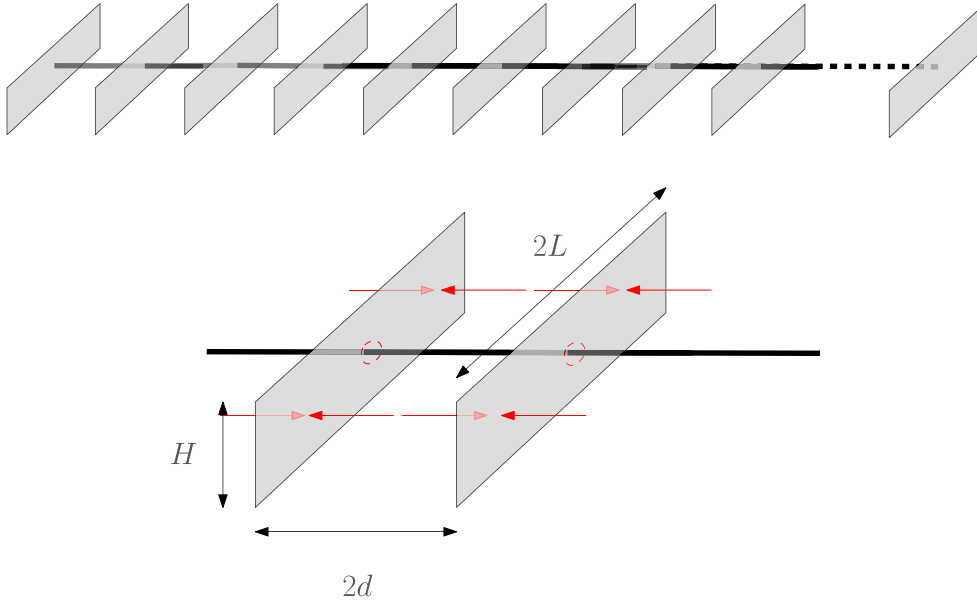


Figure 4.1: Geometrical setup of the Patzek et al. (2013) model. Each hydrofracture stage is taken to be a plane perpendicular to the horizontal well, spaced a distance $2d$ apart from the nearest stage. In practice, it is typical to have 10-20 stages over the entire length of the horizontal well. All hydrofractures are assumed to be of the same height H and the same length $2L$. Natural gas is taken to flow linearly into each stage from both sides. Permeability of the hydrofractures is taken to be infinite compared to that of the surrounding shale. As a result, natural gas in the model is instantly produced when it reaches any hydrofracture stage. (Taken with permission from Patzek et al., 2013)

The model treats hydrofractured shale (i.e., inside the cuboid) as a homogenous region of uniform permeability, bounded between parallel planar hydrofracture stages the spacing between which is small (if shale permeability is taken to be 10 nD , the spacing comes out to $1.5 - 3\text{ m}$). This choice makes it possible to skip the geometrical details of the hydrofracture network and greatly simplifies the boundary conditions of the transport equation.

The transport problem solved in this dissertation is a variation of the transport problem solved by Patzek et al. (2013). Before we present the details of our problem later in section §4.3, in the following section we re-trace the derivation and the formal statement of Patzek et al.’s transport problem- an initial boundary value problem which describes gas pressure diffusion from inside a cuboid region to parallel planar absorbing boundaries on the sides of the cuboid (see Figure 4.1). The diffusion problem in this setup has been studied also by Silin and Kneafsy (2012) and Nobakht et al. (2012).

4.2.1 Derivation of the Transport Problem

We now present the transport problem that corresponds to production from the geometrical setup described in the previous section. We note that the following derivation describes production after the initial transients have ended, during which gas flow from the cuboid region to the hydrofractures resembles flow from inside a semi-infinite body to an absorbing boundary.

Starting with the mass balance equation, we have

$$\frac{\partial (\phi S_g \rho_g + (1 - \phi) \rho_a)}{\partial t} + \nabla \cdot (\rho_g u_g) = 0, \quad (4.1)$$

where the subscript g denotes free gas; a , adsorbed gas. S is saturation, ϕ is porosity, ρ is density and u is velocity. We now substitute for u_g using Darcy’s equation,

$$u_g = -\frac{k}{\mu_g} \nabla P, \quad (4.2)$$

and obtain the diffusivity equation:

$$\frac{\partial(\phi S_g \rho_g + (1 - \phi) \rho_a)}{\partial t} = \nabla \cdot \left(\frac{k \rho_g}{\mu_g} \nabla P \right). \quad (4.3)$$

As shown by Al-Hussainy et al. (1966), employing the real gas pseudo-pressure (the Kirchhoff integral transform of gas pressure),

$$m(p) = 2 \int_{p^*}^p \frac{p dp}{\mu_g z_g}, \quad (4.4)$$

simplifies the nonlinear equation (4.3) into

$$\frac{\partial m(p)}{\partial t} = \alpha(p) \nabla^2 m(p), \quad (4.5)$$

where

$$\alpha(p) = \frac{k}{[\phi S_g + (1 - \phi) K_a] \mu_g c_g}, \quad (4.6)$$

and

$$K_a = \left(\frac{\partial \rho_a}{\partial \rho_g} \right)_{T=\text{const.}}. \quad (4.7)$$

The reference pressure p^* is set equal to the wellbore flowing pressure, p_f . Note that p_f is also the hydrofracture pressure. The coefficient α is known as the hydraulic diffusivity of gas and depends on pressure; $K_a = K_a(T, p)$ is defined as the differential equilibrium partitioning coefficient of gas at a constant temperature.

The initial condition for equation (4.5) is

$$m[p(x, t = 0)] = m(p_i) = m_i, \quad (4.8)$$

where m_i is constant in a virgin reservoir. In the case of a hydrofractured reservoir, m_i will depend on the distance to the hydrofractures.

The boundary condition for equation (4.5) is specified pseudopressure on the hydrofractures:

$$m [p(x = x_{\text{hydrofractures}}, t)] = m(p_f) = m_f, \quad (4.9)$$

where m_f can be kept constant or gradually reduced over time.

The current form of equation (4.5) is dimensional: physical quantities such as time, length and mass are measured in units which are defined independent of the time, length and mass scales present in the system. If one chooses to use the SI system, for instance, then regardless of the system under consideration, time will be given in seconds, length will be measured in meters and mass will be in units of Kilogram. Instead, one can define scaling parameters which are based on the scales present in the system and scale equation (4.5) with respect to those parameters to obtain a dimensionless form.

We note that the choice of the scaling parameters is not mathematically unique. However, those scaling parameters which represent physically characteristic scales of the system scale the dimensional solution into a *universal* dimensionless form, where universality means the solution is identical for *every* system size. Universal solutions are simpler, more general (the solution is scale-independent) and more useful than their corresponding dimensional forms.

Once discovered, characteristic scales can be used to describe the governing physics in a scale-independent fashion. We note, however, that there is no well-established, step-by-step procedure to discover the characteristic scales of a given physical system. In the case of the transport problem considered here, the governing physics is that of pseudopressure diffusion to parallel planar absorbing boundaries and the characteristic scales as first obtained by Patzek et al. (2013) are a time-scale τ , referred to as *the time to interference*, and a characteristic mass M , which represents the original mass of gas contained in the reservoir volume drained by the well.

The characteristic time unit τ is defined in terms of the initial reservoir properties as

$$\tau = \frac{d^2}{\alpha_i}, \quad (4.10)$$

where d is half the distance between two consecutive hydrofracture planes, see Figure 4.1, and α_i is the hydraulic diffusivity at initial reservoir temperature and pressure:

$$\alpha_i = \frac{k}{\phi\mu C_g S_g} \Big|_{\text{initial reservoir } T, p}. \quad (4.11)$$

The characteristic time τ represents the time it takes for the pressure wave to travel from one hydrofracture stage to the plane located mid-way to the nearest hydrofracture, at which point the wave will interfere with the wave from the nearest hydrofracture and pressure at the mid-plane drops to below the initial reservoir pressure.

The choice to evaluate α at the initial reservoir condition does not

mean that the solution will depend on a specific value of α , but rather that the solution will be given in terms of a time unit, τ , which is defined based on α_i . Besides, as will be presented next, the procedure to compute τ does not require knowledge of the magnitude of α_i .

Having defined the characteristic time, the dimensionless time \tilde{t} can now be defined as

$$\tilde{t} = \frac{t}{\tau}. \quad (4.12)$$

The dimensionless cumulative production is called the recovery factor RF and is defined as

$$\text{RF} = \frac{m(t)}{M}, \quad (4.13)$$

where $m(t)$ is the cumulative production at a given time t .

For the geometry shown in Figure 4.1 and a constant hydraulic diffusivity, the diffusion problem given by equation (4.5) was solved analytically by Patzek et al. (2013), giving the following expression for the gas flow rate into the hydrofracture plane:

$$\dot{m} = \frac{M}{\tau} \sum_{n=0}^{\infty} \exp\left(-\frac{(2n+1)^2 \pi^2 \tilde{t}}{4}\right). \quad (4.14)$$

Scaling the production rate \dot{m} with τ and M yields the (dimensionless) recovery rate $\frac{\partial \text{RF}}{\partial \tilde{t}}$, which can be approximated as the sum of a square root of time decline and an exponential decline:

$$\frac{\dot{m}}{M} = \frac{\partial \text{RF}}{\partial \tilde{t}} \approx \frac{\sqrt{\pi} \text{erfc}\left(3\sqrt{\frac{\pi^2 \tilde{t}}{4}}\right)}{4\sqrt{\frac{\pi^2 \tilde{t}}{4}}} + \exp\left(-\frac{\pi^2 \tilde{t}}{4}\right) + \frac{1}{2} \exp\left(-\frac{9\pi^2 \tilde{t}}{4}\right). \quad (4.15)$$

The square root of time decline describes early time production and emerges from the diffusion of gas pressure from high in the reservoir to low on the hydrofractures. As time goes by, reservoir pressure gradually decreases until at $t = \tau$ the pressure halfway between the hydrofractures drops to below the initial reservoir pressure and production slows relative to the square root of time decline. As for the exponential decline, with continued production there comes a point at late time (i.e., $t \gg \tau$) when the rate of gas production becomes proportional to the amount of unproduced gas still inside the reservoir, giving rise to the exponential decline regime.

Patzek et al. (2013) note that ignoring the variations in properties of natural gas with pressure leads to errors on the order of 50%, and solve equation (4.5) using a numerical ODE solver which treats the thermodynamic properties of natural gas properly. The numerical solution consists of a square root of time decline trend followed by an exponential decline, and agrees well with the observed field recovery rate for typical Barnett wells, Figure 4.2.

5 typical wells in Barnett showing interference

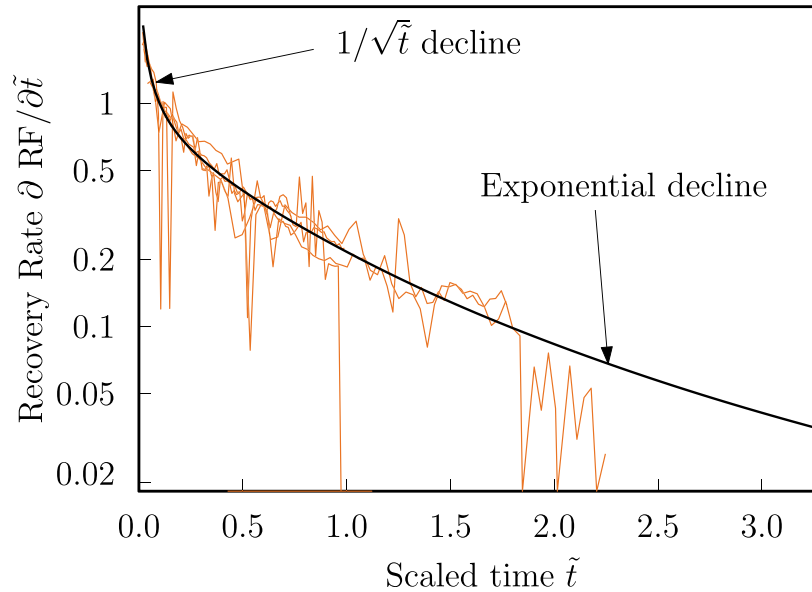


Figure 4.2: Dimensionless production rate versus dimensionless time, theory (black) and field data (burnt orange) for 5 typical wells in the Barnett Shale. Time (the horizontal axis) has been scaled with the time to interference, τ ; production rate (the vertical axis), with the mass of original gas in place, M . The decline trend at early time is square root of time and emerges from the diffusion of gas pressure from the reservoir to the hydrofractures. At $\tilde{t} = 1$ (the time to interference), gas pressure halfway between the two hydrofractures drops below the initial reservoir pressure and decline slows relative to the square root of time trend, followed at late time by an exponential decline. The exponential trend arises because eventually gas production rate becomes proportional to the amount of unproduced gas still inside the reservoir. (Taken with permission from Patzek et al., 2013)

For a given horizontal shale gas well, M and τ are obtained from fitting the solution of equation (4.5) to the field production data. Patzek et al. (2013) use the numerical solution, which accounts for thermodynamics of real gas; we

use the integral of equation (4.15), which describes cumulative production in the case of constant hydraulic diffusivity. The analytical expression for the cumulative production has been derived analytically in the present dissertation and will be presented later in section §4.3.

With M and τ known, one can now scale the cumulative production versus time data for any given (horizontal shale gas) well. This process was done by Patzek et al. (2013) for 2057 Barnett wells and the scaled curves can be seen in Figure 4.3. Note that all of the scaled curves fall more or less on a single scaling function. This means that the scaling function is universal, and further confirms that the proposed scaling parameters M and τ are indeed the characteristic physical scales which control shale gas production.

2057 wells in Barnett, $\tilde{t}_{\min} < 0.25$ & $\tilde{t}_{\max} > 0.64$

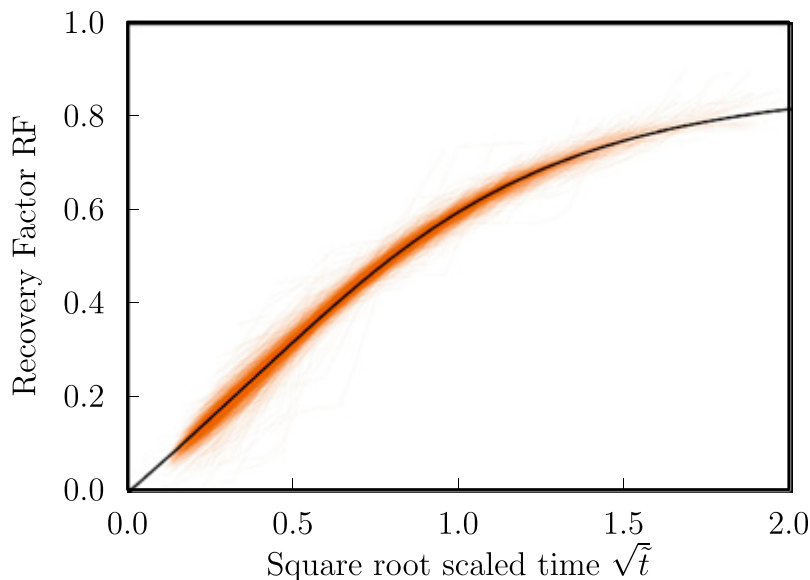


Figure 4.3: Scaled cumulative production history, theory (black) and field data (burnt orange) for 2057 wells in the Barnett Shale. The orange curves have been obtained by scaling the cumulative production versus time data of each well with the corresponding M and τ for the well. Each well in general has a different set of M and τ , which are computed from fitting the cumulative production versus time data to the numerical solution of equation (4.5). The black curve here is the universal solution. Universality here refers to how the scaled curves for different wells all fall on a single scaling curve (the universal solution) and highlights that the scaling parameters M and τ indeed represent the characteristic scales of shale gas production from hydrofractured horizontal wells. Pressure on the hydrofractures (wellbore flowing pressure) was taken to be 500 psi; reservoir pressure, 3500 psi. Because wellbore flowing pressure has been non zero, the wells could not have produced all of the original gas in place, and the ultimate recovery factor is around 0.8. (Taken with permission from Patzek et al., 2013)

4.3 The Model

Having established the context for this chapter, we now move on to original work and start by introducing our model in this section.

As mentioned earlier, the transport problem solved in the present dissertation is a variant of the problem introduced in section 4.2.1, given by equation (4.5):

$$\frac{\partial m(p)}{\partial t} = \alpha(p) \nabla^2 m(p).$$

In particular, two features distinguish our model from that of Patzek et al.'s. First, we relax the assumption that the boundary of equation (4.5) is two parallel planar hydrofractures and instead consider a network of fractures as the boundary. Patzek et al.'s model treats the diffusion of gas pressure from the reservoir to the production network as being effectively equivalent to diffusion of gas pressure to two parallel planar hydrofracture stages from a homogenous, fracture-free reservoir of uniform permeability; here we consider the production network explicitly and model gas pressure diffusion to it.

Second, we consider natural gas to be ideal. This choice is made specifically to allow us to ignore the pressure dependence of α and instead replace it with a constant, at which point the solution to equation (4.5) can be obtained efficiently using the basic random walk algorithm. The desire to take the random walk approach is motivated by the complex geometry of the boundary and the diffusive nature of equation (4.5). We note that in principle it is possible to extend the basic random walk to allow the possibility of a pressure dependent

diffusivity; we also note that natural gas is not ideal and its compressibility and viscosity vary strongly with temperature and pressure. In any case, as the results will show later, taking natural gas to be ideal still results in exactly the same universal scaling of cumulative production as the one introduced by Patzek et al. (2013).

The numerical framework used in this dissertation to solve equation (4.5) and compute production is based on a Monte Carlo implementation of the basic random walk. Before presenting the framework in details, we first introduce random walk, establish how it leads to the diffusion equation, and demonstrate how random walk may be used to solve any linear diffusion equation.

As the name suggests, random walk describes how a *random walker* moves by taking *random steps*. In general, direction and length of each step is random. The classic example of random walk is the Brownian motion; for instance, in the case of gas molecules, a given gas molecule will continue to travel along a straight line until it collides with another molecule, at which point the molecule will be deflected into a random orientation. Because all gas molecules move randomly, the distance the molecule travels before the next collision, i.e. the step length, is also random.

To demonstrate how random walk leads to the diffusion equation, we now discuss the limiting case of a random walk with infinitesimally small and constant step length l and constant time step τ . Take t to represent the time elapsed from the start of the walk and $\vec{r}(t)$ to mark the location of the walker at time t and with respect to the initial position of the walker. Then it can

be shown that the probability density of finding the walker at location $\vec{r}(t)$ at time t is the solution to the linear diffusion equation

$$\frac{\partial p(\vec{r}(t), t)}{\partial t} = D \nabla^2 p(\vec{r}(t), t), \quad (4.16)$$

where D is called the diffusion coefficient and depends on the step length, time step of the walk and the dimensions of the system. In two dimensions, for instance, D is given by

$$D = \frac{l^2}{4\tau}, \quad (4.17)$$

where l is the step length and τ is the time step of the walk. The diffusion coefficient D will be a constant only if l and τ are both constant.

Going back to Brownian motion in gases, we note that gases contain more than only one molecule and that gas molecules interact. Generally, the interaction between a large number of random walkers leads to a variable D , one which will be a function of the local concentration of walkers. In the case of natural gas, for instance, D , i.e., α in equation (4.5), is a function of gas pressure and temperature. Taking α to be constant means taking the interaction between the walkers to be negligible, which physically corresponds to ideal gas and mathematically manifests as a linear diffusion equation.

Having laid out the general idea of random walk, we now present the details of our numerical framework. The geometrical setup of the model is presented in Figure 4.4. The fracture network here is one which spans the lattice and is generated by the percolation model of Chapter 2: fracture length follows a power law distribution and fractures are uniformly placed on the

bonds of a square lattice, such that a single fracture may span several bonds. The lattice is a square of side length L , tiled by squares of side length a (the lattice spacing). For the lattice shown in Figure 4.4, $L = 200$ and $a = 1$.

Conductivity of fractures is taken to be infinite compared to the shale matrix, therefore the width of fractures does not play any role here: fractures are treated as features extruded uniformly in the height direction (into the page in Figure 4.4) and the model is pseudo-three-dimensional. The thickness of the blue lines in Figure 4.4 is only a visual representation and does not signify any physics. We note that the diffusion model may be extended to allow the possibility of finite conductivity fractures: because hydraulic conductivity depends on fracture aperture, the diffusion model has to be modified such that fractures of different widths can exist, and the value of α inside each fracture will be a function of the width. The case of finite conductivity fractures will be discussed in detail in section 5.3.6.

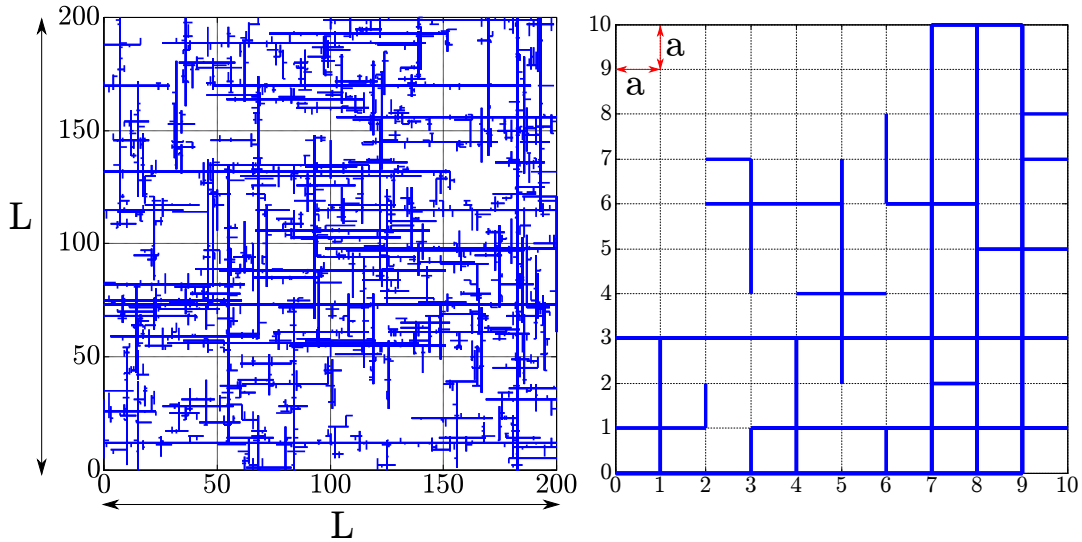


Figure 4.4: Geometrical setup of the diffusion model. The lattice on the right is a close up of a 10×10 subdomain of the lattice on the left. The fracture network (blue) is generated by the percolation model of Chapter 2 and is constructed on the bonds of a square lattice. The lattice is a square of side length L and is tiled by squares of side length a (the lattice spacing). Each fracture may span several bonds. Fractures are infinitely conductive compared to the shale matrix, so as soon as natural gas hits any fracture, it is produced. The fracture network is therefore an absorbing boundary to the gas transport equation.

Regardless of what the fracture network geometry is or how it was obtained, we expect the characteristic time and mass scales of production from the fracture network to scale the time evolution of cumulative production from the network onto the universal solution. Therefore the fracture networks in the diffusion model may be at or above the percolation threshold and it does not matter whether or not the networks were processed through the hydrofracture model of Chapter 3.

We use a random walk scheme in this dissertation to solve equation (4.5). Mathematically, the domain on which we solve equation (4.5) is the area inside the lattice; the boundary is the union of the lattice boundary and the fracture network. The random walker in our algorithm represents a finite mass of gas. As we will show later in this section, the procedure by which we scale the random walk simulation does not require us to specify the mass of the walker.

We place a walker at the center of each $a \times a$ tile inside the lattice and one by one, let each walker take random steps. Each walk is treated as if the walker is alone in the lattice, because the gas in our model is ideal and therefore the walkers do not interact. Also because of the ideal gas assumption, the hydraulic diffusivity α has to be a constant, so step length in the algorithm is a constant and taken to be equal to the lattice spacing a , the walkers jump to one of the four neighboring $a \times a$ squares with equal probability, and the time step of the walk is also a constant.

The lattice boundary in the model is reflective: if a given walker jumps outside the lattice, the walker will be brought back to its position right before the jump. We note that the diffusive nature of transport in the present problem allows flexibility for the choice of condition on the lattice boundary, and the boundary may as well have been taken to be absorbing. Mathematically, a reflective boundary corresponds to the no flow (Neumann) boundary condition.

Each walker is allowed to walk until it crosses any fracture. At this point the walker is removed from the lattice, and the number of steps from the initial location of the walker to the fracture, also known as the *arrival time*, is

recorded. Once all of the walkers have completed their walks, the distribution of arrival time for all walks is constructed next. For a given value of arrival time, the distribution gives the number of walkers which have arrived at any fracture at the given arrival time.

The functional form of the arrival time distribution is the same as that of production rate versus time. For the arrival time to correspond to physical time and the number of walkers to correspond to production, the distribution has to be scaled properly first. To scale the numerics, we fit the cumulative distribution of arrival time using the analytical solution for the cumulative mass of gas flowing into a planar hydrofracture. It is from this fitting procedure that we obtain the characteristic time to interference, τ , and the original gas in place, M .

The analytical solution for the production rate in the case of constant α was given earlier by equation (4.15). Integrating the production rate to get cumulative production, we obtain

$$\int_0^{\tilde{t}} \frac{\partial \text{RF}}{\partial \tilde{t}_0} d\tilde{t}_0 = \text{RF}(\tilde{t}) =$$

$$\frac{2}{3\pi^{\frac{3}{2}}} \left[\frac{3\pi}{2} \sqrt{\tilde{t}} \operatorname{erfc} \left(\frac{3\pi}{2} \sqrt{\tilde{t}} \right) - \frac{\exp \left(-\frac{9\pi^2}{4} \right) - 1}{\sqrt{\pi}} \right]$$

$$- \frac{4}{\pi^2} \exp \left(-\frac{\pi^2 \tilde{t}}{4} \right) - \frac{2}{9\pi^2} \exp \left(-\frac{9\pi^2}{4} \tilde{t} \right) + \frac{38}{9\pi^2}. \quad (4.18)$$

We now consider two fitting parameters, τ^* and M^* , and replace $\text{RF}(\tilde{t})$ in

equation (4.18) with

$$\text{scaled cumulative number of walkers} = \frac{\text{cumulative number of walkers}}{M^*},$$

replace \tilde{t} with

$$\text{scaled arrival time} = \frac{\text{arrival time}}{\tau^*},$$

and compute those values of M^* and τ^* which provide the least-squares fit to equation (4.18). The computed values for τ^* and M^* give, respectively, the characteristic time to interference τ and the original gas in place, M .

For the example system shown in Figure 4.5, the fits to cumulative production and the production rate are presented in Figure 4.6 and Figure 4.7, respectively.

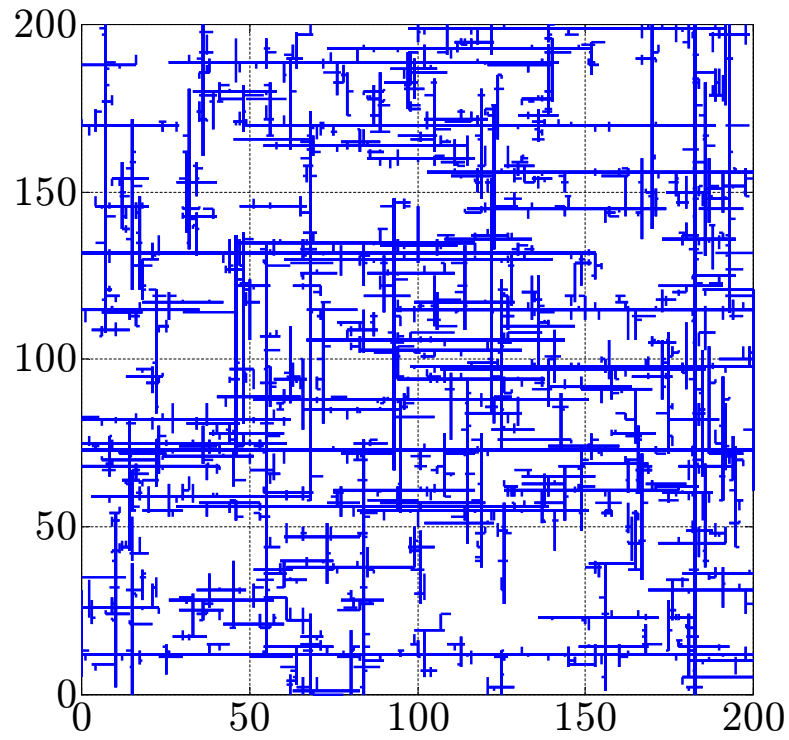


Figure 4.5: A 200×200 lattice system containing a spanning fracture network (blue). The system is discussed as an example in the text to demonstrate the procedure to compute M and τ .

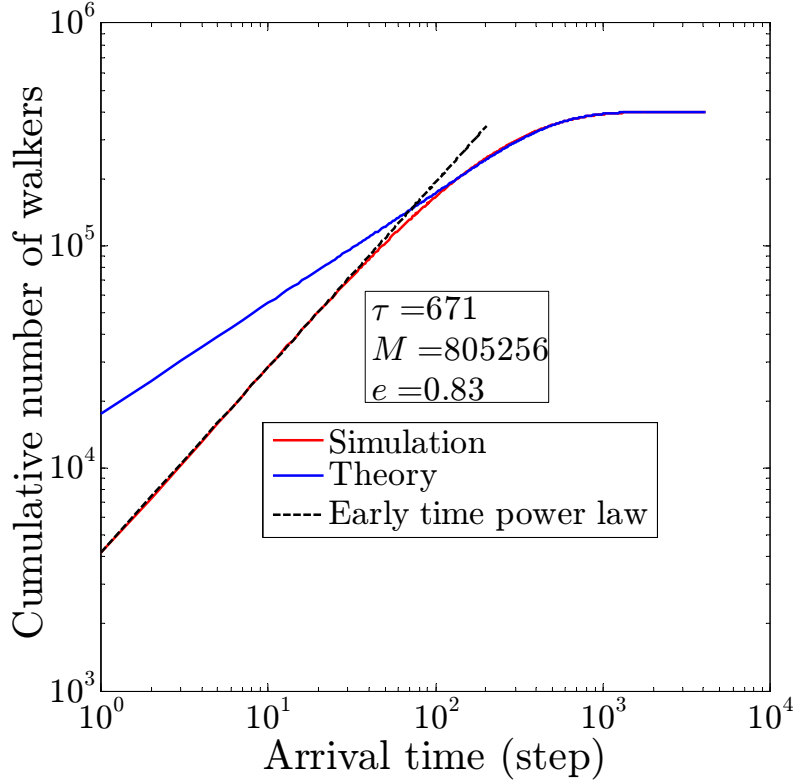


Figure 4.6: The procedure to compute the characteristic time to interference and the original gas in place is based on computing the least squares fit of equation (4.18) to the cumulative distribution of arrival time. The arrival time data in the plot is obtained from running the random walk algorithm on the example system of Figure 4.5. To obtain a smooth enough distribution, we have swept through all the walkers 10 times and pooled the recorded arrival time data. The fitting parameters τ and M are the original gas in place and the characteristic time to interference, respectively; τ ([=] steps) scales the arrival time data onto physical time and M ([=] walkers) scales the cumulative number of walkers onto cumulative production. The dashed black line represents a power law fit to early time simulation data. The exponent of the power law fit is given by e .

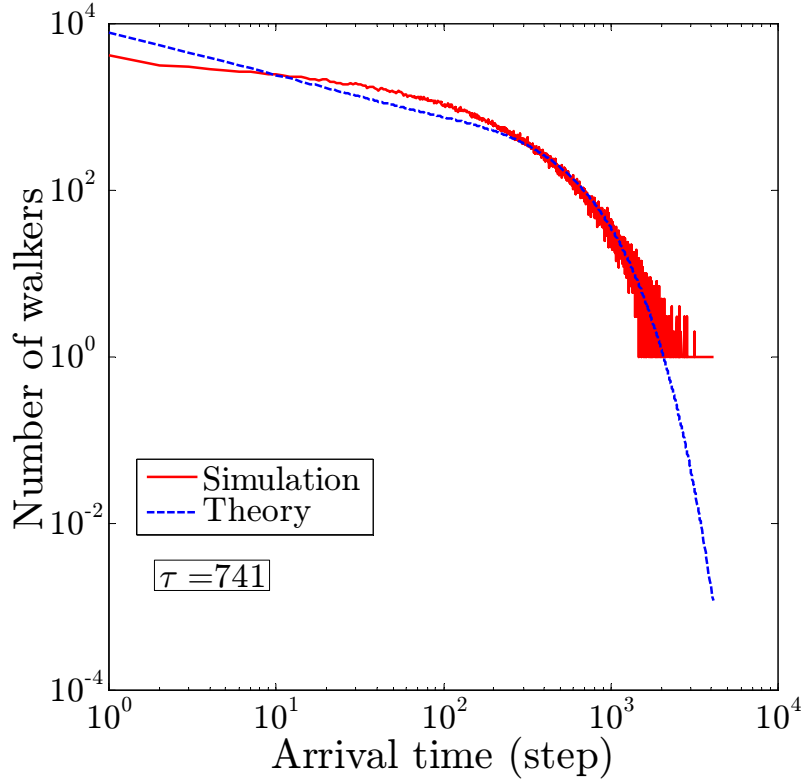


Figure 4.7: Least squares fit of equation (4.15) to the distribution of arrival time, obtained from running the random walk algorithm on the example system of Figure 4.5. The statistical fluctuation is most pronounced at large arrival times and gets smaller with increasing the number of realizations. To obtain a smooth enough distribution, we have swept through all the walkers 10 times and pooled the recorded arrival time data. Taking the cumulative of the number of walkers smooths the fluctuations and leads to a value for τ which is slightly different from the one in Figure 4.6.

We note that the value of τ computed from fitting the cumulative production is close to the one obtained from fitting the production rate, but the two values are not identical (671 for the cumulative fit and 741 for the rate fit).

The difference is not unexpected: there is statistical fluctuation in the (numerical) production rate data, most pronounced at large arrival times, which is inherent to the Monte Carlo scheme and gets smaller as the number of realizations increases. To obtain a smooth enough distribution, we have swept through all the walkers 10 times and pooled the recorded arrival time data. Taking the cumulative of the rate data acts as a low pass filter and smooths out the fluctuations, as can be seen from comparing Figure 4.7 to Figure 4.6, and therefore we expect the values of τ from the two fits to be close, but not identical.

As shown in Figure 4.6, early time production data from the diffusion model follow a power law of the exponent $e \approx 0.8$. This trend is systematically *not* captured by equation (4.18), which predicts an exponent of 0.5 (square root of time) for early time production. We suspect that the early time 0.8 power law might be a signature of the fracture network geometry, since the derivation of equation (4.18) is based on parallel planar hydrofractures and does not include any network geometry. In addition, emergence of the power law implies the relevance of fractal analysis and suggests scale-independence during initial production transients. Further investigation of these ideas is left for future work.

We now use equation (4.10) to estimate the time it takes natural gas in the field to diffuse over a distance equal to the lattice spacing, a . We note that diffusion over the distance a in the field is mimicked in the diffusion model with a single random step on the lattice. Taking $a = 1 \text{ m}$ and $\alpha = 10^{-8} \frac{\text{m}^2}{\text{s}}$,

we get

$$\Delta t = \frac{d^2}{\alpha} = \frac{1}{10^{-8}} = 10^8 \text{ sec} \approx 3.17 \text{ year}, \quad (4.19)$$

so it takes natural gas about 3 years to diffuse over a distance of 1 m in the field.

4.4 Validation & Results

For any given fracture network, the diffusion model described in section §2.5 allows us to compute the cumulative production versus time, as well as the characteristic time and mass scales τ and M . We show in this section that the model exactly reproduces Patzek et al.'s universal scaling curve for cumulative production versus time, a solution which was shown to match the production history of more than 8,000 horizontal gas wells in the Barnett Shale. The success of the diffusion model in reproducing the universal scaling curve broadens the set of geometrical setups from which the universal scaling may emerge: the diffusion model relaxes Patzek et al.'s assumption of parallel planar hydrofracture stages, the setup for which the scaling was originally derived, and shows that the same scaling emerges from a complex fracture network.

The objective in this section is to verify whether or not τ and M for any given fracture network scale the numerically obtained cumulative production versus time data for the network onto the universal solution. To answer this question, the diffusion model was run on 5 fracture networks of different size and geometry and for each network the cumulative production versus time,

the characteristic time τ and the original gas in place M were computed. The fracture networks were generated using the percolation model of Chapter 2, were all at or above the threshold and were not processed by the hydrofracture model of Chapter 3. For each network, cumulative production and time were then scaled with the corresponding M and τ , respectively, to give the recovery factor RF and scaled time \tilde{t} . All scaled curves were then plotted on one graph, given by Figure 4.8.

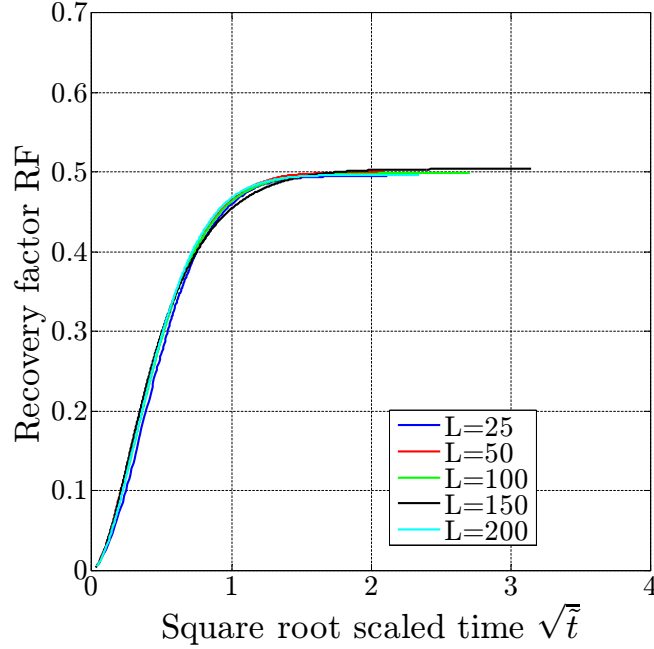


Figure 4.8: The diffusion model exactly reproduces the universal scaling curve due to Patzek et al. (2013). For 5 fracture networks of different size and geometry, we have computed the cumulative production versus time, τ and M using the diffusion model, then scaled cumulative production with M to get the recovery factor RF and scaled time with τ to obtain scaled time \tilde{t} . This plot confirms that the computed τ and M are indeed characteristic scales, as the scaled production plots all fall on a single curve, referred to as the universal scaling curve.

The lattice sizes considered here are $L = 25, 50, 100, 150,$ and 200 . As Figure 4.8 shows, the plots for different lattice sizes fall quite closely on top of each other and trace a single universal scaling curve. Moreover, after a relatively short period of initial transients (the early time power law of Figure 4.6), the scaling curve becomes linear in $\sqrt{\tilde{t}}$ and remains so until $\sqrt{\tilde{t}} \approx 0.6$, at which point the curve starts to roll over and then becomes flat after

$\tilde{t} = 1$. This trend, which was obtained from scaling the data computed by the diffusion model, exactly describes the orange curve in Figure 4.3, which was obtained from scaling real production data.

The question which arises now is what τ for a fracture network physically corresponds to. Recall that Patzek et al.'s model treats hydraulically fractured shale as a homogenous, fracture-free region of uniform permeability, bounded between two parallel planar absorbing hydrofractures. In this setup, τ is the characteristic time to interference and gives the travel time of the diffusive pressure wave to get from one hydrofracture plane to the plane half-way to the nearest hydrofracture stage. The model presented in this chapter, however, considers the fracture network responsible for production explicitly and yet scaling the numerical cumulative production versus time data for any fracture network with τ (and M) yields the universal scaling curve first obtained by Patzek et al.

As shown by equation (4.10),

$$\tau = \frac{d^2}{\alpha_i},$$

τ is in a one-to-one correspondence with a characteristic distance d , so defining d will uniquely define τ . Patzek et al. (2013) has shown that if the permeability of the shale matrix is taken to be 10 nD, then the characteristic distance has to be 1.5 – 3 m.

We use the diffusion model here to identify the characteristic distance of fracture networks; τ is then the time it takes for the pressure wave to

travel the characteristic distance. The definition uses only the geometry of the fracture network and the drainage area. For a given fracture network draining a given region, we find that the characteristic distance d is the average distance between a randomly chosen point inside the region to the nearest fracture of the network. Because our diffusion model is set up on a lattice, the gas can only travel up/down and left/right and therefore the characteristic distance is a “city block” distance and not a Euclidean distance. We employ this definition of d in a Monte Carlo scheme and use it to compute d for 5 fracture networks of different size and geometry. The results are presented in Figure 4.9.

Figure 4.9 confirms that our definition for d indeed captures the characteristic distance of fracture networks. Similar to Figure 4.8, Figure 4.9 shows scaled cumulative production versus time plots obtained from the diffusion model for 5 fracture networks of different size and geometry. Unlike Figure 4.8 where the plots are scaled with τ and M , the plots here are scaled with the characteristic distance d and M . (In this procedure, scaled time $\tilde{t} = \frac{\text{arrival time}}{d}$, since d in the diffusion model is measured in steps.) As Figure 4.9 shows, the curves for $L = 50, 100$ and 200 fall on top of each other and the curves for $L = 25$ and 150 are close to the rest of the curves, confirming that our definition of characteristic distance is correct.

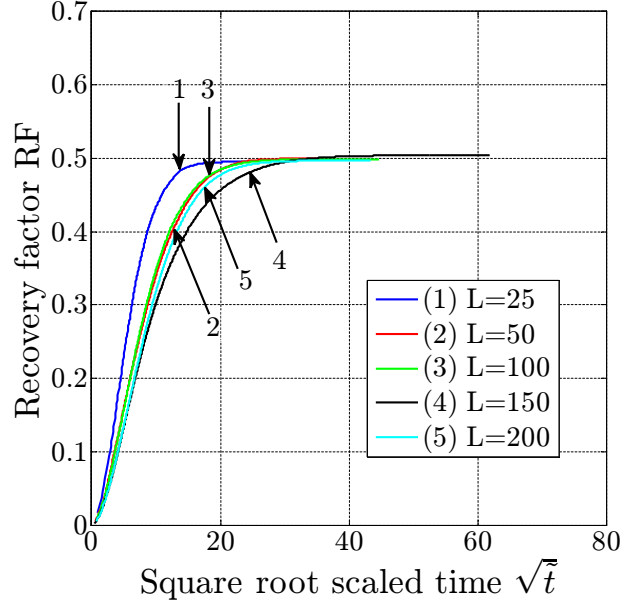


Figure 4.9: The scaled cumulative production versus square root of time plots for 5 fracture networks of different size and geometry. The maximum standard error in RF for all sizes does not exceed 0.14% (not shown on the plot). For each network, we have computed the cumulative production versus time and M using the diffusion model of section §4.3. The characteristic distance d was computed next; d and M were then used to scale the cumulative production versus time data. Recovery factor RF is $\frac{\text{cumulative production}}{M}$, and scaled time \tilde{t} is $\frac{\text{arrival time}}{d}$. The scaled plots fall on top of one another, which means that our definition of d indeed captures the characteristic distance of the fracture networks.

The scaled plot for each realization of the diffusion model falls close to the plots of other realizations and the standard error is very small: for all system sizes considered in Figure 4.9, the standard error does not exceed 0.14%. The scaled plot for each realization of the diffusion model for $L = 25$

is presented in Figure 4.10.

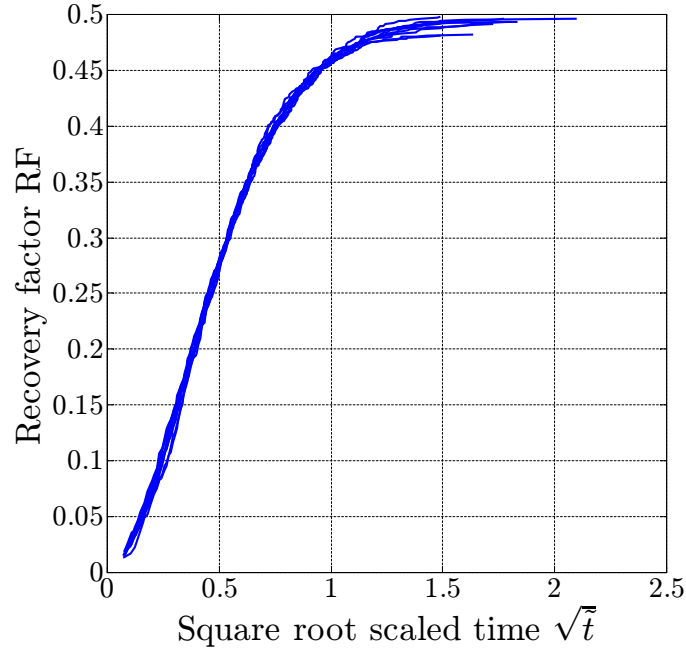


Figure 4.10: 10 different realizations of the diffusion model for $L = 25$. The scaled plots are very close. This is also the case for all the other system sizes considered in Figure 4.9. The maximum standard error in RF (including all system sizes) does not exceed 0.14%.

4.5 Conclusions

We presented in this chapter a diffusion model which makes it possible to compute cumulative production versus time for production from hydraulically fractured shale. Previous chapters had established that the hydrofracture process ultimately creates a connected network of hydraulic fractures and natural/induced fractures, which we referred to as the fracture network. Previous

chapters allowed us to predict the time evolution of the geometry of the fracture network during injection. This chapter considers production due to the fracture network.

It was established in earlier chapters that during gas production from hydraulically fractured shale, natural gas travels from the organic matter inside the shale through the shale matrix to get to the fracture network, and then flows through the network fractures to the wellbore. The diffusion model presented in this chapter treats the fracture network predicted by previous chapters as the absorbing boundary to the transport equation which describes gas production from shales, and uses the random walk algorithm to solve the transport equation.

This chapter answers the questions which originally motivated the dissertation. These questions are about first the scaling of gas production from hydraulically fractured horizontal shale wells, and second the exact nature of the characteristic distance of fracture networks, which was discovered from the analysis due to Patzek et al. (2013).

Patzek et al.'s model solves the same transport equation, with the difference that their model treats hydrofractured shale as a homogenous medium of uniform permeability and takes this medium to be bounded between two parallel planar hydrofractures. The diffusion model presented in this chapter considers fractures explicitly. Patzek et al. showed, for more than 8,000 horizontal gas wells in the Barnett Shale, that scaling the cumulative production versus time data with respect to two characteristic scales, the time to inter-

ference τ and the original gas in place M , maps the cumulative production versus time plots for different wells onto a single scaling curve, which they referred to as the *universal scaling curve*. We showed in this chapter that scaling the output of the diffusion model with respect to M and τ reproduces Patzek et al.'s universal scaling curve, confirming that the setup of the two models is the correct mental picture for gas production from hydraulically fractured horizontal shale wells.

We concluded the chapter by using the diffusion model to identify, or define, the characteristic distance for fracture networks. The characteristic distance for a given fracture network was shown to be the average distance to the nearest fracture of the network, measured from a random point in the area drained by the network.

Chapter 5

Conclusions and Future Work

This chapter concludes the present dissertation. The original research of this dissertation was presented in Chapters 2 – 4. Our objective in this chapter is to review the contributions of this dissertation and propose new courses of research for future work.

We start by reviewing the questions which motivated this dissertation in the first place. We then move on to the models we developed to answer these questions. A total of three different models were developed in this dissertation and each was discussed in one of Chapters 2 – 4. While each model is designed to address a certain question, the three models fit together and form a coherent lattice model of gas production from hydraulically fractured shale reservoirs. We present in this chapter a map of how the models interact, and review specifically what questions each model answers. We then highlight the main findings of this dissertation.

We conclude this final chapter by identifying potential future courses of research which can build on the present work. Some of our suggestions for future work concern the underlying assumptions of our models and are aimed primarily at making the models more realistic. Others have to do with how

the work presented in this dissertation may be used to either predict certain production-related physical quantities of interest, or identify characteristics of gas production from hydrofractured shales.

5.1 Motivation

The present dissertation was motivated by two works due to Patzek et al., published in 2013 and 2014. These papers put forward a model for gas production from hydraulically fractured, horizontal wells in shales. The model assumes the hydrofracture stages to be parallel planes perpendicular to the horizontal well, takes natural gas to flow in a linear and transient fashion towards the hydrofractures, which act as absorbing boundaries, and treats hydrofractured shale as a homogenous medium of uniform permeability. Gas transport in this setup is given by the gas diffusivity equation, which describes the diffusion of gas pressure.

The model introduces two characteristic dimensions: a time scale τ , referred to as the time to interference, and a mass scale M , known as the original gas in place. The time to interference represents the time it takes the pressure wave from one hydrofracture to reach the plane mid-way to the nearest hydrofracture, at which point pressure in the mid-plane falls below the original reservoir pressure and pressure decline slows down. The original gas in place M is the amount of gas available in the reservoir volume drained by the well.

This dissertation was conceived as the immediate follow up to the

Patzek et al. papers. Two particular results of the Patzek et al. papers point to a gap in our understanding of the hydrofracture process. The first result is that scaling the cumulative production history of real wells with respect to τ and M maps the decline plots onto a single curve, referred to as the *universal scaling curve*, and that the universal scaling curve fits the production history of more than 8,000 wells in the Barnett Shale with reasonable accuracy. The emergence of the universal scaling curve proves that M and τ are indeed characteristic scales of gas production from hydrofractured horizontal shale wells.

The second result is that if one assumes the permeability of hydrofractured shale to be equal to the lab measured value of 10 nD, then to account for the observed field production data with the model the spacing between the hydrofracture stages has to be 1.5 – 3 m. This conclusion of course does not suggest that the hydrofracture stages in the field are spaced 1.5 – 3 m apart, but that the hydrofracture process creates a network of hydraulically induced and natural fractures which has a *characteristic spacing* of 1.5 – 3 m. We have adopted this mental picture in this dissertation. (There is, however another equally valid take on this result, which we mention here only for the sake of completeness and do not pursue further: if one takes the spacing between hydrofracture stages in the model to be equal to a typical value used in the field, then to account for the observed field production data with the model requires shale permeability values which are 10 – 100 times larger than the lab measured values of permeability for unfractured shale.)

Patzek et al.'s model treats the effect of the fracture network on gas production as a small spacing between hydrofracture stages which bound a homogenous reservoir of uniform permeability equal to the lab measured value; the model does not include the hydraulically induced fracture network explicitly. Details of how fracture networks evolve geometrically and temporally are therefore beyond the reach of the model. In particular, to identify the exact nature of characteristic spacing for fracture networks requires a model of gas production from fracture networks.

The objective of this dissertation was to study the production and formation properties of the hydraulically induced fracture networks which make gas production from shales possible. Connectivity of fracture networks, the mechanics of network growth, and production from hydraulically fractured shales are the topics explored in this dissertation, each discussed in detail in one of Chapters 2 – 4.

5.2 The Models

We now present a review of the models developed in this dissertation and start with an overview of what each model does and how the models fit together. We then review the main results from each model in more detail.

The framework in which we study the connectivity of fracture networks is percolation theory. The percolation model is the subject of Chapter 2, and describes the topology of the natural fracture/incipient crack system of shales.

We suggest that production from hydraulically fractured shales comes from that subset of the natural fracture/incipient crack system which gets opened by the fracturing fluid during the injection, and develop in Chapter 3 a geomechanical model of hydraulic fracture which allows us to predict which natural fracture/incipient crack will open during injection, and when. The model of Chapter 3 can simulate initiation and propagation of hydraulic fractures and can account for the interaction between hydraulic and natural fractures/incipient cracks. Ultimately, our hydrofracture model makes it possible to describe the time evolution of the fracture network geometry during injection.

The output of the percolation model and the hydrofracture model combined is the geometry of the fracture network responsible for production. Next, we presented in Chapter 4 a diffusion model to compute production from the predicted fracture network. The diffusion model makes it possible to investigate how the geometry of the fracture network affects production.

All models of this dissertation are constructed on a two-dimensional square lattice and include fractures which are represented by lattice bonds. The models are all pseudo-three-dimensional.

5.2.1 Chapter 2: The Percolation Model

We focused in Chapter 2 on the topology and connectivity of the natural fracture/incipient crack system. The percolation model of Chapter 2 treats the natural fracture/incipient crack system of shales as a random population of

lines on the bonds of a two-dimensional square lattice. Based on geological observations, fracture length was assumed to follow a power law distribution characterized by an exponent e .

We showed that based on the value of the exponent e , fracture network connectivity emerges from either the clustering of fractures shorter than lattice size ($e > 2$), or the presence of a few fractures or even a single fracture of a size comparable to or longer than the lattice size, which can directly connect the opposite sides of the lattice ($1 < e < 2$). We note that despite differences in definition and setup, this result for lattice systems and horizontal/vertical fractures is identical to the result due to Bour and Davy (1997) for continuum systems and random fracture orientations.

In the limiting case where connectivity is achieved by a single fracture longer than the system size, we analytically derived the closed form expression for the probability of connectivity.

Finally, we numerically computed the percolation threshold as a function of e and showed that it agrees with the theoretical scaling predicted in this work: for $1 < e < 2$, the threshold is close to 0; for $e > 2$, the threshold rapidly increases and asymptotically converges to 50% as $e \rightarrow \infty$.

5.2.2 Chapter 3: The Hydrofracture Model

We focused in Chapter 3 on the mechanics of how the fracture network is created. We presented a numerical framework to simulate initiation and propagation of hydraulic fractures, as well as the interaction of hydraulic frac-

tures with natural fractures/induced cracks. The model makes it possible to explore the geometric and temporal complexities associated with the growth of hydraulically induced fracture networks.

We chose to include an “intermediate” level of details in the model: fluid flow through hydraulic fractures was modeled with the Reynolds lubrication approximation, and the stress response was modeled using analytical estimates. This choice was made to ensure that the model could include the interaction of hydraulic fractures with a large number of natural fractures/induced cracks, while maintaining computational efficiency.

The model was validated against the Perkins-Kern-Nordgren theory. The numerics are in reasonable agreement with theory and as originally intended, the model is computationally efficient.

Our results in this chapter come in the form of qualitative observations. The first observation is that hydraulic fractures tend to propagate straight and branching was observed to happen primarily after hydraulic fractures had reached the end of their natural fracture/induced crack path. Second, hydraulic fractures appear to propagate one at a time for the most part, and third, hydraulic fractures get slower as they grew longer. Fourth, less heterogeneity in the mechanical properties of the cement tend to lead to branches which form close to the base of dynamic cracks, while more heterogeneity allows branches to form farther from the base and even close to the tip of a dynamic crack.

5.2.3 Chapter 4: The Diffusion Model

We focused in Chapter 4 on how the geometry of the fracture network affects production. We presented in Chapter 4 a diffusion model which makes it possible to compute cumulative production versus time for production from hydraulically fractured shale. The model uses the random walk algorithm to solve the transport equation which describes gas production from shales. The fracture network predicted by Chapter 2 and Chapter 3 is used in the diffusion model as the absorbing boundary to the transport equation.

Our first contribution in this chapter was to show that the universal solution of Patzek et al. for production history emerges as a result of gas pressure diffusion to an absorbing, complex network of fractures. This result broadens the geometrical setup which leads to the universal solution, as fracture network geometry is less restrictive than parallel planar hydrofractures.

We ran the diffusion model for several fracture networks of different size and geometry and showed that scaling the numerically obtained cumulative production versus time data with respect to the characteristic scales of production maps the scaled plots for all network sizes onto a single curve which is Patzek et al.'s universal scaling curve. The success of our diffusion model in reproducing Patzek et al.'s universal solution confirms that the setup of the two models is the correct mental picture for gas production from hydraulically fractured horizontal shale wells.

Finally, we used the diffusion model to identify, or define, the character-

istic spacing of fracture networks. We showed that the characteristic distance for a given fracture network is the average distance to the nearest fracture of the network, measured from a random point in the area drained by the network.

5.3 Future Work

Having discussed the work done in this dissertation, we present in this section several possible extensions or new applications of the present work. Each suggestion is discussed in one of the following subsections.

5.3.1 Early-Time Production

Re-visiting Figure 4.6 (re-plotted here in Figure 5.1), we now focus on the early time power law fit to simulation data. We suspect that the power law here may be a signature of the fracture network geometry and suggest that future research investigate this suspicion. We note that the early time production behavior is systematically not captured by the analytical solution of equation (4.18) (the dashed blue curve in Figure 5.1); also, emergence of the power law implies scale-independence and makes a fractal analysis seem relevant here.

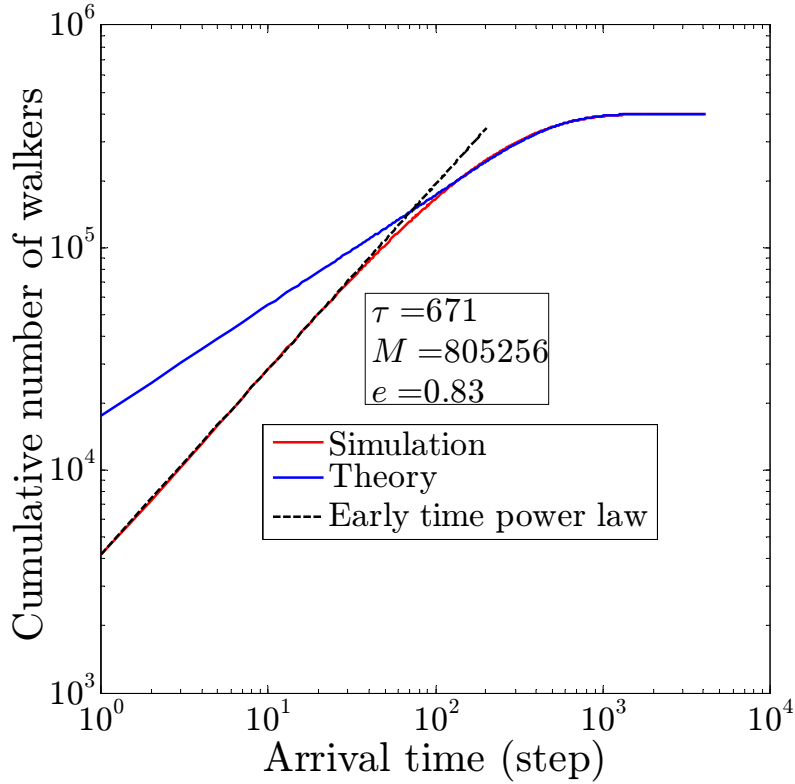


Figure 5.1: Figure 4.6, revisited. The procedure to compute the characteristic time to interference and the original gas in place is based on computing the least squares fit of equation (4.18) to the cumulative distribution of arrival time. The arrival time data in the plot is obtained from running the random walk algorithm on the example system of Figure 4.5. To obtain a smooth enough distribution, we have swept through all the walkers 10 times and pooled the recorded arrival time data. The fitting parameters τ and M are the original gas in place and the characteristic time to interference, respectively; τ scales the arrival time data onto physical time and M scales the cumulative number of walkers onto cumulative production. The dashed black line represents a power law fit to early time simulation data. The exponent of the power law fit is given by e .

5.3.2 Characteristic Distance as a Function of Fracture Network Geometry

Going back to Figure 4.9 (re-plotted here in Figure 5.2), we note that the scaled plots all fall quite closely on the universal scaling curve, except for $L = 25$ and $L = 150$. The question which now arises is what distinguishes these two fracture networks from the rest. More specifically, we suggest that future research attempts to establish how the characteristic distance changes as a function of the percolation probability p and injection time. We note that the hydrofracture code of Chapter 3 may be used to obtain the time evolution of characteristic distance.

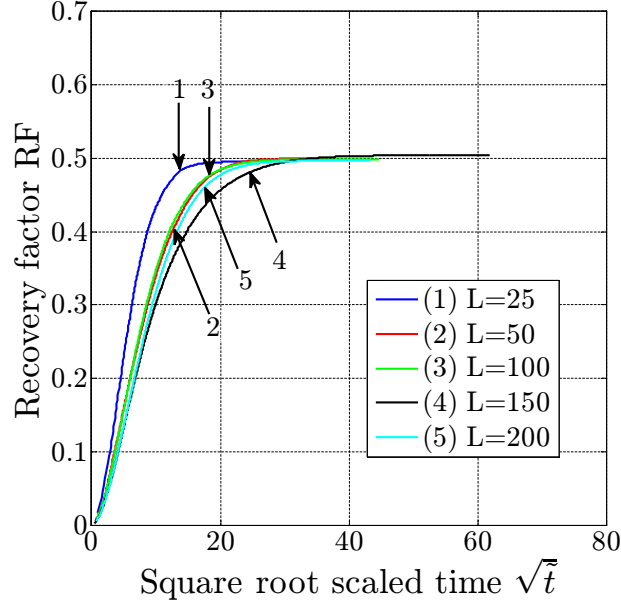


Figure 5.2: Figure 4.9, revisited. The scaled cumulative production versus square root of time plots for 5 fracture networks of different size and geometry. The maximum standard error in RF for all sizes does not exceed 0.14% (not shown on the plot). For each network, we have computed the cumulative production versus time and M using the diffusion model of section §4.3. The characteristic distance d was computed next; d and M were then used to scale the cumulative production versus time data. Recovery factor RF is $\frac{\text{cumulative production}}{M}$, and scaled time \tilde{t} is $\frac{\text{arrival time}}{d}$. The scaled plots fall on top of one another, which means that our definition of d indeed captures the characteristic distance of the fracture networks.

5.3.3 Scaling of Original Gas in Place with Reservoir Size

Scaling of the original gas in place with the size of the reservoir is an interesting topic which may be explored using the diffusion model. In the diffusion model, original gas in place is given by M , obtained from fitting

equation (4.18) to numerically obtained cumulative production versus time data, and reservoir size is lattice size L . We note that the current setup of the diffusion model drains all of the walkers inside the system and therefore always leads to $M \sim L^2$, Figure 5.3. Field data indicate, however, that the scaling exponent is not 2 but close to 0.8.

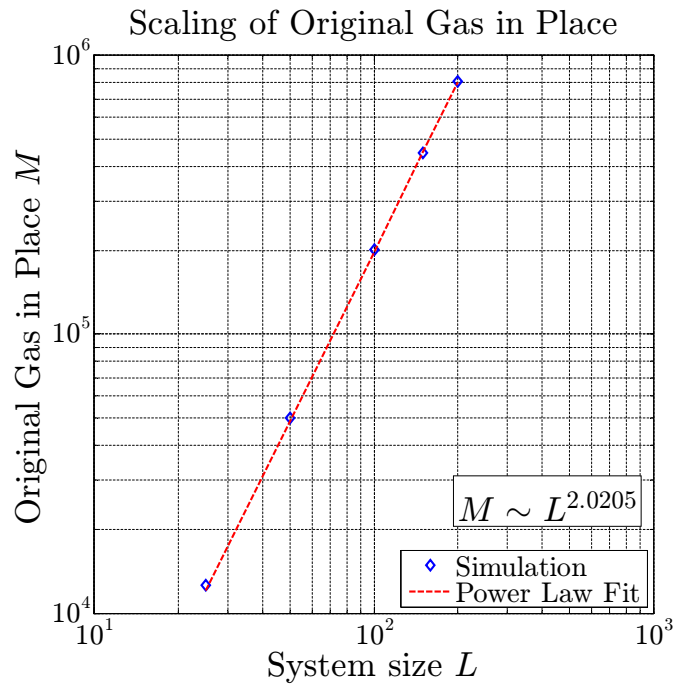


Figure 5.3: The diffusion model was run for 5 fracture networks of different size and geometry. The sizes considered for this plot are $L = 25, 50, 100, 150$ and 200 . For each network, the numerically obtained cumulative production versus time data was then fit with equation (4.18) and the original gas in place M was determined. The original gas in place scales with L^2 , reflecting the current setup of the diffusion model in which all walkers inside the lattice will be eventually produced.

A possible future course of research is to run the diffusion model on a

drainage area which represents how far away from the fracture network the diffusive pressure wave will travel during the life of the well. An estimate of the size of the drainage area may be obtained based on an average hydraulic diffusivity, perhaps the value which corresponds to average reservoir pressure during production, and a typical well life between 15 – 25 years. Here,

$$\alpha = \frac{(\text{travel distance of pressure wave})^2}{\text{well life}}.$$

5.3.4 The Stress Shadow Effect

As discussed earlier in Chapter 3, the stress shadow effect does not emerge naturally from the underlying assumptions of our hydrofracture model and therefore has to be manually added. Given that the model already relies on analytical estimates to predict the stress response, it seems plausible that an analytical estimate of the stress shadow effect, perhaps the one obtained by Geilikman and Wong (2013), can be added to the model.

5.3.5 Thermodynamic Properties of Natural Gas

In the diffusion model of Chapter 4, we assumed the natural gas to be ideal, for which the hydraulic diffusivity α is a constant and the transport equation becomes linear. Because the gas was ideal and the interaction between gas particles was negligible, a random walk of fixed step size and fixed time step could solve the transport equation. In the diffusion model, we took $\alpha = 1$, and took the step size to be equal to the lattice spacing.

Natural gas is not an ideal gas, and the hydraulic diffusivity α varies

strongly with temperature and pressure. A future course of research here is to treat the thermodynamic properties of natural gas properly, and extend the basic random walk algorithm in a way that can model variable α . The random walk algorithm should keep track of pressure at every point inside the lattice and have the random walkers take steps of variable size (or time step) according to the local value of pressure.

5.3.6 Finite Fracture Conductivity

In the diffusion model, fractures of the hydrofracture network were taken to be infinitely conductive. This assumption is justified by considering that shales are almost impermeable, and fractures are highly conductive. It follows from this assumption that as soon as a walker hits a fracture, it is immediately produced and the aperture of the fracture does not enter the picture in any way. Real fractures, however, have different finite conductivities because they have different apertures and surface properties and may or may not be propped. A possible course of future research here is to extend the diffusion model to account for networks of finite-conductivity fractures.

The extension can be done as follows: fractures should no longer be treated as line sinks but as regions of space, with areas specified by the aperture and length. Fractures that are less conductive should have a smaller diffusion coefficient (hydraulic diffusivity in the diffusion model). For a two-dimensional block of shale, this scheme partitions the lattice into regions with different diffusion coefficient values. As far as coding of the walk algorithm, there are

two ways to implement a spatially variable diffusion coefficient. Since in two dimensions

$$D = \frac{l^2}{4\tau},$$

one could either specify the random walker to take longer/shorter steps or change the time-step.

5.3.7 Extension to Three Dimensions

As mentioned earlier in this chapter, all models of this dissertation are constructed on a two-dimensional square lattice and include fractures which are represented by lines (the models are all pseudo-three-dimensional). A possible course of future research here is to extend the models to three dimensions, where (among numerous other new details) fractures will be represented by planes which are not necessarily vertical.

Bibliography

- [1] Adachi, J., Siebrits, E., and Peirce, A. 2007. Computer simulation of hydraulic fractures. *Int. J. Rock. Mech. Min.*, **44**(5): 739–757. <http://dx.doi.org/10.1016/j.ijrmms.2006.11.006>
- [2] Al-Ahmadi, H.A., Almarzooq, A.M., and Wattenbarger, R.A. 2010. Application of linear flow analysis to shale gas wells—Field cases. SPE Unconventional Gas Conference, Pittsburgh, Pennsylvania, USA, 23-25 February. SPE-130370-MS. <http://dx.doi.org/10.2118/130370-MS>
- [3] Al-Hussainy, R., Ramey Jr., H.J., and Crawford, P.B. 1966. The flow of real gases through porous media. *J. Pet. Technol.* **18**(5): 624–636. SPE-1243-A-PA. <http://dx.doi.org/10.2118/1243-A-PA>
- [4] Al-Futaisi, A., and Patzek, T.W. 2003. Extension of Hoshen–Kopelman algorithm to non–lattice environments. *Physica A* **321**(3) 665–678
- [5] Berkowitz, B., and Balberg, I. 1993. Percolation theory and its applications to groundwater hydrology. *Water Resour. Res.*, **29**(4): 775–794. <http://dx.doi.org/10.1029/92wr02707>
- [6] Blanton, T.L. 1982. An experimental study of interaction between hydraulically induced and pre-existing fractures. Presented at the SPE/DOE

Unconventional Gas Recovery Symposium, Pittsburgh, Pennsylvania, USA, 16–18 May. SPE/DOE 10847. <http://dx.doi.org/10.2118/10847-MS>

- [7] Bonnet, E., Bour, O., Odling, N. E. et al. 2001. Scaling of fracture systems in geological media. *Rev. Geophys.*, **39**(3): 347–383. <http://dx.doi.org/10.1029/1999RG000074>
- [8] Bour, O., and Davy, P. 1997. Connectivity of random fault networks following a power law fault length distribution. *Water Resour. Res.*, **33**(7): 1567–1583. <http://dx.doi.org/10.1029/96WR00433>
- [9] Broadbent, S.R., and Hammersley, J.M. 1957. Percolation processes. I. Crystals and mazes. *Math. Proc. Cambridge*, **53**(3): 629–641.
- [10] Chen, C.H. 2014. *Scaling and instability of dynamic fracture*. Dissertation, The University of Texas at Austin, Austin, Texas (May 2014). Retrieved from <https://repositories.lib.utexas.edu/bitstream/handle/2152/24927/CHEN-DISSERTATION-2014.pdf?sequence=1>
- [11] Clark, J.B. 1949. A hydraulic process for increasing the productivity of wells. *J. Pet. Technol.*, **1**(1): 1–8. SPE-949001-G. <http://dx.doi.org/10.2118/949001-G>
- [12] Clifton, R., Abou-Sayed, A. and Brechtel, C. 1978. In situ stress determination by hydrofracturing: A fracture mechanics approach. *J. Geophys. Res.* **83**(6): 2851–2862. <http://dx.doi.org/10.1029/JB083iB06p02851>

- [13] Cotterell, B., and Rice, J.R. 1980. Slightly curved or kinked cracks. *Int. Journ. of Fracture*, **16**(2): 155–169.
- [14] Crouch, S.L. and Starfield, A.M. 1983. *Boundary Element Methods in Solid Mechanics*. London: George Allen & Unwin.
- [15] Dahi–Taleghani, A., and Olson, J. 2011. Numerical modeling of multi-stranded hydraulic fracture propagation: accounting for the interaction between induced and natural fractures. *SPE J.* **16** (03): 575–581. SPE 124884. <http://dx.doi.org/10.2118/124884-PA>
- [16] DOE NETL. 2009. Modern Shale Gas Development in the United States: A Primer. April 2009. http://energy.gov/sites/prod/files/2013/03/f0/ShaleGasPrimer_Online_4-2009.pdf (retrieved November 2016).
- [17] DOE NETL. 2013. Modern Shale Gas Development in the United States: An Update. September 2013. <https://www.netl.doe.gov/File%20Library/Research/Oil-Gas/shale-gas-primer-update-2013.pdf> (retrieved November 2016).
- [18] DOE NETL. 2011. Shale Gas: Applying Technology to Solve America’s Energy Challenges. March 2011. http://www.netl.doe.gov/file%20library/research/oil-gas/Shale_Gas_March_2011.pdf (retrieved November 2016).
- [19] EIA. 1993. Drilling Sideways – A Review of Horizontal Well Technology and Its Domestic Application. April 1993. <http://www.eia.gov/pub/>

oil_gas/natural_gas/analysis_publications/drilling_sideways_well_ technology/pdf/tr0565.pdf (retrieved November 2016).

- [20] EIA. 2013. Technically Recoverable Shale Oil and Shale Gas Resources: An Assessment of 137 Shale Formations in 41 Countries Outside the United States. June 2013, <http://www.eia.gov/analysis/studies/worldshalegas/pdf/overview.pdf> (retrieved November 2016).
- [21] EIA. 2015. Lower 48 states shale plays. 13 April 2015, https://www.eia.gov/oil_gas/rpd/shale_gas.pdf (retrieved November 2016).
- [22] EIA. 2015. The Growth of U.S. Natural Gas: An Uncertain Outlook for U.S. and World Supply. June 2015, <http://www.eia.gov/conference/2015/pdf/presentations/staub.pdf> (retrieved November 2016).
- [23] EIA. 2016. U.S. Dry Natural Gas Production by Source. June 2016, <http://www.eia.gov/todayinenergy/detail.php?id=26552> (retrieved November 2016).
- [24] EIA. 2016. Annual Energy Outlook. September 2016, [http://www.eia.gov/forecasts/aeo/pdf/0383\(2016\).pdf](http://www.eia.gov/forecasts/aeo/pdf/0383(2016).pdf) (retrieved November 2016).
- [25] Erdogan, F., and Sih, G.C. 1963. On the crack extension in plates under loading and transverse shear. *J. Fluids Eng.* **85** (4): 519–527. <http://dx.doi.org/10.1115/1.3656897>
- [26] Fisher, M.K., Heinze, C.D., Davidson, B.M. et al. 2004. Optimizing horizontal completion techniques in the Barnett Shale using micro-

- seismic fracture mapping. Presented at the SPE Technical Conference and Exhibition, Houston, Texas, USA, 26–29 September. SPE 90051. <http://dx.doi.org/10.2118/90051-MS>
- [27] Fisher, M.K., and Warpinski, N.R. 2011. Hydraulic fracture height growth: real data. *SPE Prod. Oper.* **27**(2): 8–19. SPE-145949-PA. <http://dx.doi.org/10.2118/145949-PA>
- [28] Gale, J.F.W. 2008. Natural fractures in shales: origins, characteristics and relevance for hydraulic fracture treatments. Presented at the AAPG Annual Convention, San Antonio, Texas, USA, 20–23 April. Search and Discovery Article #40338.
- [29] Gale, J.F.W., and Holder, J. 2008. Natural fractures in the Barnett Shale: constraints on spatial organization and tensile strength with implications for hydraulic fracture treatment in shale–gas reservoirs. Presented at the 42nd US Rock Mechanics Symposium and 2nd US–Canada Rock Mechanics Symposium, San Francisco, California, USA, June 29–July 2. ARMA 08-096.
- [30] Gale, J.F.W., and Holder, J. 2010. Natural fractures in some US shales and their importance for gas production. *Petroleum Geology Conference series*, **7**: 1131–1140. <http://dx.doi.org/10.1144/0071131>
- [31] Gale, J.F.W., Laubach, S.E. Olson, J.E. et al. 2014. Natural fractures in shale: A review and new observations. *AAPG Bull.*, **98**(11): 2165–2216. <http://dx.doi.org/10.1306/08121413151>

- [32] Geertsma, J. and de Klerk, F.A. 1969. A rapid method of predicting width and extent of hydraulically induced fractures. *J. Pet. Technol.* **21**(12): 1571–1781. SPE-2458-PA. <http://dx.doi.org/10.2118/2458-PA>
- [33] Geilikman, M. and Wong, S. -W. 2013. Hydraulic fractures interference in horizontal wells: compact and diffuse patterns of fracture growth. Presented at SPE Unconventional Resources Conference, Calgary, Alberta, Canada, 5-7 November. SPE-167161-MS. <http://dx.doi.org/10.2118/167161-MS>
- [34] Griffith, A.A. 1921. The phenomena of rupture and flow in solids. *Philos. T. R. Soc. Lond.* **221**(582–593): 163–198 <http://dx.doi.org/10.1098/rsta.1921.0006>
- [35] Haddad, M., and Sepehrnoori, K. 2014. Simulation of hydraulic fracturing in quasi–brittle shale formations using characterized cohesive layer: Stimulation controlling factors. *J. Unconventional Oil Gas Resourc.* **9**:65–83. <http://dx.doi.org/10.1016/j.juogr.2014.10.001>
- [36] Haddad, M., and Sepehrnoori, K. 2016. XFEM–Based CZM for the simulation of 3D multiple–cluster hydraulic fracturing in quasi–brittle shale formations. *J. Rock Mech. Rock Eng.* <http://dx.doi.org/10.1007/s00603-016-1057-2>
- [37] Hooker, J.N., Laubach, S.E., and Marrett, R. 2014. A universal power law scaling exponent for fracture apertures in sandstones. *Geol. Soc. Am. Bull.* **126**(9): 1340–1362 <http://dx.doi.org/10.1130/B30964.1>

- [38] Hoshen, J., and Kopelman, R. 1976. Percolation and cluster distribution. I. Cluster multiple labeling technique and critical concentration algorithm. *Phys. Rev. B.* **14**(8): 3438-3445 <https://doi.org/10.1103/PhysRevB.14.3438>
- [39] Hubbert, M.K., and Willis, D.G. Mechanics of hydraulic fracturing. *Transactions AIME* **210**: 153–168. SPE-686-G. Retrieved from <https://www.onepetro.org/general/SPE-686-G>
- [40] Irwin, G.R. 1957. Analysis of stresses and strains near the end of a crack traversing a plate. *J. Appl. Mech.* **24**: 361–364.
- [41] Khristianovic, S. A. and Zheltov, Y.P. 1955. Formation of vertical fractures by means of highly viscous fluid. Presented at 4th World Petroleum Congress, Rome, Italy, 6–15 June. WPC-6132.
- [42] Marder, M., Chen, C.H., and Patzek, T.W. 2015. Simple models of the hydrofracture process. *Phys. Rev. E* **92**(6): 062408-1–062408-12. <http://dx.doi.org/10.1103/PhysRevE.92.062408>
- [43] Marrett, R. Ortega, O. J., and Kelsey, C.M. 1999. Extent of power law scaling for natural fractures in rock. *Geol. Soc. Am. Bull.* **27** (9): 799–802. [http://dx.doi.org/10.1130/0091-7613\(1999\)027%3C0031:SACOTA%3E2.3.CO;2](http://dx.doi.org/10.1130/0091-7613(1999)027%3C0031:SACOTA%3E2.3.CO;2)
- [44] Nobakht, M., Mattar, L., Moghadam, S. et al. 2012. Simplified forecasting of tight/shale-gas production in linear flow. *J. Can. Pet. Tech-*

- nol.* **51**(6): 476–486. SPE-133615-PA. <http://dx.doi.org/10.2118/133615-PA>
- [45] Nordgren, R.P. 1972. Propagation of a vertical hydraulic fracture. *SPE J.* **12**(4): 306–314. SPE 3009-PA. <http://dx.doi.org/10.2118/3009-PA>
- [46] Nuismer, R. 1975. An energy release rate criterion for mixed mode fracture, *Int. J. Fracture.* **11** (2): 245–250 <http://dx.doi.org/10.1007/BF00038891>
- [47] Olson, J.E. 1990. *Fracture Mechanics Analysis of Joints and Veins*. Dissertation, Stanford University, Stanford, California (December 1990).
- [48] Olson, J.E. 1997. Natural fracture pattern characterization using a mechanically-based model constrained by geologic data - moving closer to a predictive tool. *Int. J. Rock Mech. & Min. Sci.* **34**: 3–4, Paper No. 237. [http://dx.doi.org/10.1016/S1365-1609\(97\)00227-X](http://dx.doi.org/10.1016/S1365-1609(97)00227-X)
- [49] Olson, J.E. 2004. Predicting fracture swarms—The influence of subcritical crack growth and the crack-tip process zone on joint spacing in rock. *Geol. Soc. Spec. Publ.* **231**: 73–88. <http://dx.doi.org/10.1144/GSL.SP.2004.231.01.05>
- [50] Olson, J.E. 2007. Fracture Aperture, Length and pattern geometry development under biaxial loading: A numerical study with applications to natural, cross-jointed systems. *Geol. Soc. Spec. Publ.* **289**: 123–142. <http://dx.doi.org/10.1144/SP289.8>

- [51] Patzek, T.W., Male, F., and Marder, M. 2013. Gas production in the Barnett Shale obeys a simple scaling theory. *Proc. Natl. Acad. Sci.* **110**(49): 19731-19736. <http://dx.doi.org/10.1073/pnas.1313380110>
- [52] Patzek, T.W., Male, F., and Marder, M. 2014. A simple model of gas production from hydrofractured horizontal wells in shales. *AAPG Bull.* **98**(12): 2507-2529. <http://dx.doi.org/10.1306/03241412125>
- [53] Perkins, T.K. and Kern, L.R. 1961. Width of hydraulic fractures. *J. Pet. Technol.* **13**(9): 937-949. SPE-89-PA. <http://dx.doi.org/10.2118/89-PA>
- [54] Reynolds, O. 1886. On the theory of lubrication and its application to Mr. Beauchamp Tower's experiments, including an experimental determination of the viscosity of olive oil. *Philos. T. R. Soc. Lond.* **17**: 157-234. <http://dx.doi.org/10.1098/rspl.1886.0021>
- [55] Robinson, P.C. 1983. Connectivity of fracture systems—a percolation theory approach. *J. Phys. A: Math. Gen.* **16**(3): 605-614. <http://dx.doi.org/10.1088/0305-4470/16/3/020>
- [56] Ryder, R.T. 1996. Fracture patterns and their origin in the Upper Devonian Antrim Shale gas reservoir of the Michigan Basin: A review. Open-File report 96-23 US Geological Survey, Reston, Virginia, USA
- [57] Sahimi, M. 1994. *Applications of percolation theory*, first edition. London: Taylor and Francis.

- [58] Schlumberger. 2016. Plug And Perf. November 2016, http://www.slb.com/services/completions/multistage_stimulation_systems/plug_and_perf.aspx (retrieved November 2016).
- [59] Silin, D.B., and Kneafsey, T.J. 2012. Shale Gas: Nanometer-scale observations and well modeling. *J. Can. Pet. Technol.* **51**(6): 464–475. SPE-149489-PA. <http://dx.doi.org/10.2118/149489-PA>
- [60] Simonson, E.R., Abou-Sayed, A.S., and Clifton, R.J. 1978. Containment of massive hydraulic fractures. *SPE J.* **18**(1): 27–32. SPE-6089-PA. <http://dx.doi.org/10.2118/6089-PA>
- [61] Sneddon, I.N. 1946. The distribution of stress in the neighbourhood of a crack in an elastic field. *Proc. R. Soc. Lond. A* **187**: 229–260 <http://dx.doi.org/10.1098/rspa.1946.0077>
- [62] Stauffer, D., and Aharony, A. 1992. *Introduction to percolation theory*, revised second edition. London: Taylor and Francis.
- [63] Warpinski, N.R., and Teufel, L.W. 1987. Influence of geologic discontinuities on hydraulic fracture propagation. *J. Pet. Technol.* **39**(2): 209–220. <http://dx.doi.org/10.2118/13224-PA>
- [64] Westergaard, H.M. 1939. Bearing pressures and cracks. *J. Appl. Mech.* **6**: 49–53.
- [65] Wu, K., and Olson, J.E. 2013. Investigation of critical in-situ and injection factors in multi-frac treatments: Guidelines for controlling fracture

complexity. Presented at SPE Hydraulic Fracturing Technology Conference, The Woodlands, Texas, USA, 4-6 February. SPE-163821-MS. <http://dx.doi.org/10.2118/163821-MS>

[66] Wu, K., and Olson, J.E. 2015. Mechanisms of simultaneous hydraulic fracture propagation from multiple perforation clusters in horizontal wells. *SPE J.* **21**(3): 1000–1008. SPE-178925-PA. <http://dx.doi.org/10.2118/178925-PA>

[67] Wu, K. and Olson, J.E. 2015b. A Simplified Three-Dimensional Displacement Discontinuity Method for Multiple Fracture Simulations. *Int. J. Fracture* **193**: 191–204. <http://dx.doi.org/10.1007/s10704-015-0023-4>